ABSTRACT

Title of Document:	CARBON-SULFUR NANOCOMPOSITES FOR LITHIUM-SULFUR BATTERIES
	Jeremy Taylor Ticey, Doctor of Philosophy, 2015
Directed By:	Professor John Cumings, Department of Materials Science and Engineering

The increasing reliance on energy storage systems is constantly pushing research efforts to find better performing, low cost electrochemical batteries. The lithium-sulfur battery has been deemed one of the most viable candidates due to its high energy density and non-toxic, inexpensive components. In order to reach its full potential, sulfur should be incorporated into a conductive carbon host structure to ensure its electrical conductivity and cycling performance. In addition, rapid capacity fading resulting from the polysulfide shuttle mechanism should be addressed. The goal of this dissertation is to employ transmission electron microscopy (TEM) to study various nanostructured carbon materials that can serve as a cathode component in a lithium-sulfur battery.

The dissertation is divided into three topics. The first topic describes the creation of graphene/sulfur composites suitable for in-situ TEM. TEM studies on sulfur are limited due to sulfur's ability to sublimate at the operating conditions of

most conventional TEMs. Therefore, we develop a layered structure in which sulfur is enveloped between two graphene sheets to stabilize the sulfur. We report the fabrication methods and TEM analysis of these structures. The second topic is the study of sulfur which is incorporated into single-walled carbon nanotubes (SWCNTs). The inner cavity of a SWCNT provides a large electrochemical interface, good mechanical stability and the potential to retain polysulfides formed during cycling. We utilize a two-step procedure consisting of thermal oxidation and high-temperature filling to produce sulfur-filled SWCNTs. Our electrochemical testing shows a clear dependence on the cell's performance with the thermal oxidation temperature. We conclude that 475 °C is the optimal oxidation temperature for sulfur filling and results in the most stable cycling performance. The last topic is in-situ TEM studies of multi-walled carbon nanotube-sulfur composites utilizing various solid electrolytes. We examine the implications of employing a Li2S-P2S5 solid electrolyte and compare with a Li2O solid electrolyte during in-situ TEM studies. When using a Li2S-P2S5 solid electrolyte, we are able to show the formation of a lithium-sulfide phase on the surface of MWCNT-sulfur composites and show evidence of lithium dendrite growth suppression.

CARBON-SULFUR NANOCOMPOSITES FOR LITHIUM-SULFUR BATTERIES

By

Jeremy Taylor Ticey.

Dissertation submitted to the Faculty of the Graduate School of the
University of Maryland, College Park, in partial fulfillment
of the requirements for the degree of
Doctor of Philosophy
2015

Advisory Committee:
Professor John Cumings, Chair
Professor Liangbing Hu
Professor Gary Rubloff
Professor Chunsheng Wang
Professor Sang Bok Lee, Dean's Representative

Dedication

To my parents, for their love and support.

Acknowledgements

The completion of this dissertation would not have been possible without the help and support of many different people. First, I would like to thank my advisor Dr. John Cumings for his guidance and input throughout my time here at the University of Maryland. Since our first meeting, he has shown a great willingness to teach and discuss new ideas related to my research. Second, I would like to thank Dr. Vladimir Oleshko for contributing his expertise in both lithium-sulfur systems and analytical transmission electron microscopy. Your arrival to the group made a profound impact on the course of my studies and I am forever grateful for your help.

As a member of the Dr. Cumings' research group, I have had the opportunity to work and form friendships with a great collection of people. My group members Dr. Kamal Baloch, Dr. Merinjte Bronsgeest, Dr. Stephen Daunheimer, Dr. Kai He, Jasper Drisko, and Hanna Nilsson have all helped me immensely through discussion and leading by example through success in their own research. I would like to give a special thanks to Dr. Norvik Voskanian and Dr. Khim Kharki with whom I had the privilege of sharing an office for over four years. The long days and nights spent in the lab were much more enjoyable because they were shared with two of my closest friends.

I would like to thank my committee members Prof. Liangbing Hu, Prof. Gary Rubloff, Prof. Sang BokLee, and Prof. Chunsheng Wang for their input on the direction of my work. Also, thank you to my collaborator Dr. Yujie Zhu who provided his expertise in electrochemical testing to our experiments. I would also

like to thank the rest of the graduate students in our department, many of whom have become lifetime friends.

Last but not least, I would like to thank my family who has provided unwavering support throughout my doctoral studies. I could not have done it without your constant encouragement and positivity.

Table of Contents

List of Tables

List of Figures

Chapter 1: Introduction

With our daily lives becoming even more intertwined with electronic devices, the world's energy consumption is at an all-time high. Furthermore, with rapid population increases, it is expected that by the year 2050, our current energy production of 14 TW must be doubled to meet the world's increasing energy demands [1]. To reach these levels of energy production, it would require the equivalent of 10^{10} tons of oil per year resulting in even higher levels of CO_2 emissions [2] These trends highlight the need for alternative sources of energy which can provide the energy we need, in an environmentally friendly manner. While the development of renewable energy sources such as solar or wind power is vital to provide sustainable, clean, energy for future generations, their variability fails to provide a constant source of energy throughout the day. Therefore, a method to reliably store and access this generated energy is crucial to their utilization. Currently, Lithium-ion (Li-ion) technology is reaching a plateau of development, the goal of lightweight, portable electrochemical cells which can sustain itself over a long cycle-life and good performance has become a top industry priority. Of the potential candidates to replace Li-ion batteries, lithium sulfur (Li-S) batteries are widely considered to be the most viable candidate. This dissertation focuses around the design, fabrication, and characterization of novel cathode materials for use in Li-S batteries.

1.1 Energy Storage Systems

1.1.1 Battery Fundamentals

The basic operating principles of a secondary, or rechargeable, battery can be described as the conversion of electrical energy to chemical energy, and the reverse process, conversion of chemical energy to electrical energy. The battery can be broken into three main components: a negative electrode (anode), a positive electrode (cathode), and the electrolyte. Charging occurs through the transfer of an electron from the cathode to the anode via an external circuit. During this process, a positively charged cation flows through the electrolyte from the cathode to the anode. This previously described process is the conversion of electrical energy into chemical energy. During discharge, the opposite reaction occurs through the conversion of chemical energy to electrical energy. Discharge occurs when cations diffuse from the anode to the cathode with the simultaneous transfer of an electron from the cathode to the cathode. This process of cycling allows for the storage of electrochemical energy capable of powering electronic devices. [3]

To evaluate the performance of a battery, there are several common metrics used. The energy density can be expressed in two forms, gravimetric energy density and volumetric energy density. The gravimetric energy density, given in units W·h/kg, or mW·h/g, is a measure of the power, per unit weight, which the battery is able to supply. The capacity of the battery is the amount of charge per unit weight which can be extracted during cycling. This property is strongly dependent on electrochemistry of the cell in study. For example, low ionic conductivity in the electrolyte can result in a decrease in available lithium ions. This reaction, while

reversible, results in a temporary decrease in battery performance. Reactions such as the formation of a solid electrolyte interphase from cross-linked electrolyte, results in an irreversible loss of capacity as the amount of active material has been decreased. [4] Coulombic efficiency is an important measure of the ability of the battery's performance over multiple cycles. This value is the ratio of the discharge capacity and the charge capacity and typically demonstrates the stability of the battery. [4]

1.1.2 Li-ion battery limitations

The modern Li-ion battery consisting of a $LiCoO_2$ cathode and a graphite anode was first patented in 1985 [5]. Since being commercially introduced, has served as the most commonly used rechargeable electrochemical cell in portable electronic devices. Charging occurs when a potential, supplied by an external source, overcomes the battery's internal resistance to remove lithium ions from the $LiCoO_2$ cathode. They then diffuse through the electrolyte (and separator) and are intercalated into the graphitic anode structure. The reverse process occurs during charging. [4] A Li-ion battery using the previously described configuration possesses a theoretical capacity of 372 mA·h/g and an energy density of 387 W·h/kg. [6] One of the obstacles in replacing current Li-ion technology is creating a battery capable of matching the superior stability associated with Li-ion batteries. Li-ion batteries having demonstrated a cycle life up to 30,000 charge/discharge cycles [7], and as a result, any potential replacement must be able to match, or exceed, these capabilities. In addition to performance standards, careful consideration of cost, environmental

impact, and consumer safety, amongst others must be taken. With all considerations, one such candidate capable of addressing these concerns is the lithium-sulfur battery.

1.2 Lithium-sulfur batteries

The Li-S battery, first discovered in the 1960s [8], typically consists of a sulfur cathode and a lithium metal anode within an electrolyte. Sulfur itself is earthly abundant and costs roughly $150-200 per ton to produce [2]. The majority of sulfur is produced via the Claus Process:

$$2\ H_2S + O_2 \rightarrow 2\ S + H_2O \quad \text{(Eq. 1.1)}$$

Advantageously, this reaction utilizes the gas precursor hydrogen disulfide (H_2S) which is produced both naturally, as well as, during oil refinement [9]. In 2014, roughly 9.0 million tons of sulfur were produced in the United States [10] Given the ease of sulfur production, as well its environmentally friendly byproducts, Li-S offer many advantages from a commercial perspective when compared to many of its Li-ion counterparts. In addition, elemental sulfur itself is non-toxic making it better from a consumer perspective. [11] From a performance perspective, the Li-S reduction/oxidation reaction possess the highest theoretical capacity of any solid reduction/oxidation pair (1672 mA·h/g). It also possesses an energy density of 2600 W·h/kg. [12] This value is roughly five times the capacity of conventional Li-ion batteries.

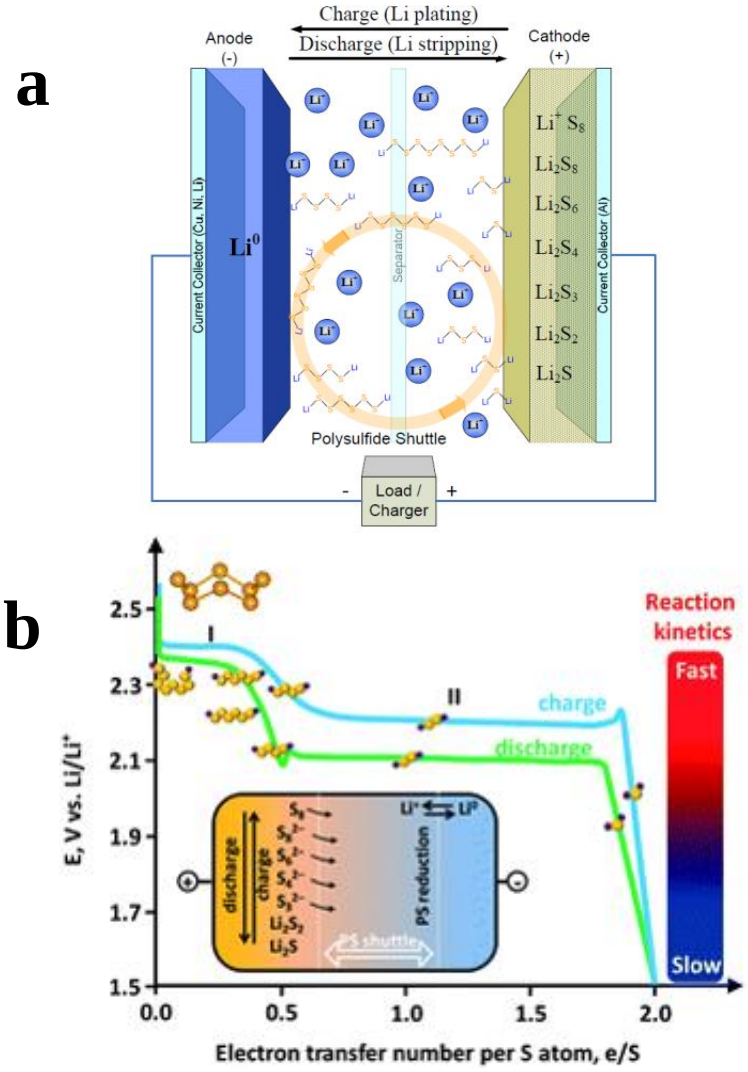

Figure 1.1: Lithium-sulfur battery cycling behavior. (**a**) Schematic of electrochemical cycling in lithium-sulfur batteries. [13] (**b**) Discharge curve for lithium-sulfur batteries showing two distinct plateaus at ~2.3 V and ~2.1 V associated with the formation of higher order and lower order polysulfides respectively. [14]

1.2.1 Electrochemistry

The electrochemistry associated with cycling of Li-S cells, differs from what is commonly discussed for other Li-ion technologies. A schematic of the charging/discharging process can be seen in Figure 1.1 Discharging occurs through a two electron reduction process at the cathode which converts cyclic octoatomic sulfur (S_8) to polysulfides (Li_2S_x; $1< x < 8$). The complete reaction can be seen in Eq. 1.2.

$$
\begin{aligned}
S_8 + 2Li^+ + 2e^- &\rightarrow Li_2S_8 \\
3Li_2S_8 + 2Li^+ + 2e^- &\rightarrow 4Li_2S_6 \qquad \text{Higher Order Polysulfides} \\
2Li_2S_6 + 2Li^+ + 2e^- &\rightarrow 3Li_2S_4 \\
Li_2S_4 + 2Li^+ + 2e^- &\rightarrow 2Li_2S_2 \qquad \text{Lower Order Polysulfides} \\
Li_2S_2 + 2Li^+ + 2e^- &\rightarrow 2Li_2S
\end{aligned}
\qquad \text{(Eq. 1.2)}
$$

The reduction process can be broken into two different regimes, which appear as distinct plateaus on the curve (Figure 1.1b). The first regime, which occurs at ~2.3 V, is associated with the production of higher order polysulfides (Li_2S_8, Li_2S_6, Li_2S_4, and Li_2S_3). The second regime occurs at ~2.1 V and further reduces the polysulfides to form Li_2S_2 and Li_2S. Higher order polysulfides are often soluble in the electrolyte, allowing them to diffuse into the electrolyte which can result in a loss of active sulfur in the cathode. If the higher order polysulfides reach the Li anode, they can be reduced forming Li_2S which leads to battery degradation. This process is known as *polysulfide shuttling* [15]. Lower order polysulfides are insoluble in the electrolyte and as a result, can prevent the polysulfide shuttle mechanism by acting as a diffusive

barrier. Conversely, these barriers can also act as an insulating layer preventing Li atoms from penetrating the cathode structure resulting in poor battery performance. Therefore, in the design of the cell, the main goal is to create a structure that is able to confine the polysulfides to the cathode side of the battery.

1.2.2 Anode Material

The most commonly used anode in Li-S batteries is the lithium metal foil, which offers a high theoretical capacity of 3860 mAh/g and a low electrochemical potential, 3.04V vs the standard hydrogen electrode [16]. These favorable electrochemical properties make it a highly attractive anode material to pair with sulfur. The extraction and redeposition of Li on the metal during cycling occurs through plating and stripping. This mechanism is less favorable than other intercalation materials such as graphite. Li metal anodes are plagued by the growth of Li dendrites which can penetrate the separator causing an electrical short. Given the high energy density of Li-S cells, this type of failure can prove to be catastrophic.

Inherent to all Li metal anodes is the formation of a solid electrolyte interphase (SEI) layer which is formed through reactions with the electrolyte. [17] This formation results in the deposition of a small film which acts as both an ionic conductor and an electronic insulator. While this process creates a more stable anode for cycling, it also results in the loss of active material. The amount of SEI formed, as well as its composition, depends strongly on the electrolyte being used. As a result, much work is being done to understand both the mechanism of formation, as well as, the electrochemical implications.

To lessen the effects of SEI formation and Li dendrite growth, a promising approach of using protective coatings of the Li anode are being studied and developed. Recently, Kozen et al., has demonstrated the ability to use atomic layer deposition, to deposit an Al_2O_3 protective layer, which protects the Li anode from corrosion, as well as, showing evidence for preventing parasitic effects from the polysulfide shuttle [18]. Results similar to this have further pushed the interest of utilizing a Li metal anode in not only Li-S cell, but other systems as well.

While the most popular choice of anode material is the Li metal, demonstrations of alternate anode candidates have also shown promise. Perhaps one of the most compelling demonstrations is the implementation of a prelithiated silicon nanowire to serve as the anode material. Silicon materials have received a large amount of attention as a potential anode material due to their high specific capacity of around 3500 mAh/g [19]. The main issue in employing a silicon anode is the volumetric expansion associated with the lithiation process resulting in an expansion of 400% [20] [21]. In 2011, an electrochemical cell using a prelithiated silicon nanowire anode and sulfur/mesoporous carbon cathode demonstrated an initial discharge capacity of greater than 1000 mAh/g. After 20 cycles, the capacity dropped to roughly 600 mAh/g. [22] Studies similar to this establish the possibility for a new, more stable anodes for the next generation of Li-S batteries.

1.2.3 Electrolyte

Different approaches have been taken to understand the electrolyte electrochemistry, but all variables are still being studied. [23][24]. More details on the

characterization of suitable electrolytes will be presented in Chapter 4. However, a brief introduction to the role of the electrolyte will be presented here. The general function of the electrolyte is to allow for the diffusion of Li^+ ions from one electrode to the other. Therefore, the first criterion in selecting a suitable electrolyte is a high ionic conductivity. Additionally, it should serve as an electronic insulator, preventing electrons from neutralizing the positively charged cations during their migration between electrodes. Stability is another concern related to the electrolyte, as degradation of the electrolyte can lead to a decrease in the ionic conductivity. This degradation is most influenced by the suitable voltage window of the electrolyte. [25]

Initially, traditional liquid organic electrolytes were used in Li-S batteries, but it was shown that these electrolytes possessed high polysulfide solubility. This leads to an increase in the polysulfide shuttle resulting to poor cycling performance. [26] As a result, work was done to alter the electrolyte to make the polysulfides less soluble within the electrolyte. However, it was shown that these alterations results in a decreased Li-ion mobility [26]. Therefore, the search for a suitable electrolyte which could suppress the shuttle, while maintaining the desirable characteristics of the electrolyte, remains a priority.

The most common liquid electrolyte currently used is lithium bistrifluoromethanesulfone imide (LiTFSI) in a 1,3-dioxolane (DOL)/dimethyoxyethane (DME). [27] The volumetric ratio between DOL and DME is typically 1:1. Using the so-called, solvent-in-salt electrolyte, 74% of the initial capacity of 1000 mAh/g was maintained over 100 cycles. Additional approaches include the use of $LiNO_3$. When added to the electrolyte, LiNO3 creates a passivating

film which decreases the effects of the polysulfide shuttle. [28] Similar to the anode coating, this process does not stop the polysulfide shuttle, but lessens the effects of the process. For the majority of our studies using a liquid cell, we utilized a LiTFSI/DOL/DME electrolyte with the $LiNO_3$ additive. Another approach is the transition from a liquid electrolyte to a solid electrolyte, but this significantly slows the transport.

1.2.4 Separator

The separator, as the name implies, separates the cathode and the anode component. Should the two electrodes come into contact, an electrical short will occur resulting in battery failure. While maintaining this gap, the separator should also allow for the easy diffusion of Li ions through it. Typically, some sort of porous polymer is used to serve this role. In addition to lithium diffusion, the separator can be used as a failsafe mechanism to the overcharging of the cell resulting from temperature changes. Upon heating, the polymer softens, closing the pores and preventing further diffusion of Li ions. Similar to the anode, protective coatings have been studied to suppress the shuttle effect. In the case of the separator, the coating should allow for the diffusion of Li ions, but prevent the diffusion of polysulfides. Various coatings such as Al_2O_3 [29] and a porous carbon interlayer [30] This carbon interlayer has shown the ability to improve cycle performance by restricting the polysulfides to the cathode side of the battery, while providing additional electrical pathways.

1.2.5 Cathode

A large portion of the research efforts related to Li-S batteries involves the optimization of the cathode component. Sulfur, an electrical insulator, should be incorporated into a conductive host structure to overcome its poor electrical conductivity. Most commonly, carbon is chosen to serve this role as it is lightweight, conductive, and chemically stable. In addition to increasing the electrical conductivity, these carbon structures provide structural integrity to accommodate the volumetric expansion which occurs during lithiation. The conversion of S_8 to Li_2S_8 during lithiation results in a volumetric expansion of roughly 80% due to the density difference of 2.07 g/cm^3 and 1.66 g/cm^3 respectively. [31]

A major breakthrough for carbon-sulfur composites came in 2009 when Nazar *et. al* used an ordered mesoporous carbon, CMK-3, filled with sulfur to demonstrate the ability of porous carbons to improve the Li-S battery's performance. They were able to achieve capacities of 1320 mA·h/kg, roughly 80% of sulfur's theoretical capacity. [32] Since then, much work has been done varying carbon types, pore sizes, and surface treatments to improve battery performance. The two main methods of carbon integration are through coating and filling. These methods are largely limited by processing conditions which could potentially interfere with the sulfur material [33]. Additional details of different carbon structures suitable for cathode materials in Li-S batteries will be covered in both Chapters 2 and 3.

1.3 Transmission Electron Microscopy

1.3.1 Background

When de Broglie theorized the wavelike behavior of electrons in 1925, the foundation for the development of an electron microscope was set. It was only seven years until the first publication demonstrating an electron microscope was completed by Ruska and Knoll. For this work Ruska was awarded the Nobel Prize in Physics in 1986 [34] [35]. Shortly after their publication, scientists were able to achieve a better resolution limit than the optical microscope. The rapid development of the technology continued with the first commercial microscope being developed in 1932. [36] Along with the development of the electron microscope, sample preparation methods were continually improved with the first electron transparent specimen being produced in the 1950s. [37] With this, the first demonstration of a transmission electron microscope (TEM) image was developed. In today's research, TEM has become an invaluable tool for understanding the properties of materials.

1.3.2 Basic Parts and Operation of TEM

The operating principles for TEM directly mimic the light microscope. Light microscopes produce images created from incident photons, while TEMs use electrons to create an image. Given that electrons have a much smaller wave length than visible light, electron microscopy allows for a much higher resolution, or minimum distinguishable distance between two features.

For ideal wave-optical systems, distance can be defined as:

$$\partial = \frac{1.22\ \lambda}{2 \cdot N.A.} \qquad \text{(Eq. 1.3)}$$

Where λ is the wavelength of the radiation and N.A. is the numerical aperture of the microscope. Therefore by saying the resolution is increasing, we are able to distinguish between two different objects at closer distances. This distance, typically measured in angstroms (Å), varies depending on the accelerating voltage. Using the accelerating voltage, or essentially the energy of the electrons, it is possible to calculate the wavelength of the emitted electrons.

$$\lambda = \frac{1.22}{E^{1/2}} \qquad \text{(Eq. 1.4)}$$

Where λ is the wavelength (nm) and E is the energy of the electron (eV).

TEMs capable of reaching above the theoretical resolution limit do not exist yet due to the inability to create a perfect lens. However, recent advances in aberration-corrected TEM have produced images with less than 1 Å resolution. [38] Prior to discussing these advances, a basic understanding of lenses and how the TEM operates as a whole, must be presented.

The previously used analogy comparing a TEM to a light microscope, gives an easy path to understanding what a TEM does in the simplest form. However, the components involved in producing a final image are entirely different. The generation of an electron beam results from an accelerating voltage is applied to extract an electron beam from an electron source known as an electron "gun".

The accelerating voltage is related to the electron wavelength through the following equation:

$$\lambda = \frac{h}{(2M_0 eV)^{1/2}} \qquad \text{(Eq. 1.5)}$$

Where h is Planck's constant, M is the rest mass of the electron, eV is the kinetic energy of the electron, and V is the accelerating voltage.

However, a more exact expression must be used for energies greater than 100 keV. Taking into account relativistic effects, Eq. 1.5 becomes:

$$\lambda = \frac{h}{[2M_0 eV(1+\frac{eV}{2m_0 c^2})]^{1/2}} \qquad \text{(Eq. 1.6)}$$

Equations 1.3 and 1.4 establish the inverse proportionality of the wavelength and the accelerating voltage. Therefore, by increasing the accelerating voltage, the wavelength is decreased, and the theoretical resolution limit is decreased. Higher accelerating voltages also created elevated risks for specimen damage. Therefore, it is necessary to use an appropriate accelerating voltage which allows imaging at appropriate scales without damaging the sample, or possibly, creating secondary reactions.

Two primary TEMs which were used throughout the course of these studies: the JEOL 2100 LaB_6 TEM and the JEOL 2100 FEG TEM (Figure 1.2). The two microscopes vary in their analytical capabilities due to differences in components, namely their emission source. The JEOL 2100 LaB_6 utilizes a thermionic emission electron source and the JEOL 2100 FEG utilizes a Schottky thermal field-emission electron source. The two methods are similar in that they produce a beam of electrons; however, due to their differences, each type has different capabilities.

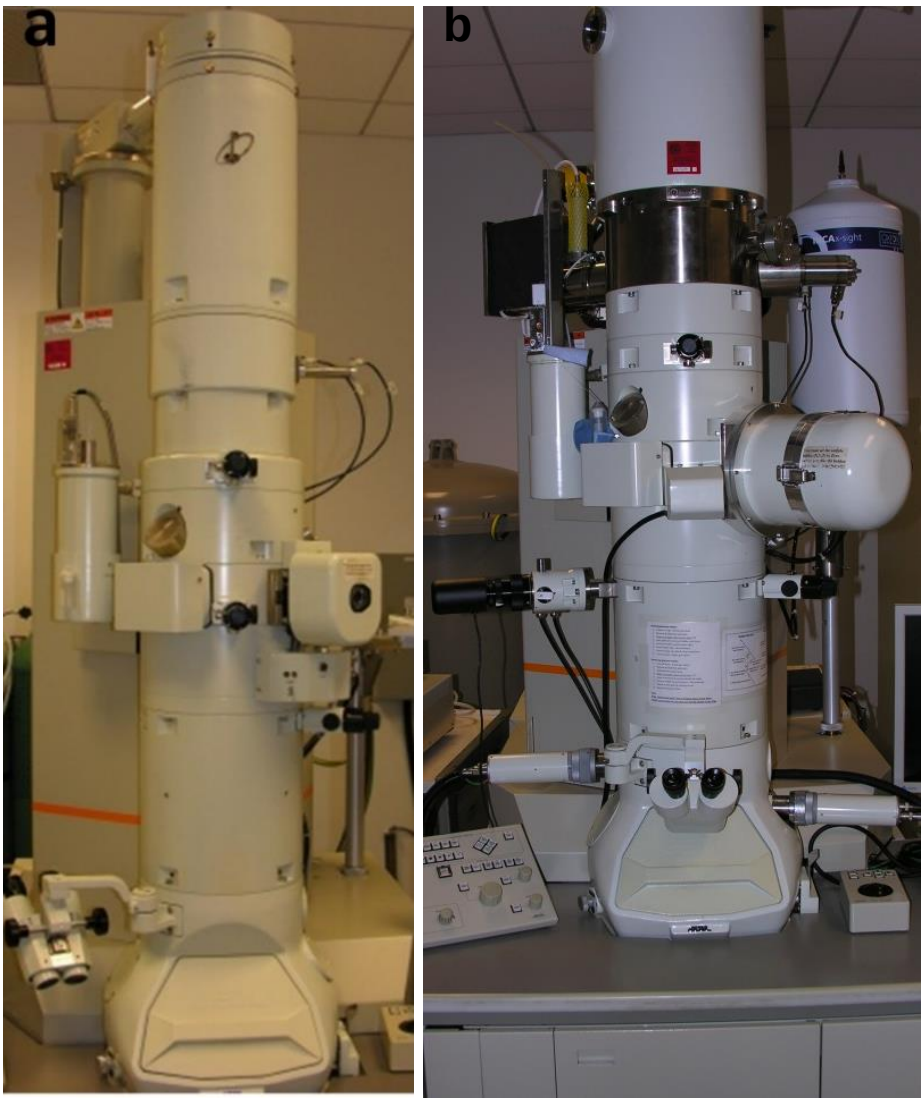

Figure 1.2: Transmission electron microscopes. (**a**) Image of JEOL 2100 LaB_6 TEM (**b**) Image of JEOL 2100 FEG TEM

Thermionic emission sources produce electrons through the heating of a crystal to high enough temperatures to give the electrons enough energy to overcome the crystal's work function (Φ). A potential difference is used to extract the highly energetic electrons. The JEOL 2100 LaB_6 utilizes a lanthanum hexaboride (LaB6) which is the most commonly used crystal for TEMs. The JEOL 2100 FEG utilizes a ZrO_2-coated tungsten tip of radius < 0.1 μm. Both emission sources can be seen in

Figure 1.3. The lenses used to vary slightly in that LaB_6 utilizes a Wehnelt cap to extract electrons and the FEG uses only two anodes. Typically, field-emission based TEMs are used for high-resolution imaging, as they provide a more coherent beam.

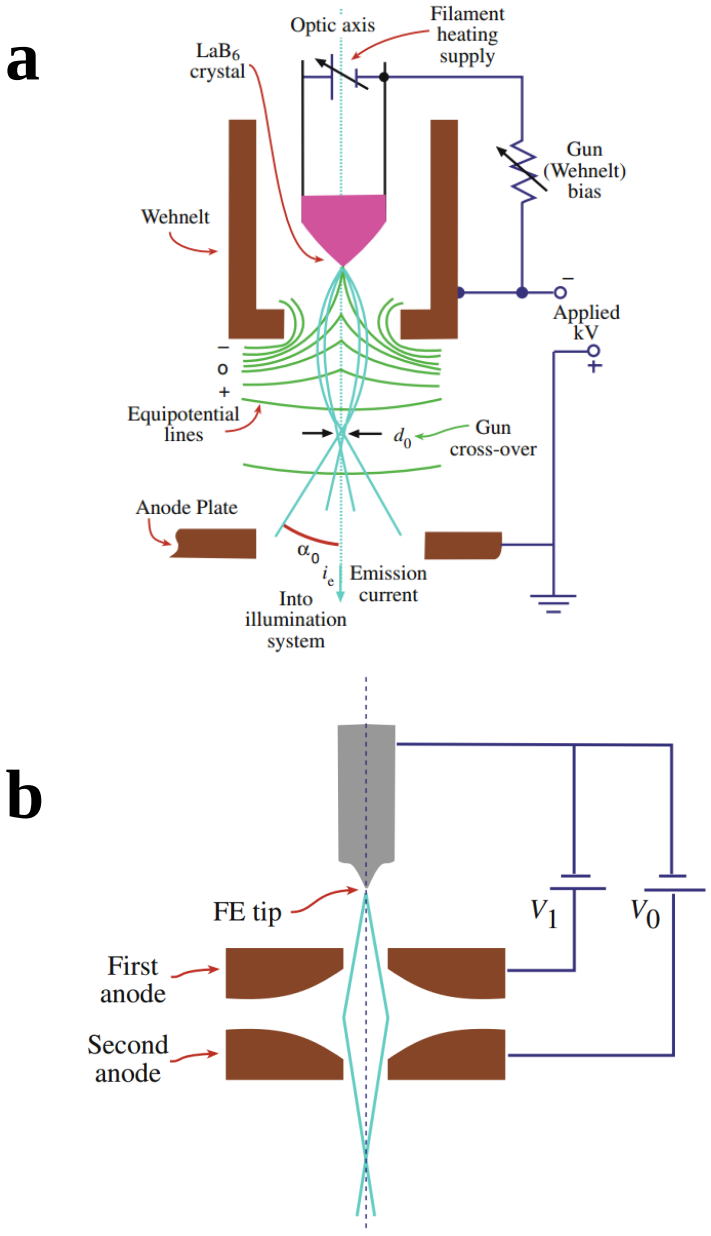

Figure 1.3: Emission sources for different electron sources. (**a**) Emission source for a LaB6 TEM (**b**) Emission source for FEG **[**39]

The next step of the electron's journey is the path down the TEM column. The column is under vacuum, (typically less than 10^{-4} Pa or 10^{-6} for FEG) to prevent collisions of the electron beam with gas molecules. Within the column is a set of lenses, which have the same function as the lenses within the light microscope, in that they are used to direct the path of the electrons prior to interacting with the specimen. A schematic ray-diagram can be seen in Figure 1.3b. However, they differ in that, instead of glass lenses, TEMs use electromagnetic lenses. In addition, instead of moving the lens vertically to adjust the focus, the strength (or current flowing through the lens) of the electromagnetic lenses are changed and the lenses themselves, are held stationary.

To understand the effect of electrons through the lenses, it is first necessary to understand how electrons interact with magnetic fields. Electrons experience a Lorentz (magnetic) force with strength equal to:

$$\boldsymbol{F} = q(\boldsymbol{v} \times \boldsymbol{B}) = -e(\boldsymbol{v} \times \boldsymbol{B}). \quad \text{(Eq. 1.6)}$$

Where q is the charge of the electron, v is the velocity of the electron, and B is the strength of the magnetic field. Within the velocity vector is a horizontal component, resulting from the electrons not entering the lens exactly at 90˚.

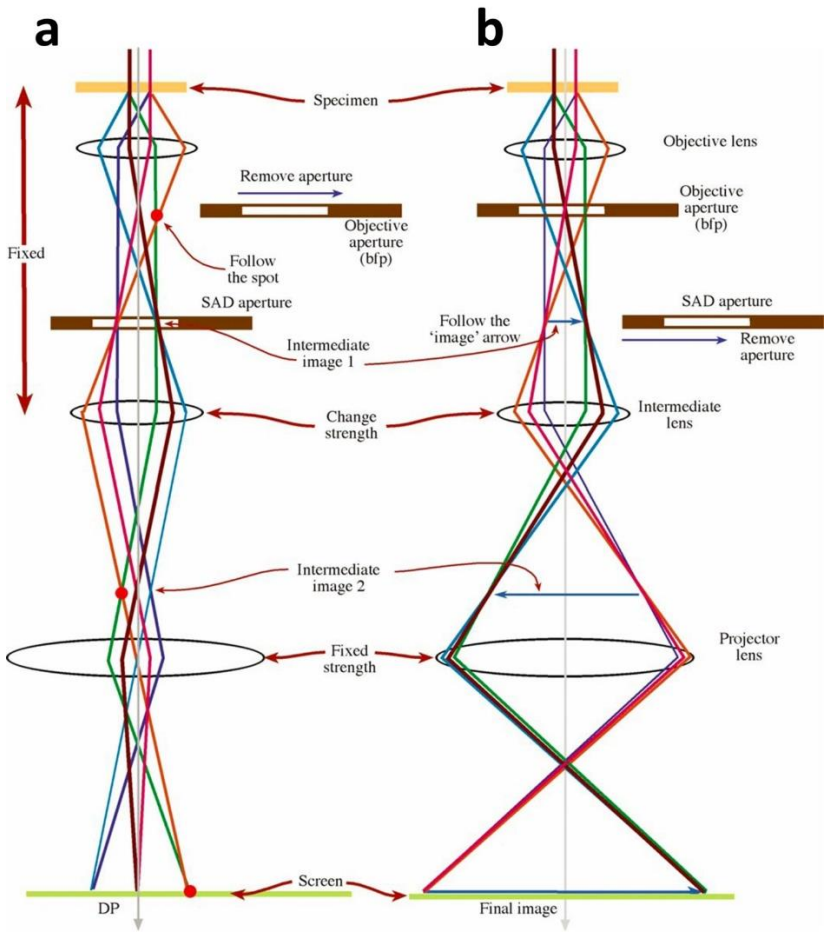

Figure 1.4: Two modes of imaging in TEM. (**a**) Diffraction pattern (DP) mode, and (**b**) Imaging mode. [39]

There are typically two major lens systems, the condenser lens system and the objective lens system. The condenser lens system consists of at least two lenses (C1 and C2). The first condenser lens (C1) produces an image of the gun crossover. The second condenser lens (C2) produces a parallel beam prior to interacting with the sample. The properties of the incident beam depend on both the electron source, and the strength and quality of the condenser lenses (It should be noted that in some cases, the upper objective lens is considered the C3 lens). Imperfections in the lenses, known as aberrations, can create distorted images, which decrease the resolution of

the microscope. There are three main "imperfections" associated with the condenser lenses, as well as, the other lenses of the microscope: spherical aberration, chromatic aberration, and astigmatism.

Spherical aberration occurs when there is an inhomogeneous lens field. As a result, electrons which are farther off-axis feel a stronger force from the lens than electrons closer to the optic axis. This results in a point source being displayed as a finite disk, caused by the irregular bending of electrons. Chromatic aberration arises from the inability of most TEMs to deliver a monochromatic electron beam, with energy variations depending on the emission source. Similar to spherical aberrations, the lenses affect electrons of different energies differently. Lower energy electrons are more strongly affected by the lenses than higher energy electrons. Astigmatism occurs when the magnetic field around the optic axis is irregular. As previously described, the electrons have a horizontal component to their velocity, so the electrons actually rotate around the optical axis while travelling down the column. In addition, defects in the soft magnet of the lens can cause an inhomogeneous magnetic field.

The objective lens is located directly under the sample and is responsible for creating both a diffraction pattern in the back focal plane and forming an image in the imaging plane. The intermediate lens is used to magnify the image. The projector lens then "projects" the image, or diffraction pattern, onto the viewing screen, or detector. The combination of the objective lens, intermediate lens, and projector lens is collectively known as the imaging system.

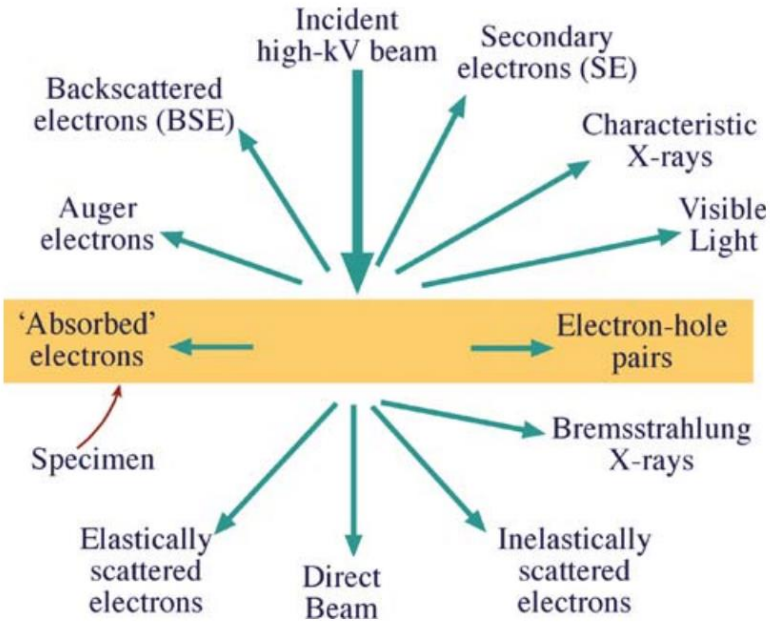

Figure 1.5: Summary of electron interactions with the specimen. [39]

Once an electron beam is generated, focused on the sample, the complex process of electron interaction begins. When an electron hits a sample a multitude of possible signals can be generated. Figure 1.5 summarizes these interactions. These signals enable the ability to study important materials properties such as structure, chemical composition, electronic states, and many others. The reactions responsible for these signals can generally be divided into three categories: interactions which produce x-rays, interactions which produce secondary electrons and interactions which cause interactions with multiple particles. These reactions and how they affect our samples will be discussed in their respective chapters.

X-rays can used to determine elemental composition of the specimen being studied. Typically, the process to generate x-rays results from an incident electron (from the beam) ejecting an inner shell electron (from the specimen), leaving the specimen in an excited state. The high energy state associated with an empty inner

shell leads to an outer shell electron filling the remaining hole. The transition to the lower energy state results in the release of an x-ray, whose energy is characteristic of the atom from which it was omitted. This process allows for the determination of local elemental composition of a structure in a TEM through a technique known as energy dispersive x-ray spectroscopy (EDS).

1.3.3 TEM Imaging of Sulfur

The main challenge with studying lithium-sulfur systems are the introduction of sulfur into the TEM. The typical operating pressure of the TEM column is around 10^{-7} kPa, depending on the TEM being used. When introducing sulfur into a TEM column, the well-known process of sulfur sublimation occurs. The reported results for the sublimation vapor pressure of orthorhombic sulfur range from 10^{-4} kPa to 10^{-9} kPa for temperatures ranging from 273.15K to 362.05K. [40] [41] [42] [43] [44]

Based on these results, the relationship between the vapor pressure of orthorhombic sulfur and temperature were established as:

$$p = \exp\left(A - \frac{B}{T}\right) \quad \text{(Eq. 1.7)}$$

Where p is the pressure in kPa, T is the temperature in K, A is a constant equal to 22.18± 0.93, and B/K = 109994.0 ± 331.8. This equation describes the vapor pressures of orthorhombic sulfur to a sulfur vapor at low pressures. It is possible for other reactions to occur such as a transition to a monoclinic phase, then subsequent sublimation. However, unless otherwise noted, sublimation will be considered to be the transition from the orthorhombic sulfur phase to sulfur vapor.

Given that the images observed are formed from the interaction of the sample with the electron beam, it is necessary to take into consideration the effects the beam has on the sample. When imaging sulfur in the TEM, it is evident that due to their ability to readily sublimate, additional energy provided by the beam could potentially induce other phase transitions. Recent reports by Barnaby et al., have suggested that TEM imaging of sulfur species could possibly induce a phase transition to a polymeric form. [45] We have demonstrated the ability to form polymeric form of sulfur which exhibits a π plasmon peak at 5.9eV (Figure 1.6a). Typically, this peak is due to the π plasmon of carbon. However, when looking at the high loss spectrum, there is a no carbon present. Therefore, the π plasmon peak results from a double bonding between sulfur atoms. To our knowledge, this is the first demonstration of this sulfur form. It is impossible to distinguish whether this phase transition results from the operating pressures of the TEM, or exposure to the beam.

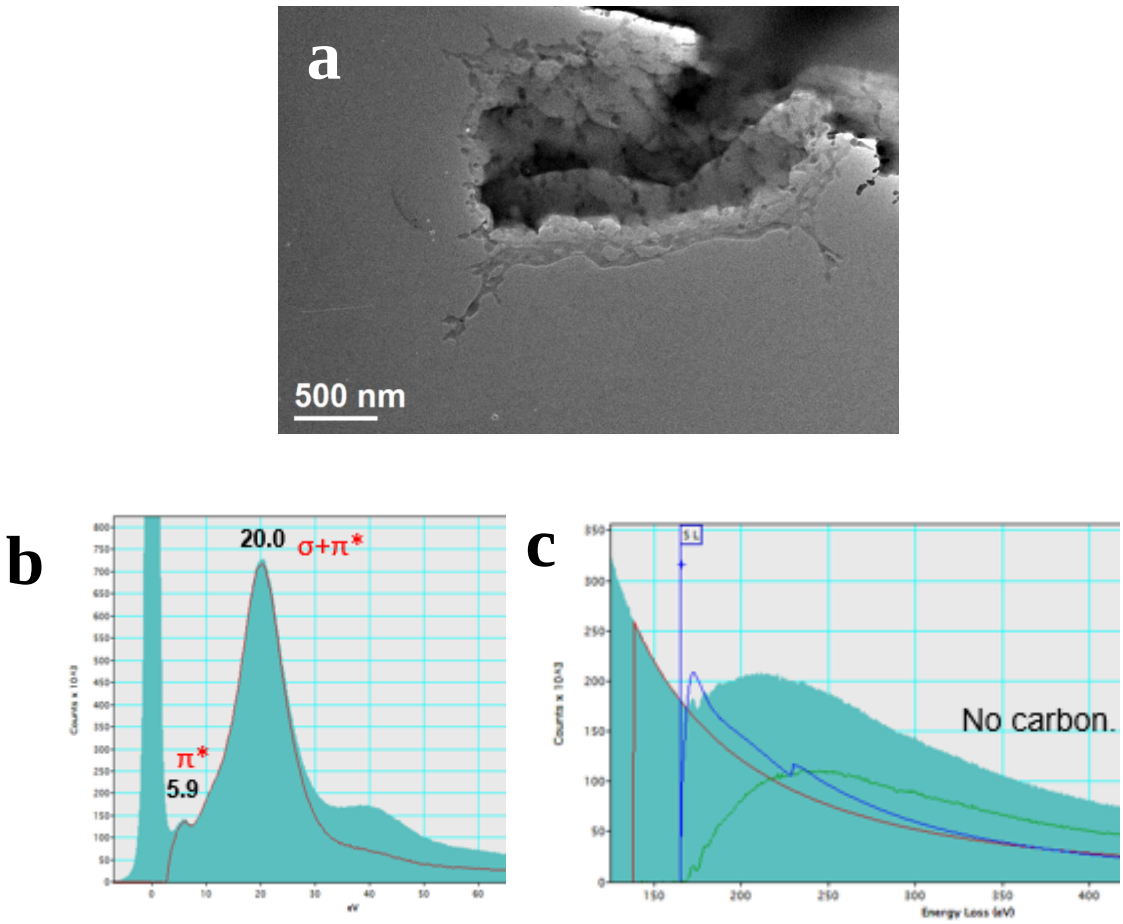

Figure 1.6: In-situ TEM polymerization of sulfur. (**a**) TEM image of partially sublimated sulfur crystal which is transitioning to a polymeric state. (**b**) Low-loss EELS spectrum taken from region in Figure 1.6a showing presence of π plasmon peak at 5.9 eV (**c**) High-loss EELS spectrum taken on same region in 1.6a showing the S $L_{2,3}$ edge at 165 eV. The C_K edge is not visible in the high-loss spectrum. Therefore, the π plasmon peak at 5.9 eV seen in Figure 1.6b is a feature of the polymerized sulfur.

1.3.4 Electron Beam Induced Effects

In addition to the sublimation of sulfur, there are other effects which can be affected by the beam. Beam damage is a primary concern with any sample that is placed within the path of the electron beam. The damage caused by the beam can be divided into three different categories: radiolysis, knock-on damage, and heating. Radiolysis occurs when the chemical bonds are broken by inelastic scattering. Knock-on damage is the most common form of beam damage and results when an atom is displaced by an incident electron creating an atomic vacancy site. When the atom is ejected from the sample, this type of damage is known as sputtering. The third type is heating, which arises from local atomic oscillations, known as phonons, which are generated by the incident beam. Each types of damage must be taken into consideration and minimized to ensure that the resulting reactions are unperturbed.

Lithium is primarily affected by knock-on damage. However, heating can also greatly affect the state of sulfur. As previously described, the phase transition from orthorhombic sulfur to sulfur vapor can occur at 145 ˚C at atmospheric pressure. Within the TEM column, sulfur is close to its vapor pressure, in most cases. Therefore, any small amount of heating caused by the beam can induce sublimation. For these reasons precautions were generally taken to minimize the beam dose on the sample.

1.4 Goal of Dissertation

While the potential of the Li-S electrochemical cell has been demonstrated in many different studies, there are still many issues that need to be overcome prior to

the widespread commercialization of this system. Methods for suppressing the parasitic reaction of the polysulfide shuttle and the formation of Li dendrites have been extensively studied using a variety of techniques. There still has been relatively little work done using transmission electron microscopy to probe the mechanisms that occur during battery cycling. This is largely due to the fact that sulfur is highly unstable and can potentially contaminate the TEM. Therefore, experimental procedures that allow for the use of TEM to analyze these processes still remain as a challenge.

For this dissertation work, I present the demonstration of multiple carbon/sulfur composite systems which allow for the study of different variables related to the electrochemical performance of the Li-S cell. In addition to TEM, scanning electron microscopy (SEM), Raman spectroscopy, x-ray diffraction, and other analytical techniques are used to investigate the reactions which occur during cycling.

1.5 Organization of Dissertation

The organization of the thesis is as follows. In Chapter 1, I will give a broad introduction to lithium-sulfur battery systems and transmission electron microscopy. In Chapter 2, I discuss our experiments in fabricating and characterizing a graphene/sulfur layered structure. In Chapter 3, our work studying the behavior of sulfur when confined to the interior of a single-walled carbon nanotube is presented. We present a direct relationship between the thermal oxidation prior to sulfur filling and the resulting electrochemical performance of the cell. Chapter 4 highlights

experiments studying multi-walled carbon nanotube/sulfur composites. An investigation of the degradation mechanisms of a Li_2S-P_2S_5 solid electrolyte is shown including the demonstration of cycling of an all-solid state Li-S nanobattery using in-situ TEM. In Chapter 6, we present a broader outlook of the topic, as well as, the future work for the research.

Chapter 2: Graphene/Sulfur Composites

2.1 Motivation

Graphene has been praised as a material which could revolutionize modern day electronics. [46] Possessing a high electrical conductivity, mechanical strength, thermal conductivity, among other exotic properties, interest in the material has grown exponentially in recent years. [47] All of these properties make it a suitable material to be employed as a cathode material. In addition to providing an electrical pathway for more efficient reaction kinetics, Zhou *et. al*, suggested that graphene can also serve as a barrier to suppress the outward diffusion of polysulfides into the electrolyte. [48] Their study showed a direct demonstration of graphene's ability to act as a physical barrier to suppress the polysulfide shuttle mechanism by directly correlating the decrease in capacity after cycling with the amount of sulfur present in the graphene coated separator. In addition to the graphene additive, the composite cathode relied on the use of carbon-black as well as a polymer binder. Therefore, we aim to explore alternate methods for creating a graphene/sulfur composite structure. In addition to the electrochemical benefits, we demonstrate that through the optimization of the fabrication of this structure, additional benefits related to electron microscopy are realized.

2.2 Graphene Structure

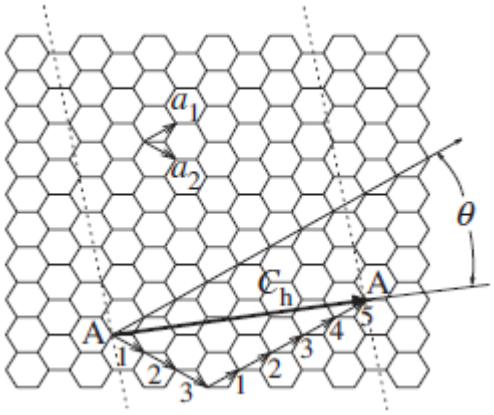

Figure 2.1: Lattice structure of graphene. Chiral vector (C_h) and corresponding basis vectors $\mathbf{a}_1$ and $\mathbf{a}_2$. [49]

Graphene is a two-dimensional monolayer network of carbon atoms arranged in a hexagonal honeycomb lattice. The structure of graphene ribbons are defined by the chiral vector C_h. Their chiral vector ($\mathbf{C}_h$) is of the form:

$$\boldsymbol{C_h} = n\boldsymbol{a_1} + m\boldsymbol{a_2} \quad \text{(Eq. 2.1)}$$

where (n,m) are the number of unit vectors, and $\mathbf{a_1}$ and $\mathbf{a}_2$ are the basis vectors. The chirality of the graphene ribbons dictates many of their properties, including electrical behavior. [50] The chiral vector can also be used to determine the edge structure which is either zigzag, or armchair. Zigzag edged graphene has the (n,m) indices of (n,0), while armchair edged sheets are (n,n). [49] The edge structure has also been shown to affect the electrical properties of the graphene ribbons. [51]

2.2 Graphene Synthesis

For laboratory research, graphene is an excellent material in that there are multiple inexpensive, relatively easy methods for producing high quality graphene. When scaling up to commercial production levels, the cost of producing high quality graphene increases. A summary of the different production methods relative to the cost are shown in Figure 2.2. The highest quality graphene is produced through mechanical exfoliation. This method, which is largely known as the "Scotch tape method", was first shown in 2004. [52] The gap between the performance of exfoliated graphene and other methods has diminished significantly. Here we will present a summary of the most commonly used techniques: exfoliation methods, epitaxial growth methods, and chemical vapor deposition (CVD).

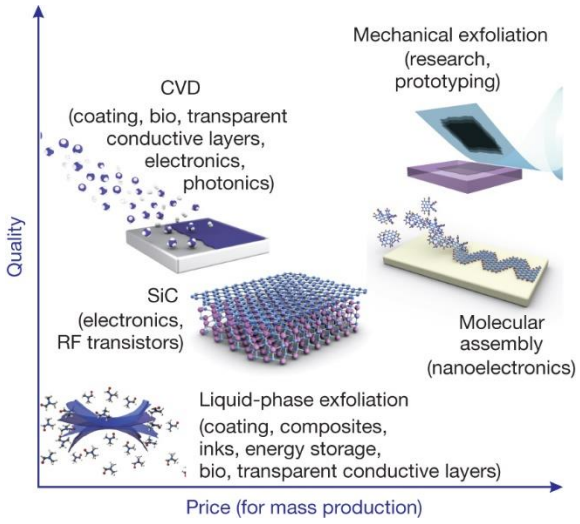

Figure 2.2: Quality versus price comparison for different graphene manufacturing techniques [53]

2.2.1 Exfoliation of Graphene

Exfoliation can be further broken into the subcategories of mechanical exfoliation and chemical exfoliation. Both methods result in the peeling away, or exfoliation of individual layers of graphene during treatment. Micromechanical cleavage uses an adhesive material to peel off single layers of graphene from a graphite material. While extraordinarily simple, the Scotch tape method revolutionized the study of graphene in a laboratory setting. [52] Mechanical exfoliation works through overcoming the van der Waals forces which exist between the graphite layers. Depiction of these two types of exfoliations can be seen in Figure 2.3. [54]

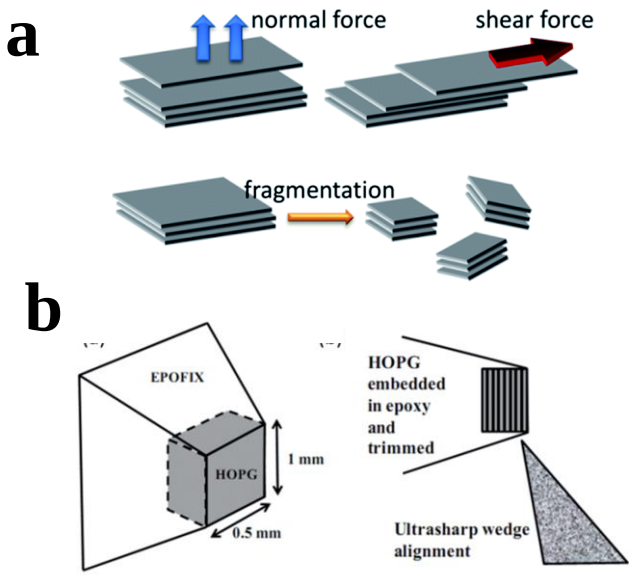

Figure 2.3 Mechanical exfoliation of graphene. (a) Exfoliation types and resulting fragmentation during exfoliation [53] (b) HOPG mounted in epoxy and trimmed to a pyramid shape. (b) Setup showing the wedge alignment with HOPG layers. (c) Actual experimental setup. [55]

2.2.2 Epitaxial Graphene Growth on SiC

The second type of graphene production is epitaxial growth on silicon carbide (SiC). This process is a thermal decomposition process in which a SiC surface is first etched atomically flat. Then the SiC is heated under vacuum resulting in the sublimation of silicon, leaving behind an epitaxial graphite layer. [56] This process was shown to occur at temperatures exceeding 1080 ˚C. At this point, it is possible to pattern the material, as well as deposit contacts for electrical measurements. [57] This method is a very popular method due to its ability to allow precise control of the number of graphene layers. [58] Due to the high conversion temperatures of this reaction, as well as the cost of the SiC material, this method can only be used in certain applications, which greatly restricts its potential commercial impact.

2.2.3 Chemical Vapor Deposition (CVD) Growth of Graphene

Chemical vapor deposition (CVD) is perhaps the most viable method of production when looking at commercial applications. As seen in Figure 2.1, it produces higher quality graphene at lower costs. Using this technique, large-scale synthesis has already been demonstrated, with the production of meter-scaled sheets being produced. [59] In addition to the scalability of the CVD process, the materials involved with the fabrication of graphene samples are inexpensive, and relatively easy to produce. Therefore, this method is already being explored for a variety of consumer products.

The working principle of chemical vapor deposition is the thermal decomposition of a precursor hydrocarbon gas by a catalyst metal. This is done at

elevated temperatures within a CVD furnace, the type of which depends on the catalyst material used for growth. The growth substrate can be broadly divided into materials with high and low carbon solubility. The growth mechanisms for each case can be seen in Figure 2.4. Using a method known as isotope labeling, in which the carbon source is alternated between ^{12}C and ^{13}C, the growth process can be experimentally observed. [60] Using Raman spectroscopy, the two different phases could be differentiated using the following equation:

$$\omega = \omega_{12}\sqrt{\frac{m_{12}}{n_{12}m_{12} + n_{13}m_{13}}} \quad \text{(Eq. 2.2)}$$

where ω_{12} is the Raman mode frequency of ^{12}C graphene/graphite, n_{12} and n_{13} are the atomic fractions, and m_{12} and m_{13} are the atomic masses for ^{12}C and ^{13}C, respectively.

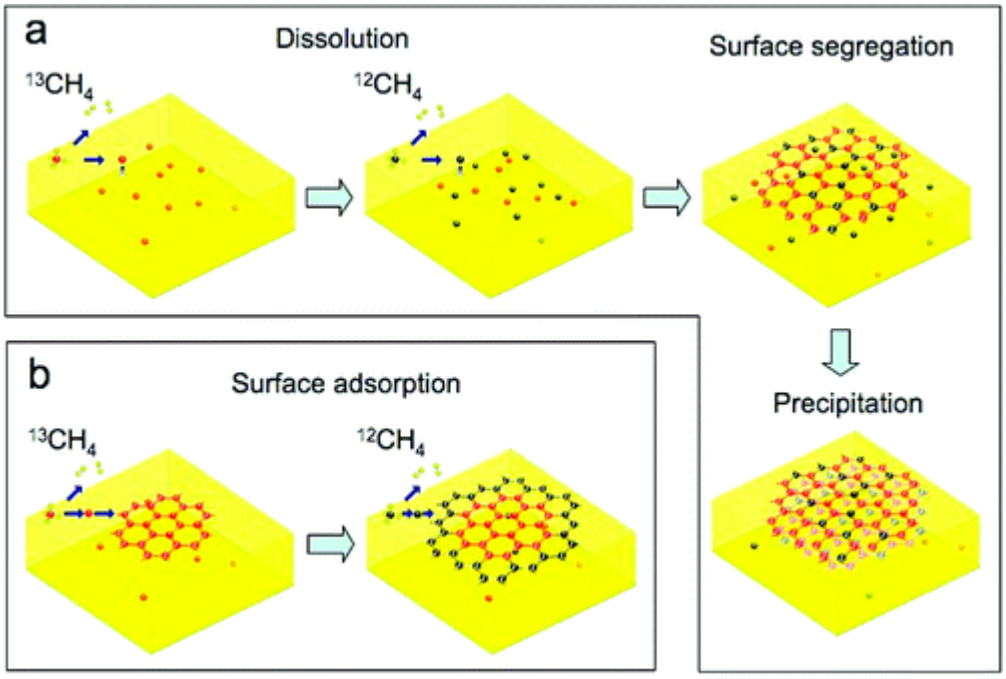

Figure 2.4 CVD Growth mechanisms of graphene. (a) Schematic diagrams of the possible distribution of C isotopes in graphene films based on different growth mechanisms for sequential input of C isotopes. (a) Graphene with randomly mixed isotopes such as might occur from surface segregation and/or precipitation. (b) Graphene with separated isotopes such as might occur by surface adsorption. [61]

Using these results, the growth process for high carbon-solubility catalyst metals is as follows. Following the carbon deposition onto the substrate, dissolution within the bulk material occurs. Following dissolution of carbon within the bulk material, two processes known as segregation [62] and precipitation [63] occur. Segregation can be defined as the change in the homogeneity of a through an increase in concentration of one of the components at an interface. [64] Once the carbon source is cut off, or the material approaches its carbon saturation limit, dissolution stops. The carbon segregates to the surface of the metal during the cooling process. It then crystallizes to form graphene layers, which is known as precipitation. The rate of

cooling and the resulting diffusion rate greatly affect the crystalline structure of the produced graphene. The most commonly used high carbon solubility material is nickel. It was shown that a faster cooling rate allows for the prevention of the formation of additional graphene layers. [65] Therefore, for high carbon solubility, a cold-wall reactor is typically used. This allows for the controlling of the cooling rate, in comparison to the hot-wall reactors which are used for low carbon solubility substrates.

The CVD process for low carbon solubility materials differs in that it is not a bulk process. Graphene growth results from, again, the breakdown of the hydrocarbon precursor gas, resulting in carbon adsorption on the surface of the catalyst metal. The negligible solubility of carbon within Cu removes the process of carbon dissolution. Therefore, the resulting graphene structure does not depend as strongly on the cooling rate. This process is also described as self-limiting in that once complete coverage of the catalyst metal is achieved, further decomposition of the hydrocarbon does not occur. [66]

Compared to exfoliation, CVD-grown graphene has a different structure associated with the deposition process. The largest benefit of mechanically exfoliated graphene is its single-crystalline structure. During CVD, the decomposition of hydrocarbons results in a nucleation process, followed by attachment onto those nucleation sites, leading to the eventual coalescence of a continuous graphene sheet. Due to misorientations of individual grains formed during coalescence, the boundary at which they meet is considered a defect. At these points, there is a drastic change in

the electrical properties, and these defects serve as scattering sites to electron transport. [67]

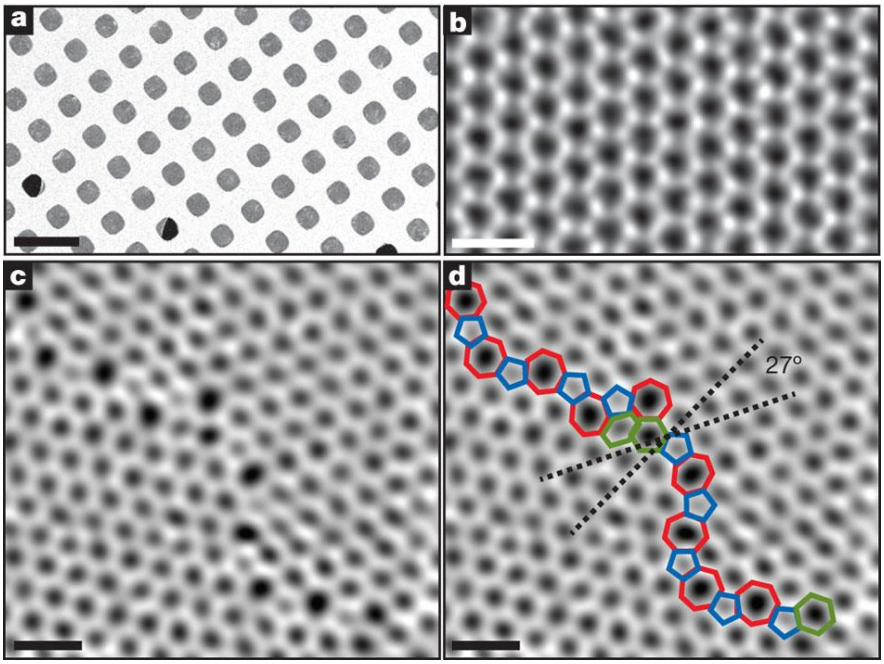

Figure 2.5. Grain boundaries in graphene. (**a**) Scanning electron microscope image of graphene transferred onto a TEM grid with over 90% coverage using novel, high-yield methods. Scale bar, 5 μm. (**b**) ADF-STEM image showing the defect-free hexagonal lattice inside a graphene grain. (**c**) Two grains (bottom left, top right) intersect with a 27° relative rotation. An aperiodic line of defects stitches the two grains together. (**d**) The image from c with the pentagons (blue), heptagons (red) and distorted hexagons (green) of the grain boundary outlined. (**b–d**) were low-pass-filtered to remove noise; scale bars, 5 Å. [68]

Using HRTEM, the individual grain boundary misorientations were studied by Muller et. al. When looking at an area within a single-crystalline grain, they show the individual atoms which make up the hexagonal structure. Figure 2.5 shows a HRTEM image of a grain boundary where two graphene grains coalesced. Due to their

misorientations, they form pentagon-hexagon pairs which are used to stich the two grains together.

This growth process was shown through the use of graphene seed cells, which were grown intermittently to form a complete graphene sheet. The results can be seen in Figure 2.6 which shows pre-patterned growth to better control this process. [69]

Using lithographically patterned graphene seed cells, they were able to precisely control and monitor the evolution of the graphene sheet using SEM. [69] This method was one of the first demonstrations of precise control of the grain boundary structure of graphene. Grain boundaries are the primary defect seen in CVD-grown graphene and result in the decreased performance of the graphene relative to their single-crystalline, mechanically exfoliated counterparts. Therefore, it is highly favorable to be able to control the amount of grain boundaries formed through the use of seed cells. Also, the possibility of controlling the orientation of these grain boundaries would allow for a better understanding of the scattering mechanisms that occur at each boundary type.

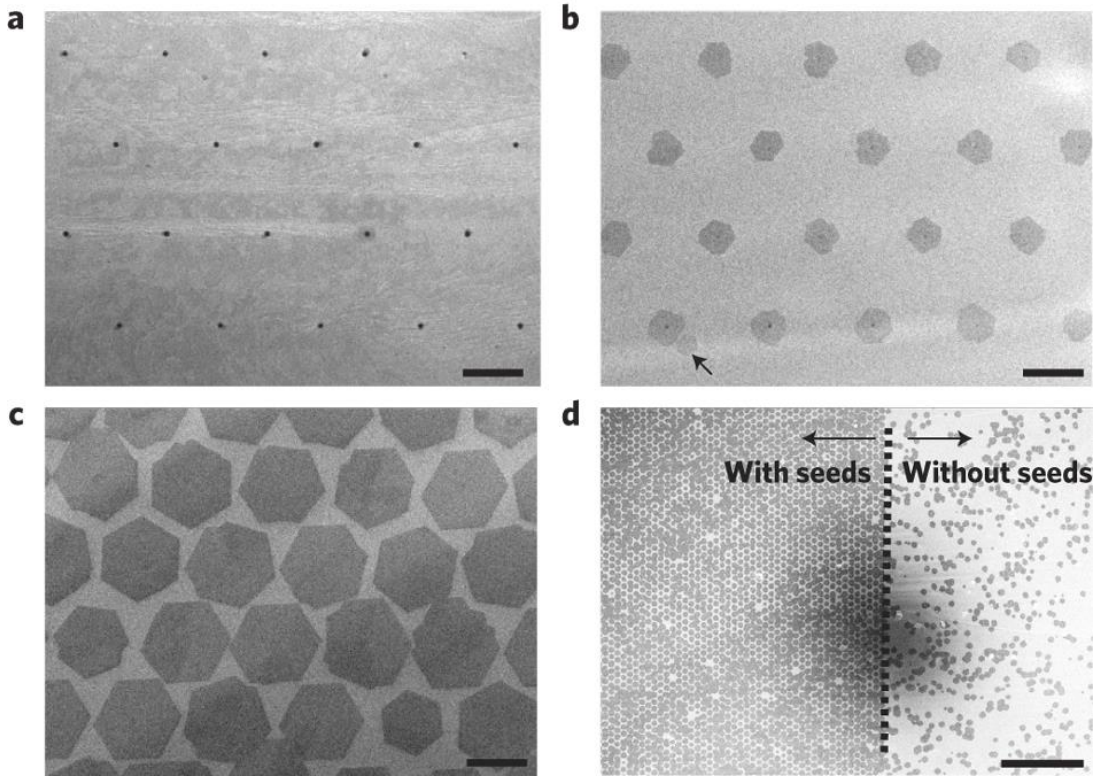

Figure 2.6: Graphene growth using a pre-patterned seed cell. (a), SEM image showing an array of seed crystals (seen as dots) patterned from a pre-grown multilayer graphene film on Cu foil by e-beam lithography. The period of the array is 16 μm. The size of each seed is about 500 nm. (**b**) SEM image of a typical graphene grain array grown from an array of seed crystals, with a relatively short growth time (5 min). The seeds can be seen at the centers of many grains. A grain that nucleated randomly (that is not from one of the pre-patterned seeds) is also observed (indicated by the arrow at the lower left). **(c)** SEM image of a graphene grain array from seeded growth similar to **b**, but following a longer growth time (15 min). The representative images **a**–**c** do not necessarily correspond to the exactly the same area on the Cu foil. (**d**) Low magnification SEM image of a seeded array of graphene grains (to the left of the dotted line), next to a randomly-nucleated set of graphene grains in an area without seeds (to the right of the dotted line). Scale bars in **a**–**c** are 10 μm and the scale bar in **d** is 200 μm. To reduce Cu surface defects that could create random (not from seeds) nucleation of graphene grains, the Cu foil was annealed for 3 h before the seeded growth. [69]

2.3 Transfer Procedures for Graphene

Despite the promise shown by the CVD technique, it requires the use of a transfer procedure to remove the graphene from the growth substrate and to deposit it onto a suitable substrate for the specific application. This step introduces the largest risk of damage during the CVD process. A commonly used technique for this step is a wet transfer process. This process can be summarized by the removal, or etching, of the underlying growth catalyst, followed by the deposition onto a suitable substrate. Typical chemical etchants used are $Fe(No_3)_3$, $FeCl_3$, and $(NH_4)_2S_2O_8$. [70] Following etching of the growth substrate, the sample is rinsed in DI water to remove any chemical etchant residue. Then the sample is scooped out of the DI bath onto the target substrate.

Typically, depending on the type of graphene grown, this transfer technique relies on the use of a polymer support. This support allows for the successful transfer with little damage to the underlying graphene. In selecting an appropriate polymer, it is necessary to choose a polymer which is chemically stable, flexible, and easily removed following the transfer process. One of the first polymers selected for this role was polydimethylsiloxane (PDMS). [71] PDMS was cast onto the graphene sheet (still on the Cu substrate) then placed into the chemical etchant. Following the etching, the PDMS/Graphene stack could be "stamped" onto the target substrate. The low adhesion force between the PDMS and graphene allow for the graphene to adhere to the target substrate, releasing it from the PDMS. The transfer process can be seen in Figure 2.7 [72] This material also offers the ability of lithographically patterning the stamped graphene during the transfer process.

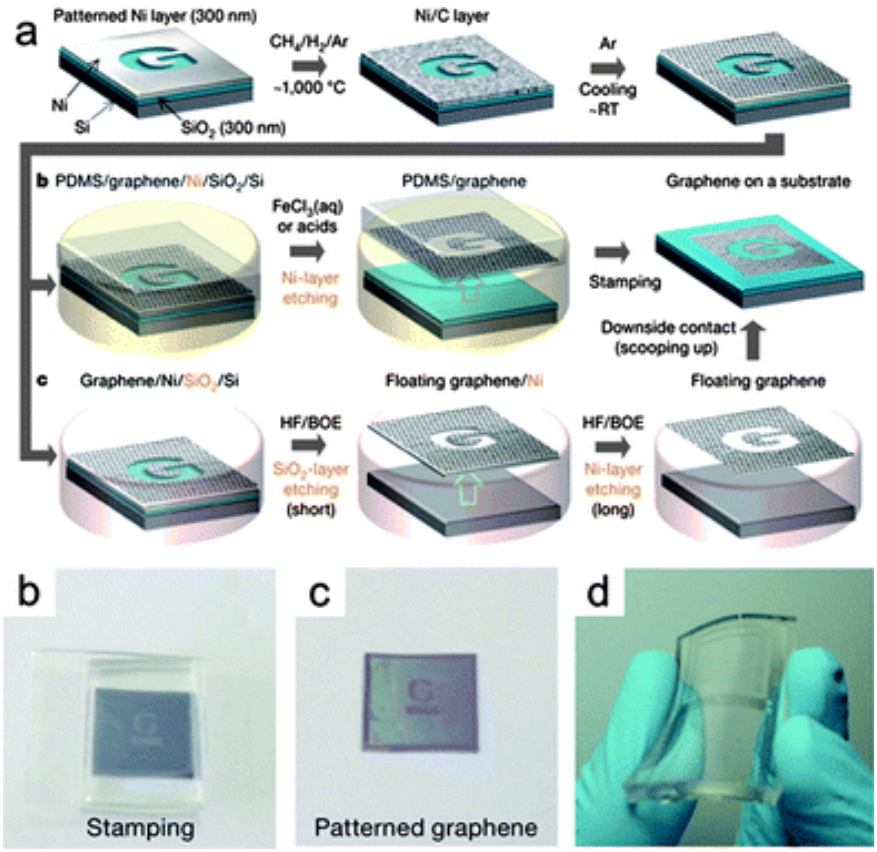

Figure 2.7: A dry transfer process for a graphene film grown on a Ni film using a soft substrate, PDMS. (**a**) Schematic illustration of synthesis, etching and transfer processes for patterned graphene films using a PDMS stamp. (**b–d**) Photograph images of graphene films. (**b**) Attaching the PDMS on a SiO_2 substrate. (**c**) Peeling the stamp and leaving the graphene film on the SiO_2 substrate. (**d**) Graphene electrode for transparent and flexible electronics fabricated by using patterning method. [72]

A second polymer widely used is polymethyl methaccrylate (PMMA). The transfer method can be seen in Figure 2.8. PMMA is spun onto the surface of the as-grown graphene on Cu, then placed in a chemical etchant to remove the metal catalyst. The Gr/PMMA stack is placed in a DI water bath to remove the etchant, then scooped onto the target substrate. In comparison to PDMS, the adhesion of PMMA is stronger. Therefore, it is possible for the PMMA to introduce rips and cracks into the

graphene sample. As a method to improve the transfer process, an additional step during the transfer process was proposed by Ruoff et al.

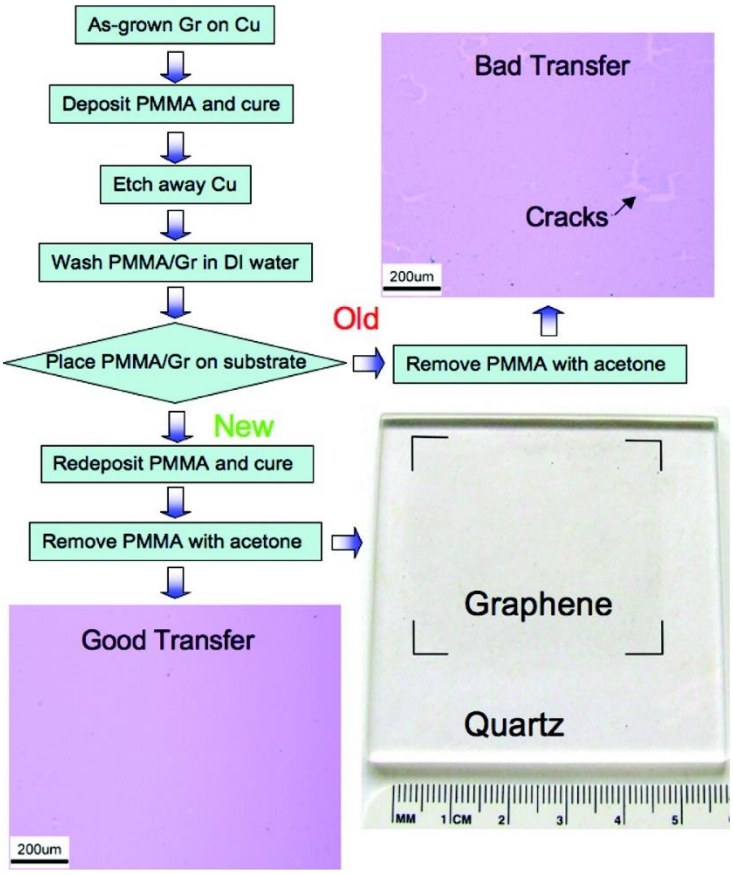

Figure 2.8: Processes for transfer of graphene films. The top-right and bottom-left insets are the optical micrographs of graphene transferred on SiO_2/Si wafers (285 nm thick SiO_2 layer) with "bad" and "good" transfer, respectively. The bottom-right is a photograph of a 4.5 × 4.5 cm^2 graphene on quartz substrate. [73]

The initial steps up until the removal of the PMMA remain the same, but PMMA is redeposited onto the PMMA/Gr stack after transfer to the target substrate. This allows for the stress relief of the PMMA, which releases the wrinkles formed in the graphene during the growth and cooling process. [73] This results in improved electrical performance and better overall transfer quality. The removal of the PMMA

can also be a point of damaging the graphene. PMMA can be removed by heat treatment above 400 ˚C under the flow of Ar and H_2 or the PMMA can be dissolved using acetone. This process can actually be rather challenging, in that residue from the PMMA often remains following treatment. Therefore, it is common to use a combination of both methods to ensure complete removal. However, residue formed during acetone rinsing or heat treatment should be examined closely during these processes.

A third method utilizes a thermal release tape to transfer graphene from the catalyst metal to the target substrate. This method has been demonstrated in the dry transfer of graphene from the SiC surface . [75] Similar to the PDMS stamping method, the adhesive tape is brought into contact with the as-grown graphene. A strong adhesive force peels away the graphene from the substrate, and it can then be put into contact with the target substrate. Using heat treatment, the graphene can be released from the tape and deposited onto the substrate. This technique allows for the capability of roll-to-roll transfer of large size graphene sheets. [59] Graphene sheets grown on a Cu foil roll were attached to the thermal release tape and placed into an etchant solution to remove the Cu. The remaining graphene/tape is placed in contact with a flexible substrate then extruded through two rollers which simultaneously applied heat and pressure. The heat releases the graphene from the tape which then adheres to the target substrate. This process was one of the most promising examples of scalable production of graphene.

2.4 Device Fabrication

2.4.1 Chemical Vapor Deposition (CVD)

The graphene used in our experiments is produced in an atmospheric pressure CVD system, shown in Figure 2.9. For our precursor gases, we used argon, methane, and hydrogen from Airgas. We use VWR high-purity two-stage regulators which control the pressure of the gas. Chemical resistant Tygon tubing is used between the regulators to the flowmeters. Three separate Omega flowmeters are used to control the precise flow rates for the different gases. Flow rates are most commonly measured in standard cubic centimeters (sccm). On the flow meters, the flow rates are scaled ranging from 0 – 150. The corresponding flow rates in sccm can be seen in Table 2.1. More details of the flow rates used for each type of graphene growth will be given later in this section.

Flowmeter Scale	Argon Flow Rate (sccm) (Omega 3805ST Flowmeter)	Hydrogen Flow Rate (sccm) (Omega 3802ST Flowmeter)	Methane Flow Rate (sccm) (Omega 3845ST Flowmeter)
10	351	89.9	5.8
20	932	133.6	8.1
30	1435	181.0	10.2
40	2003	241.8	12.9
50	2563	300.4	16.0
60	3107	358.0	19.4
70	3629	414.5	21.9
80	4185	472.5	25.8
90	4695	518.7	30.6
100	5233	561.8	345
110	5770	606.0	38.1
120	6308	658.0	43.3
130	6827	706.7	49.4
140	7369	763.5	54.5
150	7825	814.4	60.6

Table 2.1: Flowmeter reading and corresponding flow rates for gases used during CVD growth of graphene

For our CVD furnace, we used a Barnestead Thermolyne 21100 tube-furnace fitted with a 2116 PID temperature controller. Within the tube furnace, our samples are loaded on a quartz boat (Figure 2.9a), which is positioned in a quartz tube of 1-inch diameter. Given i9ts low carbon-solubility, and the high quality graphene it produces, we use copper as the metal catalyst, specifically, 25 μm thick Cu foils from Alfa Aesar.

To connect the hose to the quartz tube, we used KF25 flange components purchased from Duniway stockroom are used. Again, Tygon tubing is used to transport the exhaust gases from the tube furnace to the fume hood. Within the fume hood, an oil bubbler was used to prevent any exhaust gases from flowing back into the tube furnace. The tube was placed in the vacuum oil following the turn on of the first gas, then removed before all of the gases were turned off, to prevent any vacuum oil from being sucked into the tube.

Figure 2.9: Experimental set-up for CVD growth of graphene. (**a**) 25 μm thick Cu foil used as the catalyst metal during CVD on quartz boat (**b**) Atmospheric pressure CVD set-up used for the growth of graphene

The growth procedure for CVD consists of four steps: flush, ramp-up, growth, and cool down (and shut down). The first step, flushing, serves two purposes. First, it flushes out any atmospheric gases in the reaction chamber, creating a baseline environment for the CVD process. It also allows for the stabilization of flow rates prior to the growth process. For example, first introducing methane into the chamber by opening the tank valve produces a sudden rush of methane into the furnace. Flushing is done over 10 minutes with flow rates of 1435 sccm, 814.4 sccm, and 60.6 sccm for argon, hydrogen, and methane, respectively.

The next step is the gradual increase of the temperature within the CVD furnace to the final growth temperature. For this step, the methane is turned off, to prevent thermal decomposition of the gas prior to reaching the desired growth temperature. Typically, a ramping rate of 17 ˚C/min is used; this translates to an hour ramp time to reach the growth temperature of 1000 ˚C, which is most commonly used. We have gained a good understanding of the growth conditions for our setup that yield the various types of graphene. Our initial efforts focused on the replication of the growth procedures for different published results. It was quickly determined that the reported parameters for high-quality, single-layer graphene in other setups did not yield the same results on our setup. Cool down initially achieved by turning off the power supply and allowing the setup to return to room temperature. In order to increase the cooling rate, the quartz tube was later pulled from the furnace in order to

take the sample out from the heating zone. The gas flow rates for H_2 and CH_4 were returned back to the same rates of 1435 sccm and 814.4 sccm, similar to the ramp procedure. The shutdown procedure is a reverse shut down process in which the CH_4 and hydrogen were shut off. Then, the Ar was used to flush the tube of any residual H_2 or CH_4 gases. The sample is then removed from the tube furnace for transfer to a suitable substrate. These modified procedures produced results more consistent with the literature.

2.4.2 Transfer Procedure

The transfer procedure is undoubtedly the step which introduces the most variability in the graphene fabrication process. The first step of spin coating PMMA on the Cu foils was done using the SCS G3 Spin coater. Our initial attempts using an acceleration time of 5 seconds, spin speed of 6000 rotations per minute (RPMs) for 15 seconds, and a deceleration time of 5 seconds. Following spinning, the PMMA was cured at 150 ˚C for 20 minutes on a hot plate. This recipe was adapted from the PMMA curing procedure that we use for PMMA curing on silicon nitride TEM membranes for electron-beam lithography. As a result, the PMMA layer was extremely thin. We found that the PMMA offered little to no support and most of the transfer processes were unsuccessful. In addition to the PMMA being too thin, any wrinkles on the Cu foil result in an inhomogeneous deposition of PMMA. Areas beyond the ridges of the Cu foil were then not covered in PMMA. As a result, once the Cu was etched in solution, the graphene sheets would be separated into smaller graphene flakes. These smaller graphene flakes were suitable for certain experiments,

such as TEM characterization. However, our experimental plans required much larger sheets of graphene, so more work was done to optimize the transfer procedure.

The first step to be altered was the spin speed of the PMMA. Using different spin speeds, both the ease of transfer as well as the ease of removal was studied. Following numerous attempts at different spin speeds, acceleration times, and PMMA types, a standard protocol for transferring our CVD grown graphene was established. A spin speed of 4500 rpm was used, with an acceleration and deceleration time of 15 s. Also, instead of using a hot plate to cure the PMMA, the curing was done at 150 ˚C in an oven. Given that our previous methodology for spin-coating PMMA was derived from a process for SiN membranes, the transfer of heat to the substrate is much more uniform. In comparison to the SiN membranes, the entire Cu foil is not in contact with the glass slide, resulting in non-uniform curing of the PMMA. Therefore, the oven was expected to provide better curing of the entire Cu foil.

Another change that was made from our initial experiments was the chemical etchant used. During our preliminary growth and transfer processes, we used $FeCl_3$. However, for the majority of our etching processes, there was incomplete etching of the Cu substrate. Small patches of Cu still remained when leaving the PMMA/Gr/Cu stack in FeCl3 for up to 12 hours. Of the other possible etchants, we selected ammonium persulfate $(NH_4)_2S_2O_8$ which showed more complete removal of Cu in a much shorter time, allowing for a more efficient transfer process.

The above process was used primarily for the characterization of graphene to optimize the growth parameters used during each experiment. When we sought to create layered structures for characterizing graphene/sulfur cathode materials, we

have adapted both the growth process, and the transfer process, to ensure that the sulfur would survive. Sulfur, which has a low evaporation temperature of ~145 ˚C, would not survive the heat treatment to remove the PMMA support. In addition, acetone would likely remove sulfur from the system. Therefore, a method which did not utilize a polymer support was developed.

Initial attempts to perform a polymer-less support transfer using monolayer graphene were unsuccessful. The Cu catalyst metal would etch successfully, but any agitations to the solution in which the sample was floating, resulted in the breaking of the graphene sheet into many, small graphene flakes. Therefore, growth parameters were changed to increase the number of layers grown during the CVD process. The inter layer van der Waals forces were expected to improve the graphene's stability.

2.4.3 Sulfur Incorporation

To incorporate sulfur into the graphene structures, we used a simple thermal evaporation process. Following transfer onto the desired substrate, we placed sulfur powder in a glass dish. We mounted the sample directly above the sulfur powder and placed the entire glass dish on a hot plate. The sample was then heated to 160 ˚C allowing for the evaporation of sulfur. Following evaporation a second layer of graphene was transferred to the structure using the same transfer technique. (Figure 2.10)

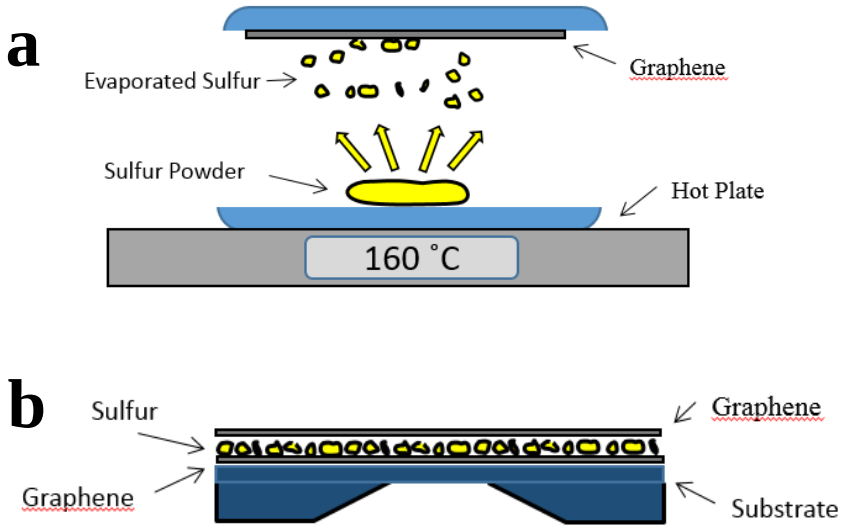

Figure 2.10: Sulfur evaporation onto graphene. (**a**) Schematic of graphene evaporation configuration (**b**) Schematic of the graphene layered structure

2.5 Results and Discussion

Using the previously described processes, we have fabricated novel graphene/sulfur layered structures which could serve as a cathode material. By varying the growth parameters, we were able to grow graphene that is capable of withstanding the transfer process without utilizing a polymer support. Following the initial transfer of FLG, sulfur was evaporated onto the graphene surface. An additional graphene layer was transferred onto the graphene/sulfur material. This complete layered structure enabled the use of transmission electron microscopy. This, to our knowledge, is the first demonstration of high-resolution TEM imaging of sulfur, which normally evaporates very quickly during electron microscopy studies.

2.5.2 Scanning Electron Microscopy

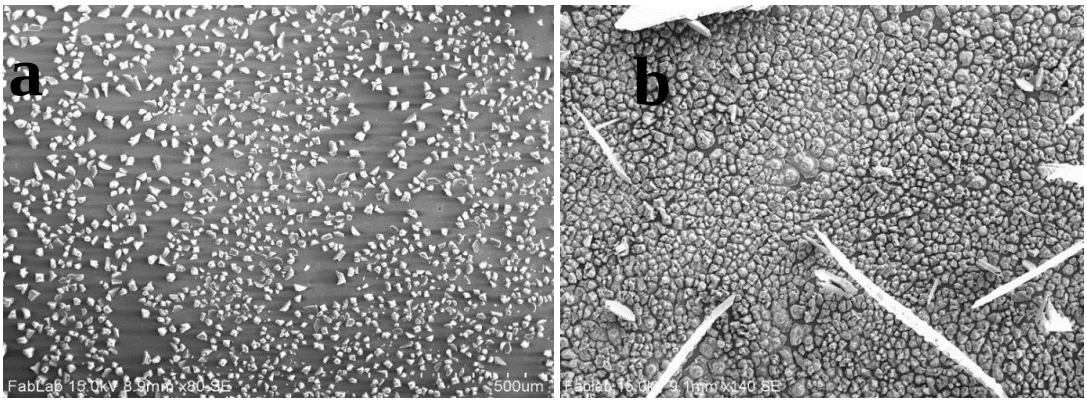

Figure 2.11: Graphene/Sulfur composite materials following thermal evaporation onto the underlying graphene. (**a**) Thermal evaporation of sulfur at 160 ˚C for 4 hours. (**b**) Thermal evaporation of sulfur at 160 ˚C for 6 hours

Scanning electron microscopy (SEM) was used to image the structure during different points in the fabrication process. Our initial studies were performed by transferring graphene to a Si/SiO_2 substrate. We found that it is possible to change both the size and density of the crystals by changing the evaporation time. For shorter times, the crystals were more densely packed. Using a time of 4 hours (Figure 2.8a), we were able to see complete coverage of the sample. However, the density of the sulfur crystals is relatively low. When we increased the time to 6 hours (Figure 2.8b), we saw a dramatic increase in the density of sulfur crystals. At this time, we also observed a change in the structure of the material. We suspect that the enhanced thermal conductivity of graphene, relative to the Si substrate, changes the cooling process and resulting crystallization.

When looking at the interface between the SiO_2 and the graphene, a striking difference between the structures of the sulfur. These differences were used to determine the success of the graphene transfer process. We defined success of the

graphene transfer, as the continuity of the transferred graphene sheet. Therefore, we aimed to achieve a homogeneous distribution of crystal types throughout the entire sample.

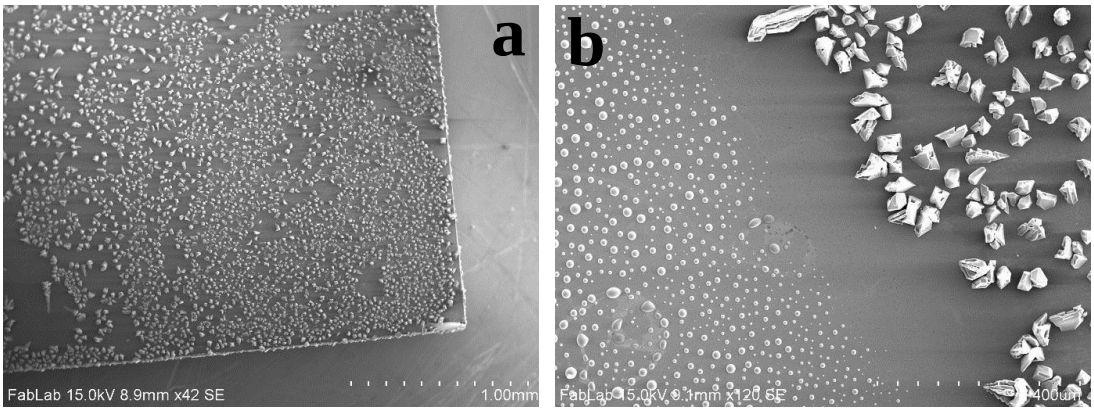

Figure 2.12: SEM micrographs showing sulfur deposited onto a graphene layer using a Si/SiO2 substrate. (**a**) Low magnification image showing inhomogeneity caused by discontinuities of the underlying graphene (**b**) Interface between graphene and bare Si/SiO2 substrate showing different structures of sulfur crystallization

Following the transfer of the second layer, the graphene layer can be seen using SEM. This was unavoidable and was apparent in all of the samples. However, it is possible to see good contact between the graphene and sulfur in areas which we have complete coverage. Using EDS spectra, we were able to confirm that the crystals seen on the surface were pure sulfur (Figure 2.10c). The difference in intensity between areas which have holes and areas which have complete coverage validates our claims that we have complete graphene coverage. We also saw that the sulfur crystals were capable of creating new tears within the sample.

b

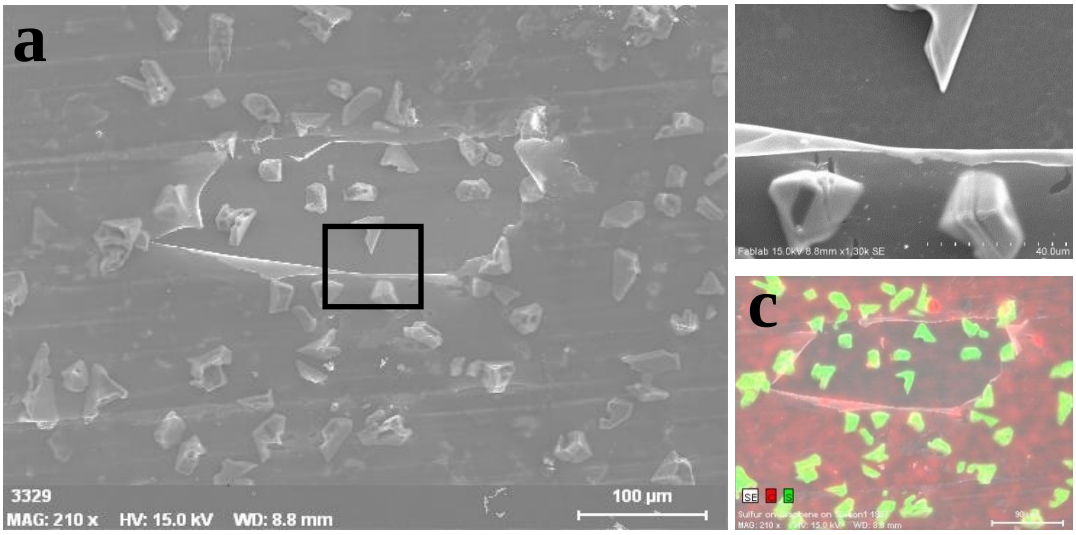

Figure 2.13: SEM micrograph of completed graphene/sulfur layered structure. (**a**) Low magnification of structure showing an area with a tear in the top layer of graphene. (**b**) Higher magnification image of area highlighted in **a**. (**c**) EDS mapping of Figure **a**. Sulfur (green); Carbon (red).

2.5.3 Transmission Electron Microscopy

TEM studies of sulfur are limited. Given the ability of sulfur to sublimate at the operating pressures of traditional TEMs, there exists a very small body of knowledge on the TEM imaging of sulfur. More detail on the instability of sulfur is presented in Chapter 4. The previously described methods were used to create graphene/sulfur structures on holey carbon TEM grids. High angle annular dark field (HAADF) image of Figure 2.11a shows the morphology of the structure. Graphene layers which have folded onto themselves are evident throughout the sample are also visible in our SEM characterization. These folds are created during the transfer process. The larger sulfur crystals which were seen on the samples which were fabricated on the SiO_2 sample were not visible. Through electron energy loss spectroscopy (EELS), we confirmed that both carbon and sulfur are present in our system. Figure 2.11(b-g)

highlights our EELS analysis in verifying the composition of the structure. It shows the distribution of carbon from the graphene, sulfur, and silicon which was introduced during the transfer process.

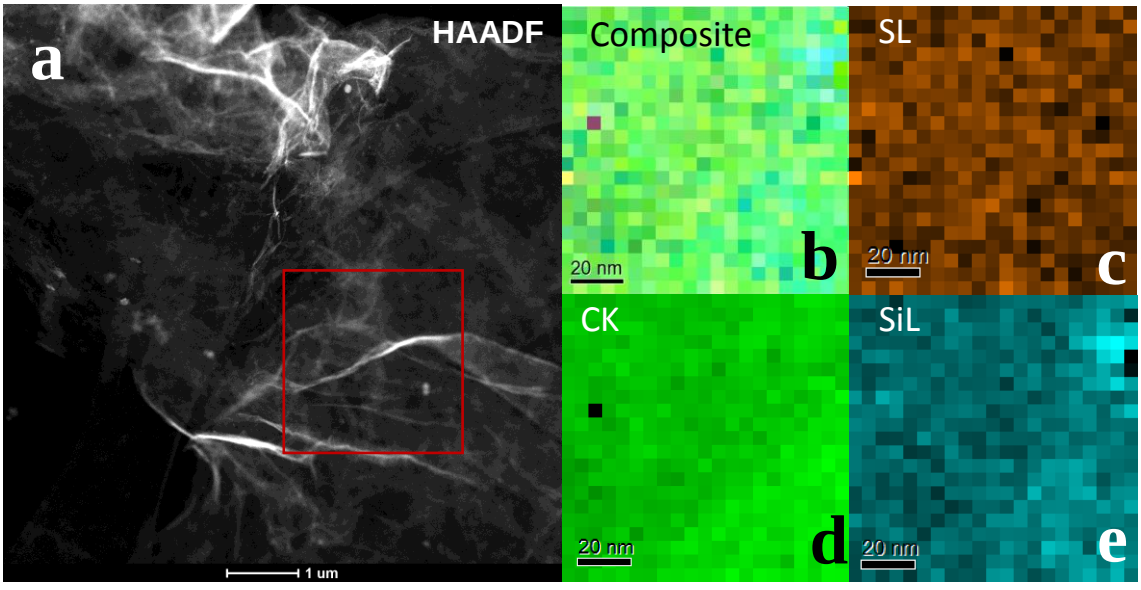

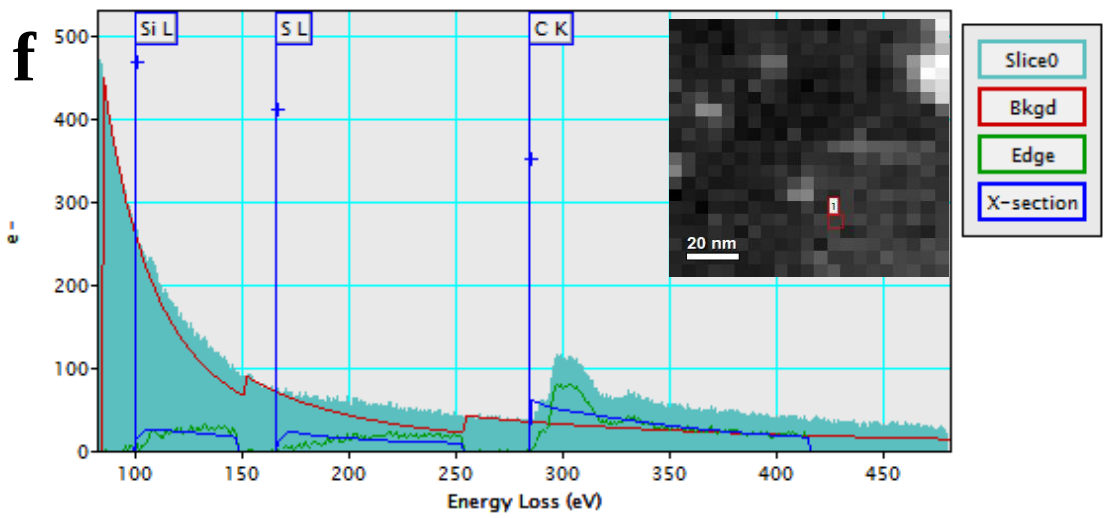

Figure 2.14: EELS spectral imaging on graphene/sulfur composites. (**a**) HAADF image taken in STEM mode (**b**) Spectrum from area highlighted during STEM imaging mode taken from a sulfur nanocrystal.(**c**) Composite spectral image of SL, CK, SiL spectral images (**d**) Spectral image taken from SL edge (**e**) Spectral image taken from CK edge (**f**) Spectral image taken from SiL edge (**g**) EELS spectrum taken from region of interest highlighted within the inset micrograph

These structures enable the ability to image sulfur using HRTEM. Using HRTEM, we were able to characterize individual nanocrystals of sulfur embedded between two layers of graphene (Figure 2.12a). Using FFT, the corresponding diffraction points can be labeled and assigned to both sulfur (Figure 2.12b) and graphene (Figure 2.12c). To our knowledge, the HRTEM lattice imaging of sulfur has not previously been reported. This clearly proves the benefit of using a structure similar to the layered structure and greatly expanded the number of analytical TEM techniques which we were able to perform on sulfur.

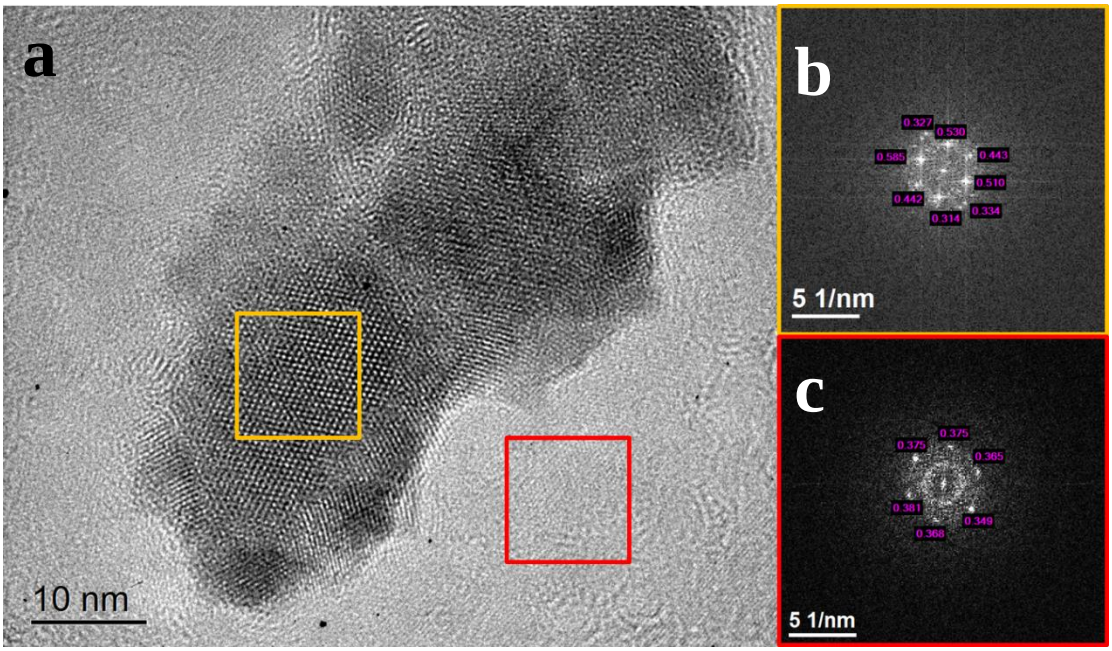

Figure 2.15: HRTEM imaging of sulfur crystal encapsulated within two graphene layers. (**a**) HRTEM image showing sulfur crystal lattice fringes (**b**) FFT showing DP for sulfur crystal (Yellow Box) (**c**) FFT of graphene area (Red box)

Further analysis of the HRTEM can be seen in Figure 2.13. Figure 2.13a shows a graphene/sulfur layered structure. Distinct lines can be seen showing discontinuities, or folds, within the graphene layers. Even at low magnifications,

visible lattice fringes can be seen on the larger darker sulfur particles. HRTEM lattice fringe spacing of the sulfur nanoparticles can be seen in Figure 2.13b-c.

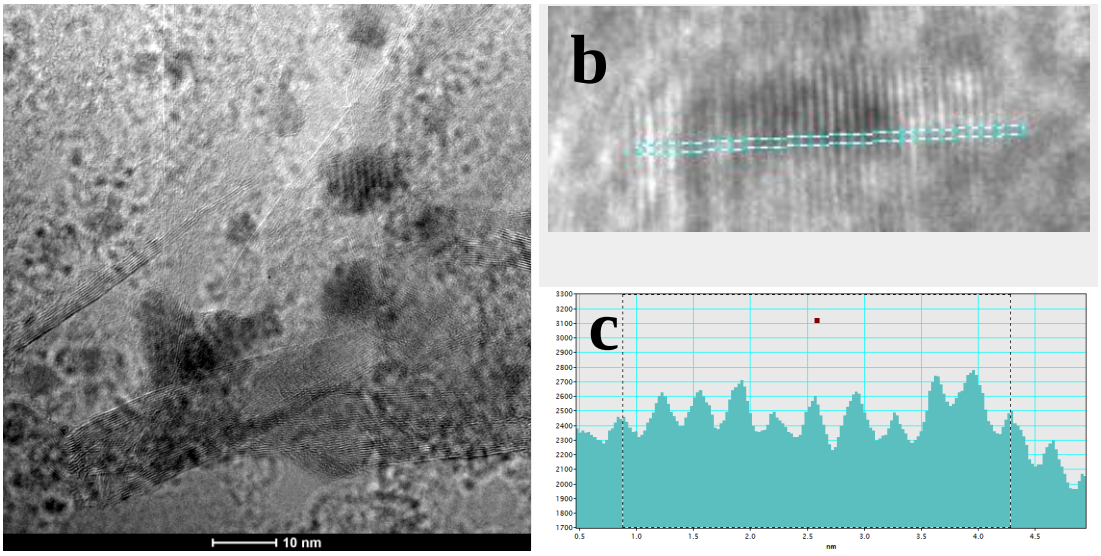

Figure 2.16: HRTEM imaging of graphene/sulfur composite. (**a**) STEM Imaging of graphene layers with sulfur particles within the sample EELS Spectrum from area highlighted during STEM imaging mode (**b**) HRTEM lattice fringe image (**c**) Intensity profile corresponding to the area of interest shown in **b**

2.6 Summary

Here we have presented a method for the creation of a layered structure consisting of sulfur sandwiched between two graphene layers. Graphene acts as a protective layer which prevents the sublimation of sulfur at the operating conditions of conventional TEMs. The creation of this structure has allowed for a multitude of analytical techniques used to characterize sulfur. We hope to utilize this structure for various in-situ techniques studying both the electrochemical performance, as well, as, intrinsic properties of related to sulfur.

Chapter 3: Sulfur-filled SWCNTs

3.1 Motivation

The lithium-sulfur (Li-S) cell has shown great promise as a candidate to replace currently utilized Li-ion technology based on a $LiCoO_2$ cathode. From a commercial standpoint, it is earth abundant, inexpensive and outperforms the theoretical limitations of traditional Li-ion technologies with a specific capacity of 2672 mAh/g and an energy density of roughly 2600 Wh/kg. [12] Despite its promise, it still suffers from poor performance resulting from both sulfur's low electrical conductivity as well as its cycle degradation through the formation of polysulfides. [15] As a result, much work has been done to develop systems to overcome these issues. Carbon nanotubes (CNTs) have been shown to behave exceptionally when employed in this role offering high thermal and electrical conductivities [75] [76] , good mechanical properties [77] and a variety of other qualities. [78] Their high surface area provides a large electrochemical interface suitable for the lithium/sulfur reaction. In addition, their inner cavities provide an additional site for sulfur packing, which would increase the overall energy density of a battery. [79]

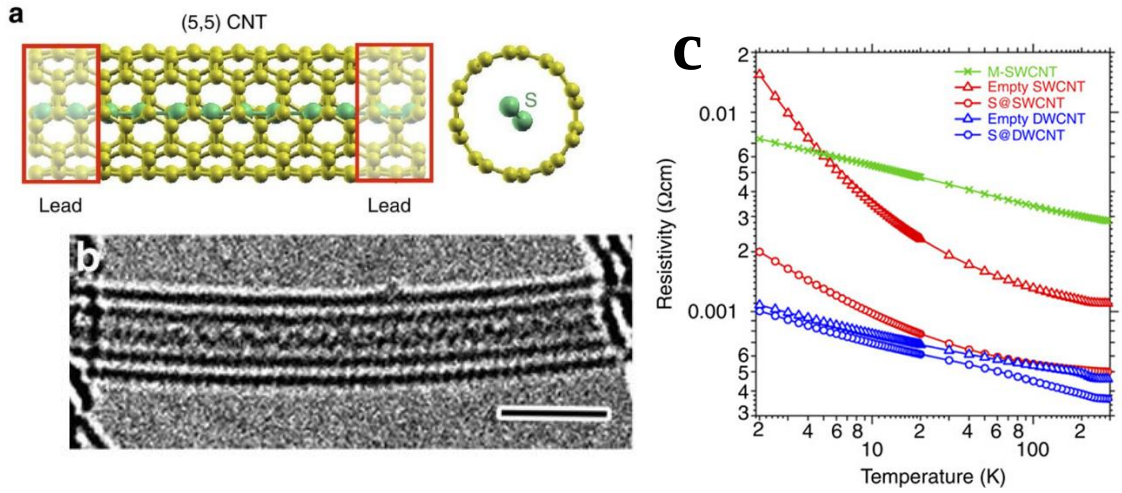

Figure 3.1: Electrical conductivity enhancement resulting from encapsulated SWCNTs. (**a**) Schematic of linear chain of sulfur within a (5,5) SWCNT (**b**) HRTEM image of a sulfur chain within a SWCNT (**c**) Electrical resistivity measurements for SWCNTs and DWCNTs before and after sulfur filling [80]

Recently, Fujimori et al. studied the electrical behavior of single linear atomic chains of sulfur. [80] This one-dimensional linear chain (Figure 3.1a) is predicted to show a finite density of states, which leads to metallic behavior (Figure 3.1c). The demonstration of these phases was previously only achieved through ultrahigh pressures and had not been experimentally confirmed. [81] [82] Through high resolution transmission electron microscopy (HRTEM), Fujimori et al. were able to demonstrate the presence of linear and zig-zag configurations of sulfur chains within a SWCNT (Figure 3.1b). The ability to stabilize these phases allows the unique opportunity to study sulfur using TEM with minimal sulfur loss due to sublimation. From an electrochemical standpoint, the ability to transform sulfur to a metallic state material would solve one, of the two, main issues lowering the performance of Li-S cells. Furthermore, the mechanical stability of the SWCNTs provides a structure capable of withstanding volumetric expansions. Similar to graphene, CNTs

potentially act as a diffusive barrier to the polysulfides formed during the cycling of the cell. Therefore, we aim to study the electrochemical performance of sulfur when confined to the interior of a SWCNT. We also examine the effects of the processing conditions on both the structure of the CNTs and the electrochemical performance.

3.2 Carbon Nanotubes

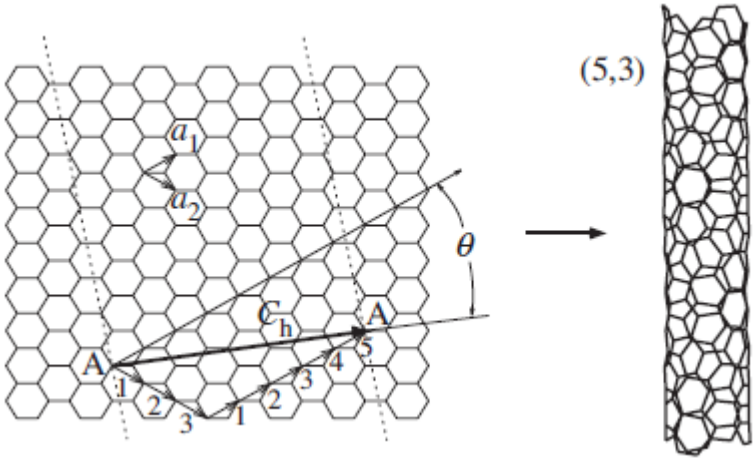

Figure 3.2: CNT structure formed by the rolling of graphene sheets. [49]

Carbon nanotubes (CNTs) can be described as graphene sheets rolled into a cylindrical form (Figure 3.2). As a result, they share many structural similarities and properties as their planar counterparts. However, due to their small radius of curvature, there are some characteristics which are unique to the CNT structure. CNTs can be largely classified by the number of walls that they possess. Either they are single-walled (SWCNT), or multi-walled (MWCNT). Similar to graphite, they possess an interplanar spacing of roughly 3.41nm [49]

The chirality of the CNTs dictates many of the CNTs properties, including its electrical behavior. [50] The chiral vector can also be used to determine the edge

structure which is either zigzag, or armchair. Zigzag CNTs have the (n,m) indices of (n,0), while armchair are (n,n). [49] In general, (n,n) tubes are metallic behaving, those with indices where n – m = 3j, where j is an integer not equal to zero are small band-gap semiconductors, and all other indices are wide band-gap semiconductors. [83] The small gap case (n – m = 3j) is one such instance in which the radius of curvature causes unique properties to CNTs. As you go to larger radii, you expect to see a decrease in the band-gap for large-gap semiconductors and a transition from the tiny-gap semiconductors to an almost metallic behaving state. These unique changes offer the ability to tailor the electrical properties based on the synthesis methods. Another defining characteristic of the electrical behavior of CNTs is the presence of defects in the system.

While considered to be a highly pristine material, the possibility of certain defects in CNTs is an unavoidable reality. The most common defect in carbon nanotubes is the terminating point of the CNTs. While it doesn't affect the majority of the properties of the seen over the length of the material, due to its high aspect ratio, interesting behavior can be seen in looking at the "cap". The most common form of defects at the cap of the CNTs is the presence of pentagon-heptagon (5/7) pairs. These pairs, which arise due to the curvature, allow for complete closure of the CNT. Due to their increased surface energy, they have been shown to be preferential sites for certain oxidation reactions which will be described in further detail later in this chapter.

In our specific works involving high-resolution TEM (HRTEM) imaging of SWCNTs, it is necessary to discuss defects that can be created during beam

irradiation. Beam-induced damages of SWCNTs have been well studied. Often, direct irradiation results in necking of the SWCNT, eventually leading to breaking of the SWCNT. [84] [85] It was shown that for energies greater than 120 keV, bonded carbon atoms can be displaced, via knock-on damage.[86] This atomic displacement results in the creation of vacancies that may be mended through the formation of the previously described pentagon-heptagon pairs. Other types of defects resulting from atom displacement are of higher surface energy, such as squares . [49] The Stone-Wales defect is a common type of surface reconstruction in which one of the C-C bonds is rotated. [87] This results in the lower energy atomic arrangement of the pentagon-septagon pair. However, there still remains an important part of the CNT structure -- the inner cavity.

3.3 Filling of CNTs

The interior of CNTs possess the ability to create a variety of new, exciting materials, which behave unlike any others. The first filling of CNTs was done using MWCNTs in 1993. [88] The study showed that it was possible to fill MWCNTs using heating in an oxygen environment to "uncap" the covered MWCNTs, followed by the subsequent heating in the presence of a liquid, or gas phase. Preliminary effects showed that, depending on the processing conditions, the yield of filled material was extremely low. They also saw damage to the structure of the MWCNTs in certain cases. Following these trials, scientists attempted to fill the MWCNTs in-situ, during the growth process. At the time, SWCNTs had not been discovered, but were eventually discovered through attempts to fill MWCNTs in-situ using cobalt metal. [89] This discovery spurred the interest in filling SWCNTs with materials in an effort

to use their nanocavities to demonstrate new nanoscale physics which do not apply in macroscale materials.

It took 5 years after the first isolation of SWCNTs to show evidence of direct filling. Similar to MWCNTs, initial efforts were aimed towards the creation of new nanowires with exotic properties directly related to their nanoconfinement. Given the smaller diameters of SWCNTs, it was expected that these materials would behave differently to those created in MWCNTs. One material which received a lot of attention as potential filler was the C_{60} molecule, which produced a material dubbed, Bucky peapods". Expected to be the next great material, a lot of the potential applications never came to fruition. However, the understanding created through the filling of this material, allowed for the production of many other exciting, hybrid structures.

The most common filling procedure of CNTs with C_{60} molecules consists of a two-step process: oxidation of the nanotubes followed by exposure to a gas vapor. The first step of thermal oxidation serves the primary purpose of uncapping, or opening holes in the CNT ends, or sidewalls. In addition, oxidation has shown further benefits such as the healing of defects in carbon nanotube sidewalls and removal of amorphous carbons and catalyst particles. [90] Different methods have been used to begin the process of opening SWCNTs prior to filling. They can be broken into two major categories: chemical oxidation and thermal oxidation.

3.4 Oxidation of CNTs

The first demonstration of gas phase opening of CNTs was published in 1993 by Ajayan et al. [91] In their experiments, they heated MWCNTs in air for varied times and temperatures. They found that at a temperature of 700 ˚C, they began to see substantial mass loss. At temperatures of 850 ˚C, their samples were completed oxidized within 15 minutes. In addition to the CNTs, they observed oxidation of C_{60} molecules, as well as other nanoparticles. After heating at 800 ˚C for 10 minutes, they were able to see open ends of MWCNTs using TEM. They estimated roughly 20% of the MWCNTs showed signs of open ends. It has also been shown that the structure and electronic properties of CNTs, can be changed at room temperature in air. [92] This rate of change, or other effects of oxidation, strongly depends on the structure of the carbon species.

The general process of oxidation results in the formation of CO_2, as well as carboxyl groups (COOH) bonding to the CNT structure. To estimate the adsorption energy, modeling has been done to understand the energetics associated with oxidation at different types of sites of CNTs. [93] Differences similar to these could potentially affect the oxidation behavior for the different temperatures that we observed.

The total energy of adsorption of an O_2 molecule can be defined as:

$$E_{ad} = E_{tot}(O_2 + CNT) - E_{tot}(O_2) - E_{tot}(CNT) \quad \textbf{(Eq. 3.2)}$$

Where E_{tot} is the total energy of the system and $E_{tot}(O_2)$ is the total energy of the O_2 molecule. The results of their simulations can be seen in Figure 3.3, which demonstrates the O_2 adsorption process for both armchair and zigzag edge CNTs. [94] The process for reaching this site, varies between cases. For armchair CNTs,

there are several steps which lead to the final position of the oxygen atoms as shown in Figure 3.3a-d. The initial is a bonding to the C_2 dimer of the armchair edge, resulting in a slightly larger bond distance between oxygen molecules resulting from columbic repulsion (Figure 3.3a). The E_{ad} of this configuration was calculated to be -4.04 (-4.61:-38.2) eV. The relaxation of this bond results in the breaking of the oxygen molecule into two separate oxygen atoms (Figure 3.3b). Following this step, the E_{ad} is -7.41 (-7.81: -6.89) eV, increasing due to the increased charge transfer. A more stable configuration is obtained by separating O_2 molecules resulting in an E_{ad} of -7.98 (-8.13: -7.04) eV (Figure 3.3c) when the one of the O atoms replaces a C atom at the pentagonal site. An additional stable site can be seen in Figure (Figure 3.3d) has -5.26 eV. For zigzag edges, there exists only one top site which possesses an E_{ad} -8.39 eV (Figure 3.3e) . This is in agreement with calculations showing the higher energies of zigzag edged CNTs. [95]

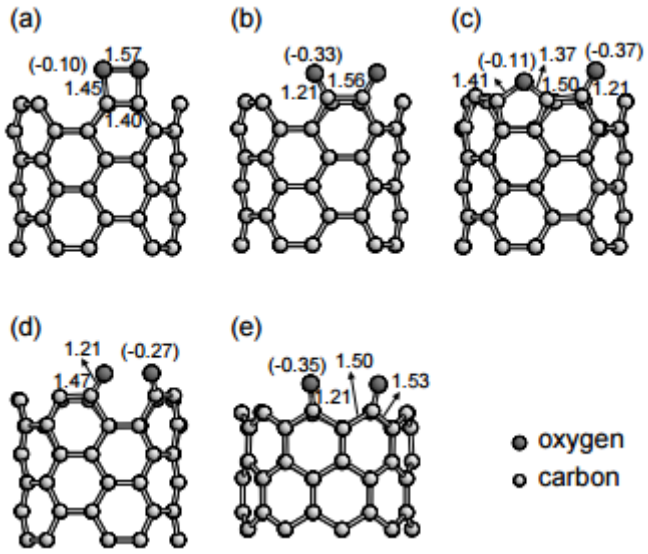

Figure 3.3: Adsorption of an O_2 molecule on CNT edges. (**a**),(**b**) the intermediate states on the top site of the armchair edge, (**c**) the final state with oxygen atoms located at pentagon and top sites of the armchair edge, (**d**) the seat site of the armchair edge, and (**e**) the top sites at the zigzag edge. The dark and grey balls indicate the oxygen and carbon atoms, respectively. All bond lengths are in units of Å. The Mulliken excess charges of the oxygen atoms are shown in parentheses in units of electron. [96]

Quantification of the etching process following adsorption was done by calculating the energy barriers for C-O desorption. Desorption processes for different configurations can be seen in Figure 3.4a and 3.4b. The corresponding energy of adsorption as a function of distance from the adsorbed oxygen atom can be seen in Figure 3.4c. Starting at the oxygen adsorption position seen in Figure 3.4a, which has the oxygen in the pentagon site, the weak C-O bond is broken. Following the breaking of that bond, the C-O bond can be removed, resulting in the oxygen atom taking the top site above the C-pentagon. This process has a barrier height of 2.48 eV. The desorption process of the zigzag top site results in a desorption energy of 2.44 eV, followed by the formation of a C-pentagon. In comparison to the O_2 *adsorption*

values, the O_2 *desorption* values are much more similar. This suggests that the selective etching of one edge type would present itself as a challenge.

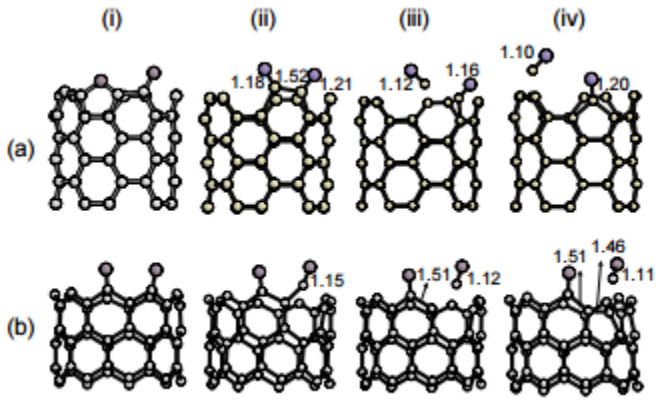

Figure 3.4: Desorption pathways of the C-O pairs. Desorption from (**a**) the pentagon site at the armchair edge, (**b**) the top site at the zigzag edge [96]

Chemical, or acid-based oxidation, is a common method of purifying CNTs. It has been shown that acid-based purification procedures can involuntarily introduce open ends. [97] As the chemistries of each of these processes depend on the chemical being used, complete details of the various chemical oxidation processes will not be presented in this work. A review on the chemical oxidation on multiwalled carbon nanotubes was given by Datsyuk et al., and it is a good point of reference for these processes. [98]

Most commonly, it is assumed that the oxidation process begins at the caps of the CNTs, due to the instability associated with the local curvature. There also exists the process of opening and subsequent filling, which may occur along the sidewalls of the CNTs. The unzipping of CNTs has been demonstrated to create graphene nanoribbons [99] The technique uses a chemical oxidation process in which the

MWCNTs are suspended in sulfuric acid, then treated with $KMnO_4$ for 1 hour at room temperature. Following this treatment, they are treated in $KMnO_4$ at 55-70 ˚C. The originating point of the unzipping is not known, the cut, are generally longitudinal resulting in the straight graphene nanoribbons (Figure 3.5) This demonstrates an alternate form of filling in comparison to the most commonly reported methods. It would be expected that the larger opening area would allow for a higher yield of filled material. It still remains to be seen the exact method of filling, but this process demonstrates the unique ability to open the CNTs. Here, we study the effect of thermal oxidation on the performance of CNT-sulfur cathode materials which have been created using a high temperature sulfur filling process.

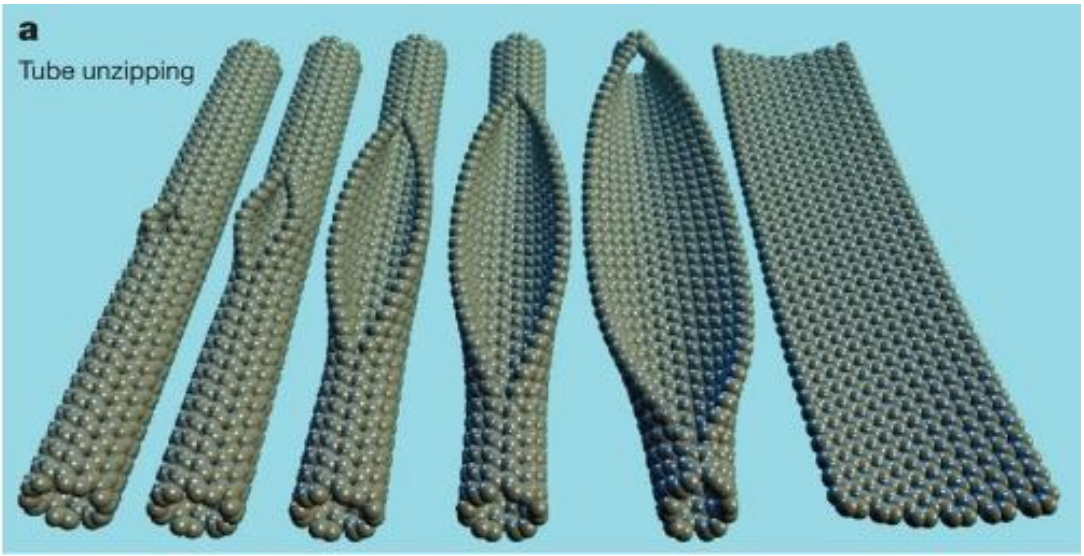

Figure 3.5: Unzipping of a CNT. Representation of the gradual unzipping of one wall of a carbon nanotube to form a nanoribbon. Oxygenated sites are not shown. [99]

3.5 Sulfur Filling of CNTs

The filling of sulfur into carbon nanotubes is done through high temperature filling. Following thermal oxidation, the SWCNTs are loaded into glass tubes after thorough mechanical mixing with sulfur using a weight ratio of 10:1 for sulfur to carbon, respectively. The glass tubes are then connected to a vacuum pump. Following evacuation of the glass tubes, they were sealed using an oxygen-propane torch. The sealed glass tubes were then loaded into a vacuum furnace where they are heated at 600 ˚C for 48 hours. Figure 3.6 shows the structural evolution of sulfur during heating. At room temperature, sulfur exists primarily as orthorhombic (α) sulfur. This crystal structure consisting of cyclic S_8 molecules arranged in an orthorhombic crystal structure. Above temperatures of 95 ˚C, sulfur transitions to a metastable state of monoclinic (β) sulfur. At 119 ˚C, the intermolecular bonds of the S_8 molecules are broken, resulting in mobile S_8 molecules which still maintain their crown-like structure. Upon further heating, the cyclic rings of the S_8 molecules are broken, resulting in linear S_8 chains. Above ~445 ˚C, these longer S_8 molecules break to form different chain lengths ranging from S_2-S_6. Therefore, at the 600 °C soak temperature, we expect that the majority of the sulfur molecules are highly mobile S_2 molecules. These molecules should have the highest probability of diffusing into the interior of the CNTs.

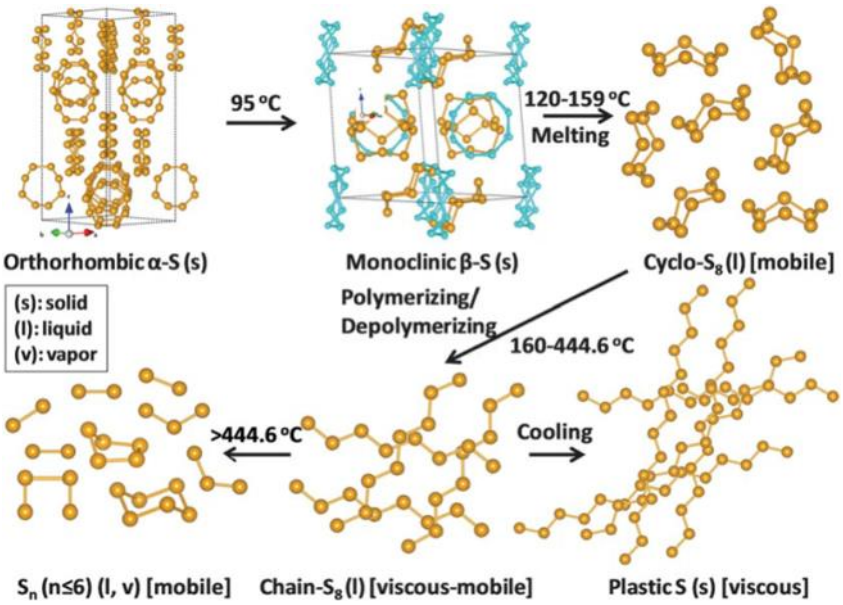

Figure 3.6: Phase transitions of sulfur during heating [100]

Studies on the electrochemical behavior of shorter sulfur molecules have been conducted. By using a higher temperature filling procedure, shorter sulfur molecules were produced. This results in lower order polysulfides using a microporous carbon. [101] The confinement of these lower order polysulfides, which are insoluble in the electrolyte, leads to increased capacity retention. A reasonable hypothesis would predict similar results in our studies.

3.6 Results and Discussion

3.6.1 High-resolution TEM Characterization of Composite Materials

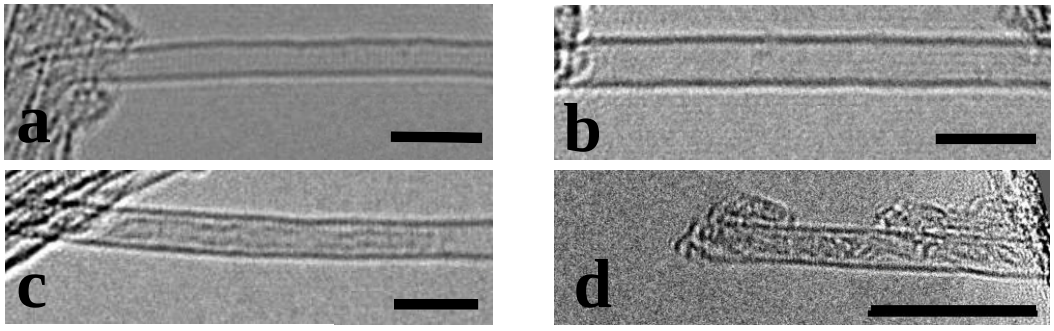

Figure 3.7: TEM Images of SWCNT/S composites produced through high temperature filling and varying temperatures of thermal oxidation. (**a**) SWCNT/Sulfur composites without any prior thermal oxidation. (**b**) SWCNT/Sulfur composites oxidized at 375C in air for 1 hr. (**c**) SWCNT/Sulfur composites oxidized at 475C in air for 1 hr. (**d**) SWCNT/Sulfur composites oxidized at 575C in air for 1 hr.

High-resolution transmission electron microscopy (HRTEM) is used to characterize the carbon nanotubes following sulfur filling. The instability of sulfur within a TEM has already been discussed, but it should be noted that SWCNTs also damage very quickly during HRTEM imaging conditions. To minimize beam damage to the SWCNTs, the focusing and alignment of the beam was done in areas outside of the region of interest. Figure 3.7 shows TEM micrographs of SWCNT/S composites for different oxidation temperatures. Unoxidized SWCNTs were used as a control to test whether the thermal oxidation step was necessary to show evidence of sulfur infiltration. Figure 3.7a shows a representative image of a SWCNT that had not been

oxidized prior to high temperature filling with sulfur. There were no filled SWCNTs in our samples comprising unoxidized SWCNTs. This result supports the expectation that the initial step of thermal oxidation is necessary to create entry points for sulfur diffusion. Figure 3.7b shows a SWCNT nanotube that was oxidized at 375 °C. Similar to the unoxidized sample, the majority of the nanotubes which were imaged did not contain sulfur. We did find some SWCNTs that contained filled materials, but the majority of the SWCNTs were unfilled. At 475 °C, visual proof of sulfur within the SWCNT can be readily seen (Figure 3.7c). Two chains are present within the SWCNT confirming successful filling of our nanotubes. Over all of our 475 °C samples, all well-resolved SWCNTs showed signs of sulfur filling. The specific amount of sulfur loading for our SWCNTs oxidized at different temperatures could not be determined using TEM due to the fact that the SWCNTs were heavily bundled when deposited onto holey carbon grids. The sample oxidized at 575 °C demonstrates SWCNTs that are filled with sulfur chains, as well. However, there is also a noticeably higher amount of amorphous carbon present in the sample (Figure 3.7d). As the temperature of oxidation is increased, the amorphous carbons around 375 ˚C oxidize. Based on our TGA results, our SWCNTs break down and are heavily oxidized beginning at temperatures of 550 ˚C. We see substantial carbon mass loss following the mass loss associated with sulfur evaporation. In addition to our composite materials, this trend can also be seen in Figure 3.8d, which shows TGA data for pristine SWCNT material.

Based on our TEM analysis, the optimal oxidation temperature for filling is 475 ˚C. At this temperature, there exists minimal formation of amorphous carbons,

while allowing for the successful filling of the inner cavities. At 375 ˚C, the demonstration of successful filling could be a result of certain inherent defects with lower activation energies. It is also possible that the presence of amorphous carbon, which is completely oxidized following treatment at 475 ˚C, blocks entry points for sulfur. This would result in both a lower yield and a lower ratio of SWCNTs to carbonaceous materials, which would degrade the electrochemical performance.

3.6.2 Raman Spectroscopy Analysis of Composite Materials

Further evidence of the sulfur filling can be investigated using Raman spectroscopy. Raman spectroscopy is a widely used technique to probe the characteristics of carbon nanotubes including their phonon, electrical, and defect structures. Raman spectroscopy results from the excitation of an electron from the valence energy band to the conduction band. This excitation is caused by incident photons, typically a laser. The energy of the scattered electron is either absorbed, or released, by phonons. Then the electron relaxes back to the valence band, from the conduction band, resulting in the release of a photon. The energy of the emitted photon is then plotted as the frequency shift, or change of energy resulting from the absorbed or released energy of the phonons. [102] The analysis of these energies allows for the understanding of many complex processes inherent to the material.

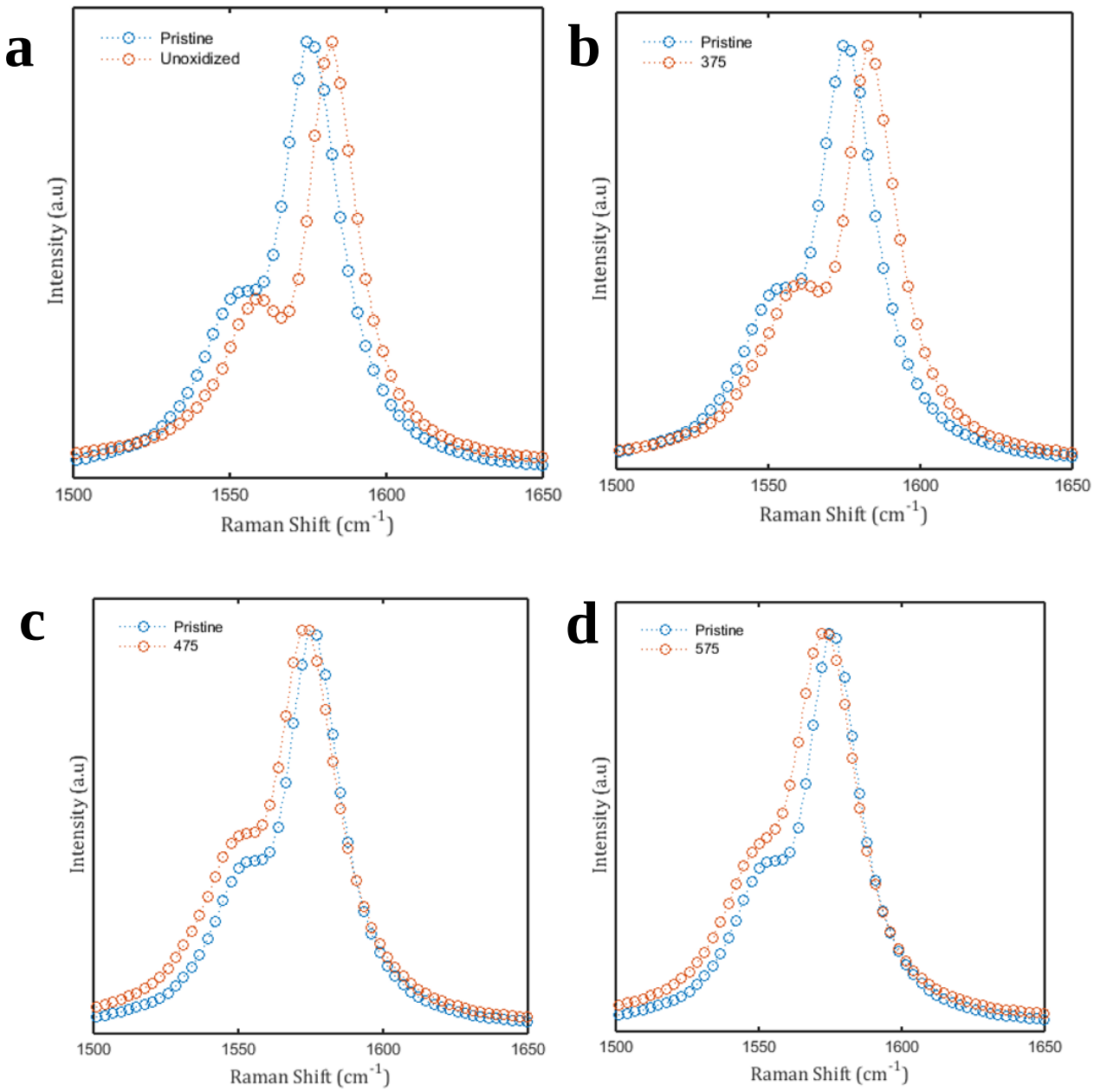

Figure 3.8: Raman spectroscopy of SWCNT/S composites showing G-peak. (**a**) SWCNT/sulfur composites without any prior thermal oxidation. (**b**) SWCNT/sulfur composites oxidized at 375 °C in air for 1 hr. (**c**) SWCNT/Sulfur composites oxidized at 475 °C in air for 1 hr. (**d**) SWCNT/Sulfur composites oxidized at 575 °C in air for 1 hr.

The features of the Raman spectra of CNTs vary slightly from other graphite structures. The three peaks discussed during the analysis of graphene using Raman spectroscopy remain (D, G, and 2D, or G' peaks). An additional feature known as the radial breathing mode (RBM), is also present. This feature results from additional vibrational modes in the radial direction as the CNT expands, and contracts. [102] The Breit-Wigner-Fano (BWF) line can be used to probe the metallicity of SWCNTs. [103] The asymmetric line shape can be described by the equation:

$$I(\omega) = I_0 \frac{[1+(\omega-\omega_{BWF})/q\gamma]^2}{1+[(\omega-\omega_{WBF})/\gamma]^2} \textbf{ (Eq. 3.3)}$$

Where 1/q is the phonon-continuum of states interaction and ω_{BWF} is the frequency the BWF peak at the maximum intensity I_0. Using this equation, it is possible to deconstruct the Raman spectra to obtain more information on the line shape of the spectra. [104] The resulting Raman spectroscopy curves for the different oxidations temperatures can be seen in Figure 3.8. Analysis of the G-peaks of the sulfur-processed SWCNTs compared to the pristine samples show similar trends to those seen using HRTEM imaging. The pristine SWCNTs show metallic behavior. The same pristine SWCNT sample was used for comparison. The unoxidized and 375 ˚C samples show similar semiconducting behavior after sulfur processing.

The D-peak is used as a measure of the disorder of the material being studied. However, due to changes in the intensities of the signal, variation between samples and runs can occur. Therefore, it is more beneficial to look at the ratio between the G- and D-peaks to allow for consistent comparison. The general trend is a decrease in the ratio as a function of increasing temperature. The G/D ratios are 0.0699, 0.0587, 0.0511, and 0.0382 for the unoxidized, 375 ˚C, 475 ˚C, and 575 ˚C samples

respectively. Given the higher stability of the SWCNTs, it is expected that they would be the last material to oxidize completely. Therefore the D-peak would be expected to lessen significantly in the absence of amorphous carbons, disordered graphitic carbons, and other disordered byproducts of the synthesis process.

3.6.3 Thermogravimetric Analysis of Composite Materials

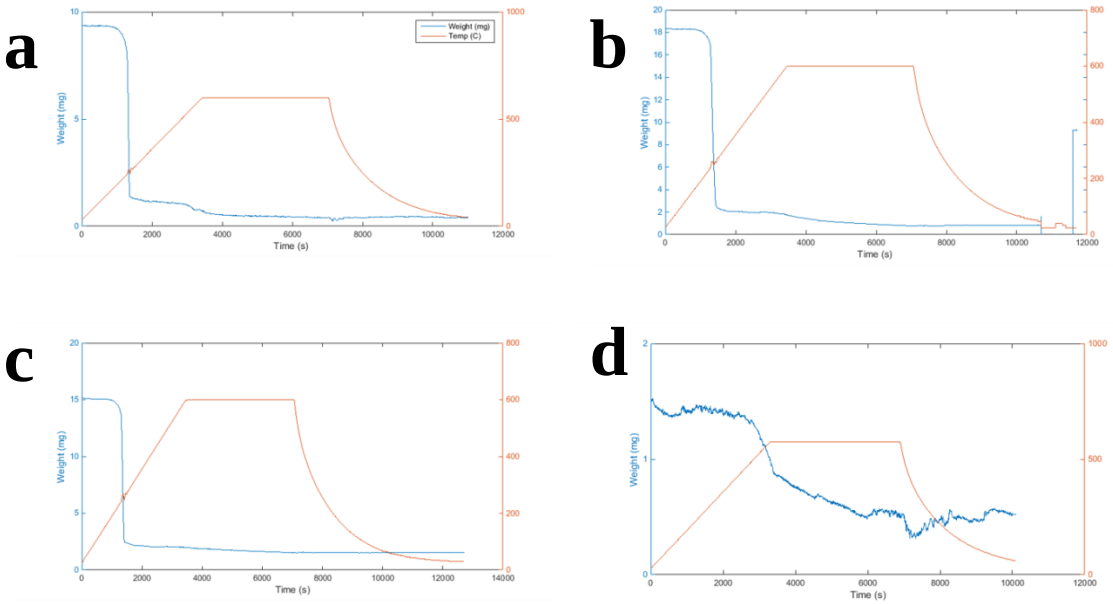

Figure 3.9: Thermogravimetric analysis of SWCNT/S composites produced through high temperature filling and varying temperatures of thermal oxidation. (**a**) SWCNT/Sulfur composites without any prior thermal oxidation. (**b**) SWCNT/Sulfur composites oxidized at 375 ˚C in air for 1 hr. (**c**) SWCNT/Sulfur composites oxidized at 475 ˚C in air for 1 hr. (**d**) SWCNT/Sulfur composites oxidized at 575 ˚C in air for 1 hr.

Figure 3.9 shows thermogravimetric analysis of our CNT/S composite structures. The blue curve is the weight of the sample during heating. The orange curve is the temperature. Both are plotted as a function of time. Small oscillations on the curve can be seen in the orange curve, which correspond to oscillations in the thermocouple

resulting from the condensation of sulfur. Thermogravimetric analysis (TGA) serves as a well-established tool to characterize the purity of SWCNTs. Typically, there are two distinct weight loss temperatures, which correspond to amorphous carbon, or catalyst particles, and pure SWCNTs. [105] The curves for the different oxidation temperatures show similar behavior, with the majority of the mass loss occurring at 250 °C. Roughly 85% of mass is lost during this range. This suggests a relative weight ratio of 85% sulfur and 15% SWCNTs. Also visible is an additional weight loss period at 550 °C which corresponds to the burning of SWCNTs. This result is also seen in TGA analysis of pristine carbon nanotubes

The differentiation between sulfur species that are encapsulated within the interior of CNTs and sulfur species on the external surfaces relies on the understanding of the sublimation behavior of encapsulated sulfur. This understanding does not currently exist. It is possible that the evaporation of external sulfur and internal sulfur occurs at the same temperature which means the large mass loss seen at 250 °C is from both locations of sulfur. It is also possible that the sulfur evaporation occurs at the damage temperature of the CNTs, which is around 550 °C. Therefore, it is hard to differentiate the location of the sulfur using TGA. The behavior beyond the evaporation temperature is also slightly different for the unoxidized and 375 °C samples, as well. There is a clear plateau prior to reaching the holding temperature of 600 °C. This plateau is not as prominent in the 475 °C sample. This could be the burning of additional amorphous carbon, or nanoparticles which were not removed during the oxidation process.

3.6.4 Electrochemical Performance of Sulfur-filled SWCNTs

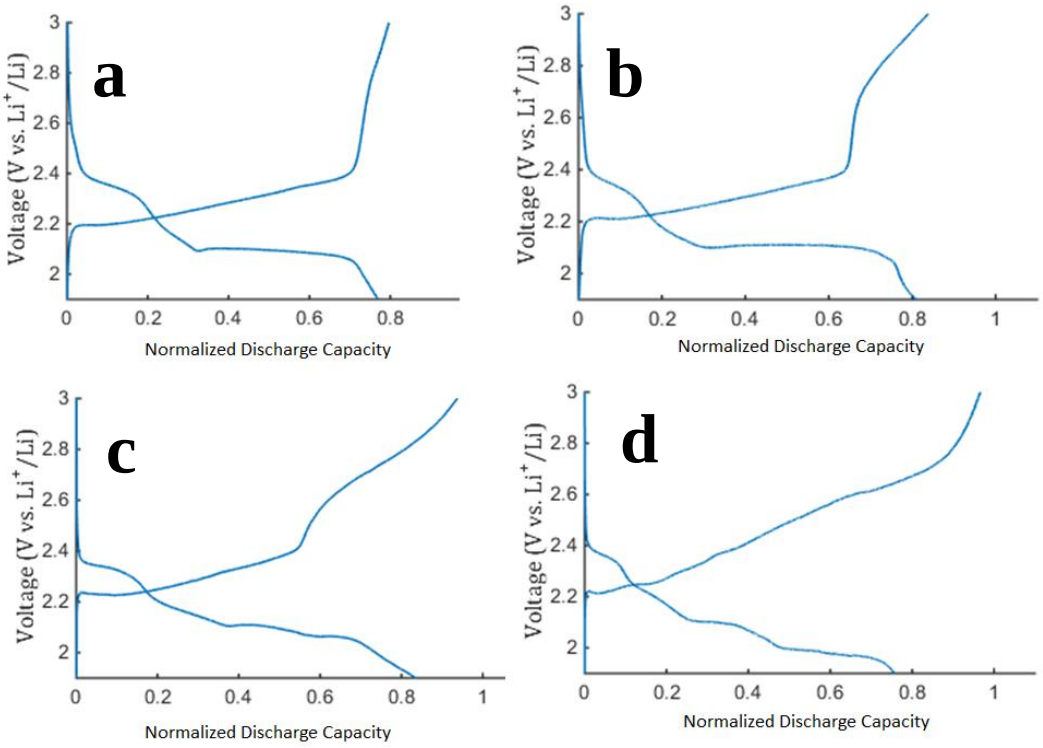

Figure 3.10: Electrochemical data for varying oxidation temperatures. (**a**) SWCNT/Sulfur composites without any prior thermal oxidation. (**b)** SWCNT/Sulfur composites oxidized at 375 ˚C in air for 1 hr. (**c**) SWCNT/Sulfur composites oxidized at 475 ˚C in air for 1 hr. (**d**) SWCNT/Sulfur composites oxidized at 575 ˚C in air for 1 hr.

Our electrochemical testing shows a clear dependence on the cell's performance with the thermal oxidation temperature. Looking at the plot of capacity as a function of voltage, distinct features can be seen between samples. The unoxidized sample shows the traditional plateaus associated with Li-S batteries. There is a plateau at 2.3V corresponding to the production of higher order polysulfides ($8 < Li_2S_x < 4$). At 2.1 V, there is the lower order plateau, which results in the final discharge products of Li_2S_2 and Li_2S. We observe the same line shapes for the 375 °C cell. Based on these line profiles, it can be assumed that the majority of the sulfur participating in cycling

is on the outer surfaces of the SWCNTs. On the 475 °C sample, we begin to see additional features on the discharge curve. An additional plateau at a lower voltage appears, which we attribute to the presence of encapsulated sulfur. Again, at 575 °C, an additional plateau is observed at lower voltages. At 575 °C, this feature is the most prominent. The profiles of the discharge curves support our TEM observations which show the presence of encapsulated sulfur for temperatures at, or above, 475 °C.

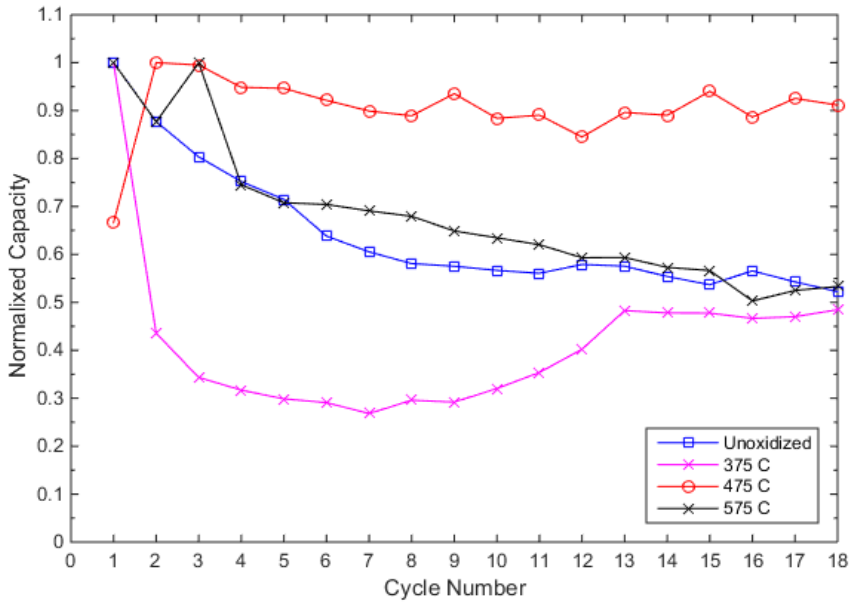

Figure 3.11: Normalized discharge capacities. Discharge capacities which were normalized to the maximum discharge capacity of the cell.

Figure 3.11 shows the normalized discharge capacity relative to the highest discharge capacity for each cell. SWCNTs that have not been oxidized show the typical capacity loss within the first few cycles associated with the polysulfide shuttle. The same trend can be seen for the SWCNTs that have been oxidized at 375 °C. At the oxidation temperature of 475 °C, we see much more stable cycling behavior. We suspect that at this temperature, the oxidation temperature is high

enough to create preferential SWNT sites for sulfur infiltration. At temperatures below 475 °C, there may be sulfur infiltration, but this early-stage process begins primarily at large defect sites which serve both as sites of sulfur access, as well as removal. At 575 °C, we see evidence of sulfur filling, but again see the typical capacity losses associated with the shuttle mechanism. Therefore, we conclude that at these temperatures, the structure of the SWCNT has been highly damaged resulting again in sites at which sulfur can both enter and exit.

3.6.5 Summary

By varying the oxidation temperature used during the opening portion of our sulfur filing process, we have made a direct correlation between the structure and the resulting electrochemical performance of the cell. We suspect that certain defect sites are preferentially oxidized at 475 ˚C, allowing for the introduction of sulfur during filling. Based on our stable electrochemical performance, these sites do not allow for the dissolution of lithium sulfides during electrochemical cycling. The other temperatures are less optimal in that they are either below the energy threshold for oxidizing these preferential sites, or they far exceed these thresholds that result in irreversible changes to our sample. Both of these cases allow for the capacity loss associated with the polysulfide shuttle. Thus, 475 °C appears to be the optimal temperature for oxidation of SWCNTs to form sulfur-filled Li-S battery cathodes.

Further work on the understanding of these structural changes should include the modeling of thermal oxidation in air using a graphene sheet as a model system. Similar work has been done on studying defects of graphene oxide. [106] The

evolution of the structure can be seen in Figure 3.8 during annealing. It clearly shows the creation of holes which allow for both the filling and removal of material within the CNTs inner cavities. We aim to model similar structures to determine what sizes of species are able to enter and exit our SWCNTs and the processes which can produce these species.

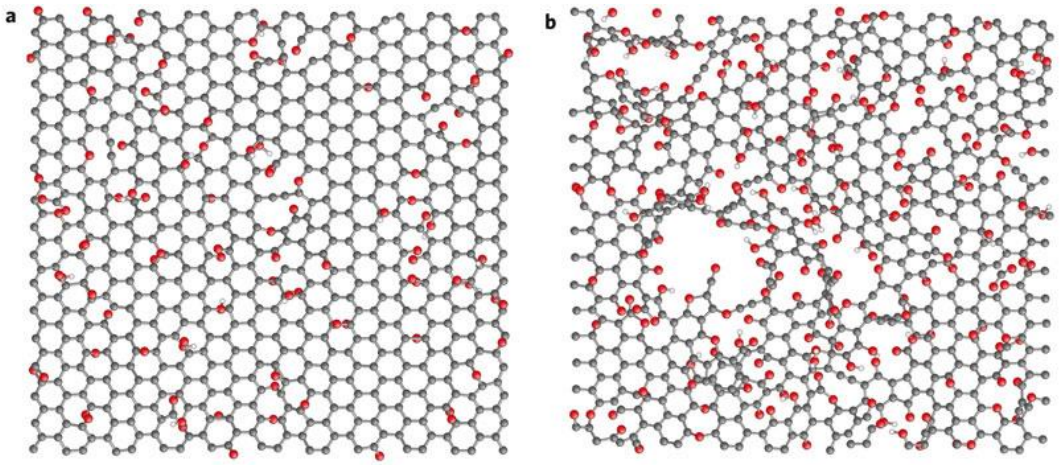

Figure 3.12: Morphology of rGO and the structure of defects formed during thermal annealing. (**a,b**), Morphology of rGO sheets with an initial oxygen concentration of 20% (**a**) and 33% (**b**) in the form of hydroxyl and epoxy groups in the ratio 3/2 after annealing at 1,500 K [106]

Chapter 4 In-Situ Transmission Electron Microscopy Studies of MWCNT/S Composites

4.1 Motivation

In-situ experiments provide valuable information on the species formed during cycling. In-situ transmission electron microscopy is a valuable tool capable of providing information on the structural, chemical, and morphological changes which occur in a wide range of dynamic systems. For Li-S batteries, significant gaps still remain in the understanding of the behavior of lithium and reduced sulfur species at the carbon-sulfur interface during working battery conditions. The previously described techniques do not offer the ability to monitor the reactions in real time and often rely on ex-situ evaluation of the materials structure. TEM offers the ability to achieve these requirements, yet very few studies have been completed on Li-S electrochemistry due in party to instability of sulfur under vacuum. [107] Successful employment of in-situ TEM studies on the interfaces between carbon and sulfur would give deeper insights into fundamental electrochemical reaction mechanisms and kinetics in the Li-S/carbon systems.

It should be noted that a large portion of this chapter's work is still ongoing. In this chapter, we will outline the motivation for our experiment as well as the current status and results. We are still developing conclusions based on the results that we have obtained.

4.2 Experimental Set up and Techniques

For TEM characterization, two TEM holders were used. The first holder (Figure 6.a) is a standard JEOL 2100 single-tilt holder. This holder was primarily used for the analytical techniques including EELS, EDS, and STEM studies. The samples were mounted on a holey carbon grid and used as a baseline for the solid electrolyte studies. The majority of the work included in this chapter utilized second customized Nanofactory nano-manipulation holder (as seen in Figure 4.1). The main components of the Nanofactory holder are the holder rod, end piece, and the front piece. The end-piece houses the electronics as well as the piezo connector and signal connector. The holder rod contains wires which run through it to the front piece, where the experiment occurs. The front-piece, contains both the sample stub and the nano-manipulation tip (Figure 4.1c).

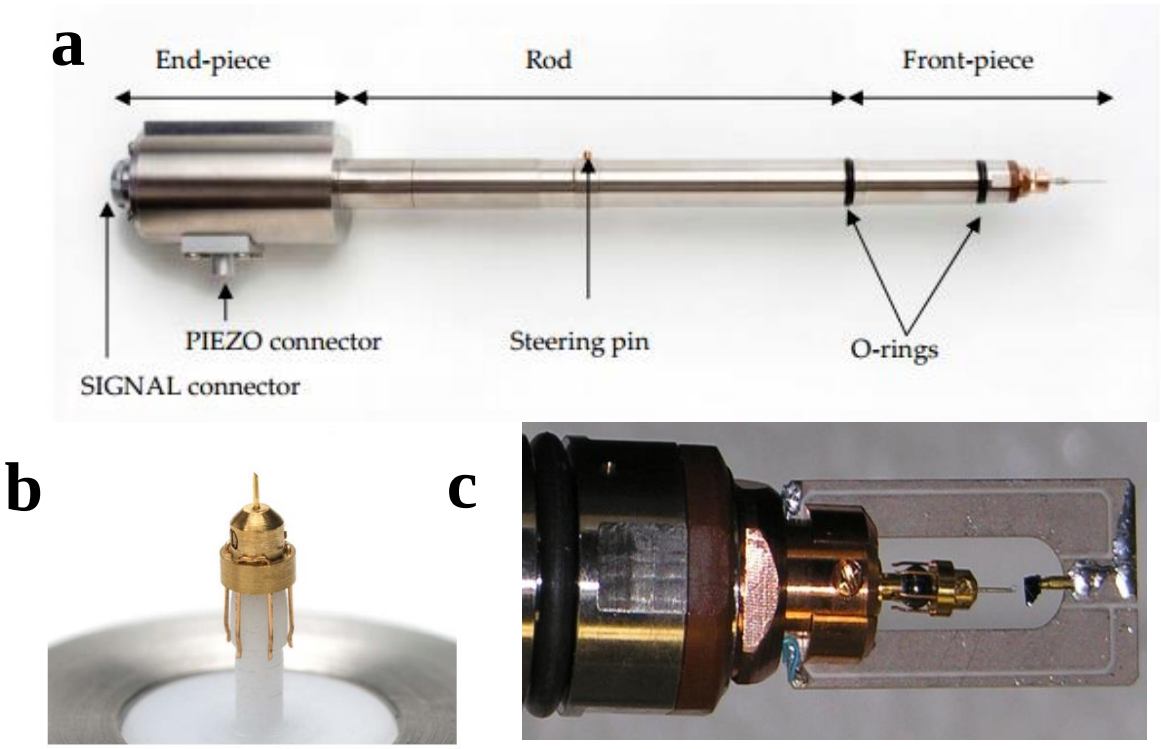

Figure 4.1: Nanofactory Holder used for our in-situ TEM experiments. (**a**) TEM Holder (**b**) Nanofactory tip-hat which serves as the anode during in-situ experiments (**c**) Sample configuration with sample mounted opposite to tip-hat.

The CNT sample is mounted to a brass stub using a conductive epoxy was blended from Epo-tek 593 ND and silver flake purchased from Alfa-Aesar (90% < 20 micron, 99.9% (metals basis), by mass). It was found that a ratio of 5:1:12 (Part A: Part B: Silver Flake) produced a conductive epoxy with resistances ranging from 2-10Ω. A small amount of silver epoxy was painted onto the surface of the brass stub. The CNTs studied are then affixed to the brass stub. The epoxy is cured at 130°C for 20 minutes.

To ensure that the height of the sample is within the viewable height ranges of the microscope, the sample is mounted without the anode prior to the anaerobic loading process within a glove bag as described below. In addition to the limitations

of the height, samples are often inhomogeneous. Therefore, it can take multiple attempts to mount the sample in a way which allows for the viewing of a favorable area, containing MWCNTs visibly protruding from portions of the sample. In addition, the inhomogeneity of the sulfur incorporation procedure creates sulfur-rich areas as well as regions which are primarily CNTs. The differences between the reaction kinetics and experimental results will be presented later in this chapter.

To conduct in-situ TEM studies on lithium-sulfur batteries, the first issue to be addressed is the air sensitivity of lithium. As previously stated, lithium metal is the primary anode used in lithium-sulfur batteries. Lithium-oxide can readily be formed in air to produce Li_2O, under the following reaction.

$$4Li + O_2 \rightarrow 2Li_2O \quad \textbf{(Eq. 6.1)}$$

To allow for the study of air sensitive devices in the TEM, a procedure was developed previously by Dr. Khim Kharki to allow for the safe insertion of the TEM holder into the microscope, with minimal air exposure. A glove bag (GlasCol S Model) was used to create an inert environment for sample handling and loading. The working end of the bag is sealed around the TEM goniometer and taped shut to create a quasi-hermetic seal. The glove bag is filled with argon, followed by purging three times, prior to the exposure of any air-sensitive materials to the environment. During loading, the sample was exposed to air for only a few seconds, at most, during the transfer of the holder into the column.

The nano-manipulation tip is mounted on a sapphire ball which is affixed to a piezo tube. The tip-hat is attached to the ball using Be-Cu “legs” which clasp onto the sapphire ball. The tip-hat holds an electrochemically etched, .25 mm diameter STM-

tip. This tip is typically made of Pt (Agilent N9801A). To complete the nano-battery, the anode (or anode & solid electrolyte) is scraped onto the STM tip within the glove bag. Typically, a lithium anode is used to replicate the battery components of commonly used Li-S batteries. Lithium metal foils are transferred to vials within a glove box, sealed with electrical tape, and placed into a container which is sealed with electrical tape, as well. Following transfer of the sealed container to the argon-filled glove bag, a piece of Li metal is removed from the vial, and inspected for any signs of oxidation due to oxygen or water vapor in the glove bag. If no signs of oxidation are present, then the Li metal is scraped onto the STM tip, and the tip-hat is secured to the sapphire ball.

For studies using a solid electrolyte, powders of Li_2S and P_2S_5 are mixed together in a vial within a glove box. Approximate ratios of 1:1 by volume are used for the mixture. The individual vials are sealed and placed within a larger sealed jar. To create the anode/electrolyte interface, lithium metal is scraped onto the STM tip as previously described. The, then lithium-covered STM tip, is scraped within the solid electrolyte powder of Li_2S and P_2S_5 to serve as the solid electrolyte.

The transfer of the TEM holder to the TEM column, results in the unavoidable exposure of the sample to air. The resulting lithium-oxide layer was used as a solid electrolyte for our *in-situ* studies. Several factors can influence the general morphology of the anode. The largest factor is the amount of time the holder is exposed to air, or any other non-inert environment. Therefore, fresh foils of lithium are used during every test. The amount of time the lithium foils remain in the jar was also minimized by limiting the time between removal of the lithium from the

glovebox and use for in-situ studies. In addition, the top layer of the lithium metal was scraped away using tweezers prior to the deposition of the lithium onto the STM tip.

Briefly, we found that the best way to make contact with individual nanotubes was, as follows. The sample was mounted at a correct height, capable of imaging at high magnifications. Ideally, there would be a high density of CNTs visibly separated from the bulk material. Following the confirmation of the height, the Nanofactory holder was placed within the glove bag. When positioning the tip-hat, the STM was placed near the area previously imaged. It was also placed slightly above the sample. Generally, as you move forward in any direction, the tip-hat tends to fall downward due to gravity. So by having the tip-hat positioned slightly higher than the sample, when approaching the sample in the forward direction, the tip-hat naturally would fall downward to the height of the sample.

In the case that the tip-hat was not in the correct position, or we chose to move to a different area of the sample, the tip-hat was moved away a considerable distance from the sample, in the y-direction. The sample was then brought back into focus using the WOBBX. The beam was repositioned for imaging on the STM tip, where the WOBB X was reactivated. The z-height was then adjusted (on max amplitude) to minimize wobbling. Once the image distortion subsided, the STM tip was moved forward in the y-direction until contact was made. We aimed to be close to the height prior to stepping forward because movement in the –Y-direction can be limited beyond a certain point. At large distances away from the sapphire ball, the legs

become more and more weak, causing their movements to become less predictable, or mechanically achievable.

4.3 Liquid vs. Solid State

In recent years, significant research effort has focused on the development of novel cathode materials capable of retaining the higher order polysulfides that dissolve in the electrolyte during the discharge process. This parasitic shuttle reaction has also prompted research efforts to focus on the development of a liquid electrolyte capable of suppressing this process. In general, liquid electrolytes offer the advantages of creating a larger electrochemical interface due to their ability to penetrate porous electrode materials. This increased contact area provides better reaction kinetics and overall battery components. In addition, due its undefined shape, it is capable of withstanding the volumetric changes associated with lithiation and delithiation . However, liquids tend to offer inferior chemical and thermal stabilities when compared to their solid counterparts. [107] Liquid electrolytes are often also electronic conductors, thereby decreasing the overall efficiency of the electrochemical cell. [108] Another common degradation mechanism in electrochemical cells which utilize a liquid electrolyte is the unavoidable formation of the solid electrolyte interphase (SEI). [109] The SEI formation occurs during the first cycle, coating the electrode material resulting in an overall loss of active material, as well as decreased battery performance.

In contrast, solid-state configurations excel in these weaknesses of liquid electrolytes, but falter in other places. Perhaps most importantly in the case of Li-S

batteries, solid electrolytes provide superior chemical stability. [110] However, due to their solid structure, they are not able to infiltrate porous materials often used in Li-S batteries. Therefore, the contact area between the electrolyte and electrode material is greatly reduced. In addition to poor wetting, solid electrolytes may develop cracks during cycling, resulting from their rigid shape. Until recent years, solid electrolytes were limited by their poor Li ion conductivity. [111] Along the same vein, solid electrolytes are expected to better protection from the formation of lithium dendrites during cycling. This problem can result in an electrical short, should the dendrite penetrate the separator and contact the cathode material. The dendritic formation can be further exacerbated through the formation of Li_2S on the anode surface.

Here, we have elected to study an all-solid state system. We expect that the enhanced reaction kinetics will allow for a more suitable system of study. In addition, due to the inability to study most liquid electrolytes in the TEM, making a direct connection between commonly used electrolytes and in-situ results presents a challenge. To study the most common liquids in a TEM, a special sealed liquid cell holder is required. While these holders have demonstrated an ability to effectively study these systems, they are often limited by the compatible electrolytes and geometric configurations. Limitations on the thickness or volume of liquid present in the sample create a challenge when trying to incorporate commonly used electrode materials. [112] As a result, this creates an additional correlation of the conclusions of the in-situ work to the reaction kinetics in a complete, working electrochemical cell. Also, secondary interactions of the liquid and the electron beam have been demonstrated [113] and prompted the creation of an entire subset for in-situ TEM

studies. Recent developments for in-situ transmission electron microscopy have enabled the study of electrochemical processes in-situ in the TEM. [114] However, due to its new development, the determination of appropriate systems of study is still ongoing.

4.4 Solid Electrolyte Selection

Selection of a solid electrolyte candidate requires the same metrics as selecting other electrolyte types in an electrochemical cell. It should have a high ionic conductivity, be compatible with selected battery components, and be easily manufactured. When looking specifically at the lithium-ion conductivity it is important to look not only at the conductivity values, but also the conditions under which these values are measured. In addition, the ability to deliver a high conductivity becomes irrelevant if the material experiences substantial performance loss over time. For example, Li_3N, which was first reported in the 1977, held the record for the highest Li-ion conductivity ($6*10^{-6}$ S cm^{-1}) until recent years. However, this material suffers from a lower electrochemical breakdown potential, which led to battery degradation when employed in traditional Li-ion batteries. [115] In traditional Li-ion batteries, materials, such as $Li_{10}GeP_2S_{12}$, have demonstrated bulk conductivities of over 10^{-2} S cm^{-1}. [116]

Typically, solid electrolytes are broken into different categories including polymer electrolytes and glass-ceramic electrolytes. A more in-depth review of polymer electrolytes was presented by Zhao et al. [117] But a brief overview of the topic will be presented to motivate the selection of the solid electrolyte utilized for in-

situ studies presented here. As highlighted by Song et al., polymeric electrolytes aim to suppress lithium dendrite growth, accommodate volumetric changes, offer better electrochemical stability, improve safety, and improve flexibility and mechanical stability. [118] Polymer electrolytes in general are categorized as either a pure solid polymer electrolyte or a gel polymer electrolyte. [117] The goal of the polymerization process is to take the favorable characteristics associated with the chosen liquid electrolyte and combine them with the mechanical stability of the polymer. [119] Understandably, the properties of the resulting PE strongly depends on the liquid electrolyte, and the polymer used as the matrix. Initial studies on PEO-Li_X polymer electrolytes demonstrate a common limitation of this type of electrolyte. In order for lithium transport to occur, the material was required to be in an amorphous state. This state occurs at temperatures exceeding 60C (PEO-LiX). [120] As a result, the batteries perform poorly at room temperature.

The mechanism of ion conductivity depends on the microstructure of the polymer membrane. If the liquid electrolyte has a high number of confined pathways, resulting from the presence of interconnected micropores, ion conductivity is determined by the liquid electrolyte itself. [117] In a polymer electrolyte that does not have these interconnected pores present, the majority of ion conduction occurs in the polymer membrane. In 2006, Ryu et al. proposed a mechanism for the electrochemical behavior of a polyvinylidene fluoride-based GPE. The first charge-discharge curve demonstrates typical behavior. There are two plateaus associated with the reduction of higher order polysulfides, followed by the reduction of lower order polysulfides to form the lower order polysulfides. Following the first cycle, the

higher order plateau disappears. Therefore the GPE suppresses the formation of higher order polysulfides, which greatly improves the cycle life of the cell.

The second class of solid electrolytes which have shown promise are electrolytes based on glass-ceramics. Glass materials, in general, are expected to perform better as ion conductors due to their lack of grain boundaries, which could act as scattering sites. [121] Lithium-sulfide glasses are expected to be advantageous due to the polarizability of sulfur, lack of grain boundaries, and the ability to create thin films due to their fine powder. Typically based around sulfur, they exhibit high ion conductivity due to the high polarizability resulting from sulfur's insulating nature, which leads to a higher ionic conductivity. [122] From a fabrication point of view, glass-ceramics offer favorable processing techniques. Polymer electrolytes require the use of a melt-quenching technique. The electrolyte materials are placed under vacuum and melted at temperatures exceeding 1000C. Following melting they are rapidly quenched to room temperature . [123] A slower quenching rate yields a higher probability of crystallite formation.

4.5 $Li_2S+P_2S_5$ Solid Electrolyte

Comparatively, $Li_2S+P_2S_5$ glasses have been shown to possess a high ionic conductivity, favorable fabrication techniques, and strong electrochemical performance. [124] These materials are typically produced through the previously described method of melting, then rapidly quenching to room temperature. Using this methods, ionic conductivities of 10^{-4} Scm^{-1}, were demonstrated. For ease of production, we sought a solid electrolyte which was more easily fabricated. Hayashi

et al., demonstrated the preparation of $Li_2S+P_2S_5$ glasses using only mechanically milling. The produced electrolyte possessed conductivity on the order of 10^{-4} S cm^{-1}. [125] This method is advantageous largely because it is performed at room temperature and is capable of creating a fine powder, which can be utilized as a thin-film electrolyte [126]

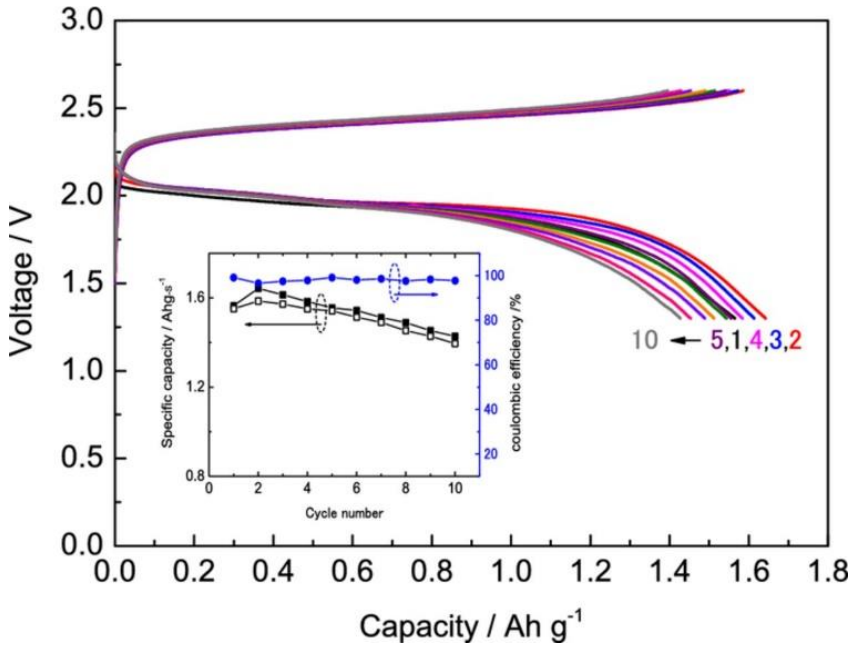

Figure 4.2: Electrochemical performance of Li_2S-P_2S_5 solid electrolyte coin cell. [127]

Yaada et al. report Li-S batteries based on mechanically milled $Li_2S+P_2S_5$ solid electrolytes. [127] The results can be seen in Figure 4.2 They have demonstrated initial discharge capacities of 1600 mAh/g, with stable cycling performance over the first 10 cycles. Immediately, the lack of upper plateau typically associated with the formation of high-order polysulfides is noticeable. The group attributes the lack of the upper plateau at 2.3V to the high polarization associated with the transition to the S.E.

Our goal is to employ the $Li_2S+P_2S_5$ to investigate its ability to provide an additional superionic state that could enable the lithiation of a sulfur phase within the TEM. Upon achieving this goal, we further aim to study the reaction kinetics related to this formation. In addition, we want to explore some of the additional benefits described by the literature related to the stability of this S.E. Lastly, we hope to investigate the role of CNTs in this reaction.

4.6 Results and Discussion

4.6.1 Li/Li_2O Solid Electrolyte

The method of sulfur incorporation plays an important role in the results of our in-situ experiments. Initial tests utilized high temperature sulfur incorporation. The MWCNTs are processed similar to the experimental methods outlined in Chapter 3. Briefly, the MWCNTs are oxidized in air, followed by high temperature filling at 600 ˚C for 48 hours. Sulfur to MWCNT ratios of 10:1 were loaded into the sealed test tube. Following filling, the samples are mounted using the methods outlined in the earlier section of this chapter. Despite the high sulfur to carbon ratios prior to filling, the amount of sulfur present in the system following filling is extremely low. This could result from a few scenarios: 1) We successfully filled the MWCNTs with sulfur2) The sulfur which was incorporated into the MWCNTs was sublimated resulting from exposure to the beam 3) Our sulfur incorporation protocol was unsuccessful. While our initial aim was to study the formation of lithium sulfides, our initial studies yield valuable information on the anodic process.

The in-situ studies utilizing a Li/Li_2O layer demonstrate much slower reaction kinetics. Typically, little to no activity is seen following initial contact between the MWCNT and the Li/Li_2O anode. When applying a significant overpotential, it was possible to activate the Li anode, after hours of biasing. This activation is typically shown by the formation of spherical Li deposits which form on the surface of the anode. Over time, this surface becomes more and more complex, forming a variety of shapes and sizes. These structures are crystalline, based on Bragg reflections seen during changes in their orientation. In addition to the spherical dendrites formed during Li activation, higher aspect ratio features can be seen. These tend to grow more rapidly, but are lower in density. They tend to occur at higher rates when the activated Li growth front approaches the cathode material.

The expected "activation" reaction for the anodic process is as follows:

$$Li_M \rightarrow Li^+ + e^-$$

$$Li_M^+ \rightarrow Li_O^+$$

This results in highly mobile, active lithium ions which either interact with the carbon nanotubes or the sulfur, depending on the point of contact. We will first look at the cases of CNT/lithium interactions.

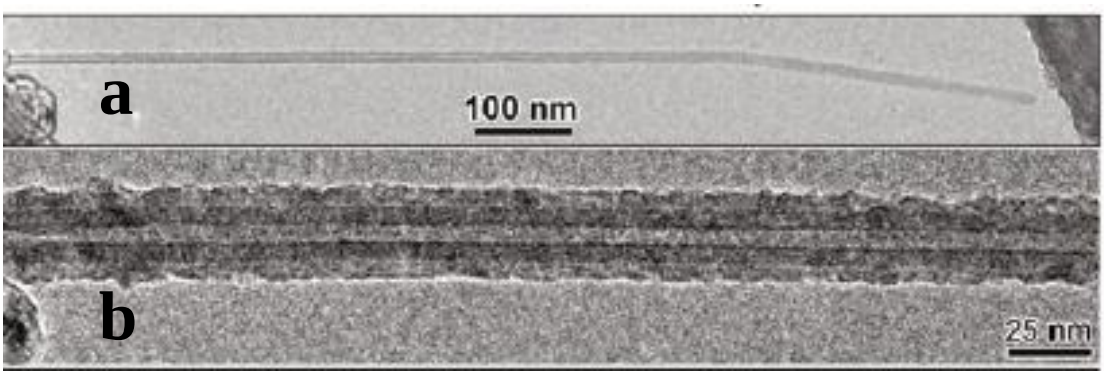

Figure 4.3: Lithiation of MWCNTs. (**a**) Pristine MWCNT with a diameter of about 15 nm before contacting the Li_2O/Li electrode. (**b**) Lithiated MWCNT showing a uniform Li_2O layer coated on the surface. [105]

Previous work has been done to study the physical properties of CNTs in-situ in the TEM [128] Using a similar set-up to our experiment, they brought a lithium-coated manipulation tip into contact with the CNTs and studied the ability of the CNTs to withstand stresses induced by bending. Using a potential of -2 V relative to the Li electrode, they were able to see an expansion of the interlayer spacing from 3.40Å to 3.60Å upon lithiation. A CNT, before and after lithiation, can be seen in Figure 4.3. We did see possible evidence of this radial expansion but, due to the beam sensitivity of the lithium shells formed on the surface, high magnification images were not taken. Typically, intercalation of lithium into MWCNTs occurs below 1V. [129]

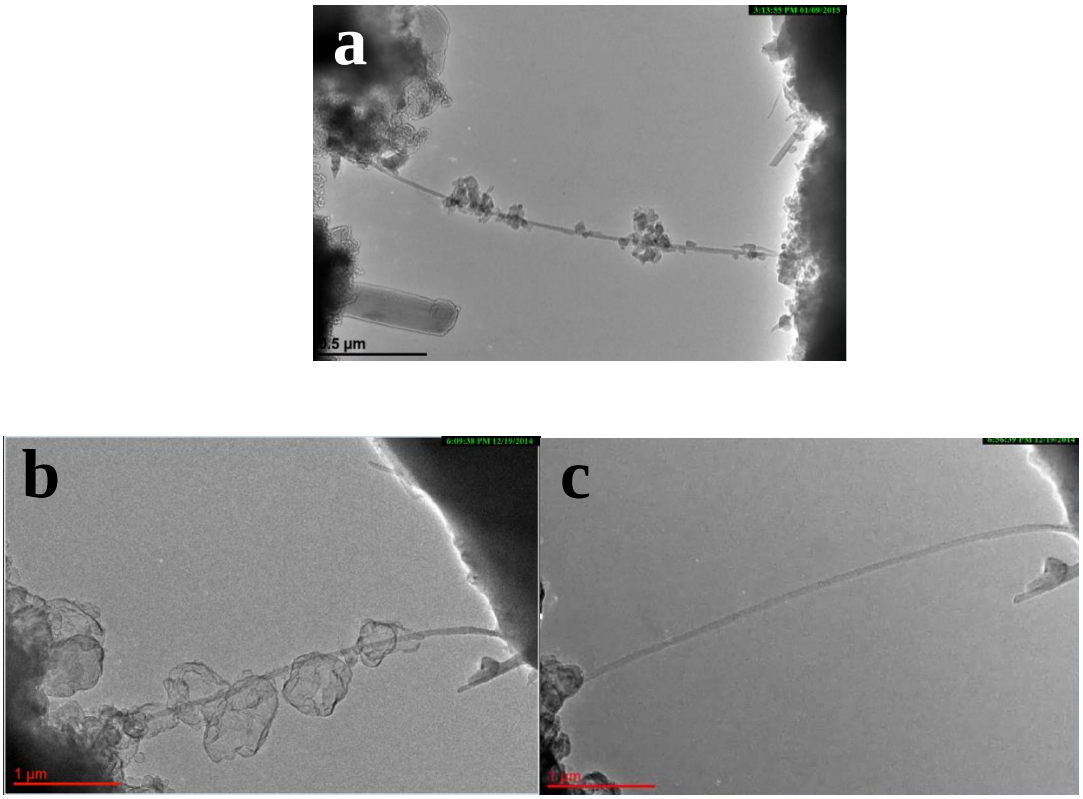

Figure 4.4: MWCNT/Li interactions. (**a**) MWCNT covered with carbon debris following extraction from the bulk (**b**) MWCNT with Li-rich phases which diffused across the length of the MWCNT (**c**) Same MWCNT after beam exposure for 10 minutes

However, we did observe other interesting interactions between the carbon nanotubes and lithium. The main method of detecting transport of lithium was the presence of external lithium shells on the surface of the MWCNT. For comparison, two similar orientations, with a MWCNT spanning the gap between the Li anode and the CNT cathode are presented in Figure 4.4. Figure 4.4a was formed after the anode was brought into contact with the cathode material. The probe was then pulled backward in the –Z direction which pulled the MWCNT out from the bulk material. As a result, some of the carbon material from the bulk, was extracted and remain decorated on the surface of the MWCNT. In the case of Figure 4.4b, the configuration

was produced by slowly bringing the probe into contact with the MWCNT directly. As a result, no similar carbon material is visible on the surface of the MWCNT. Figure 4.4b was after 2 hours of applying a bias of +11V. These oxide shells were similar to the shells which are also visible on the anode. The Li/ Li_2O shells are sensitive to beam damage and as a result, were able to be destroyed within minutes. Comparatively, the CNT imaged in Figure 4.4b showed little to no evidence of beam-induced destruction. Over the course of several minutes there is little to no change in the position, or size of the material deposited on the surface of the CNTs.

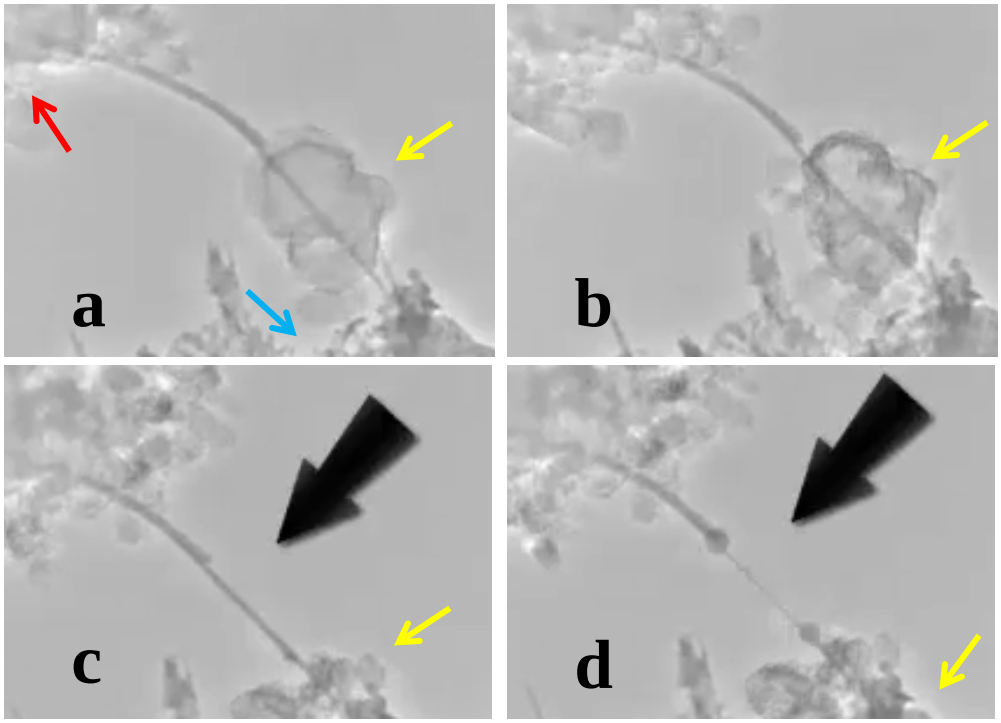

Figure 4.5: Failure Mechanism of Li Diffusion through CNTs. (**a**) MWCNT/S composite material with large Li-rich phase reaching the bulk cathode material (indicated by red arrow) (**c**) Point at which Li-rich phase is completely consumed into the bulk MWCNT/S cathode material (**d**) Resulting structure after failure occurred which shows multiple walls of the MWCNT stripped away. The red arrow indicates the Li/Li_2O anode. The blue arrow indicates the bulk MWCNT/S cathode. The yellow arrow shows the position of the Li-rich phase. The black arrow is the failure reaction site.

Failure mechanisms of sulfur/MWCNTs can be seen in Figure 4.5. Figure 4.5a shows a carbon nanotube which spans the gap between the lithium anode and the cathode bulk material. The initial frame shows the presence of lithium shell which has diffused down the length of the MWCNT. These shells are likely a lithium-rich phase. Due to the instability of the shells under the electron beam, characterization using EELS was not possible. In addition, the shells were only observed at lower magnifications. Eventually, the shells reach a kink in the MWCNT. At this point,

diffusion slows and the lithium shells eventually begin to coalesce to form two faceted, larger crystals. The phase continues to grow until it reaches the cathode material. At this point, it is likely, that the initial stages of lithium sulfide formation occur, as the lithium-rich phase is quickly absorbed into the bulk sulfur cathode material. Shortly following the complete consumption of the lithium, an abrupt structural transformation of the carbon nanotube occurs.

Following the lithium consumption, a single layer, or multiple MWCNT layers, is stripped away. This results in a fewer number of MWCNT layers and two spherical, carbon features at either side of the MWCNT. We think there are two possible mechanisms which could have caused a transformation similar to this. The first is the formation of a vitreous, or glassy, carbon phase. This type of carbon was first proposed in 1963 by Cowlard et al., and is described as a carbon phased formed at high temperatures which exhibits properties markedly different than those of traditional graphite. [130] The formation of this material typically occurs at temperatures exceeding 1800 ˚C, therefore in order for this reaction to occur, a rapid heating event occurred. [131] This rapid heating event could have been caused by the formation of a highly conducting phase, which resulted in the rapid transfer of electrons which subsequently heated the samples to sufficient temperatures. Or conversely, a lithium sulfide phase (Li_2S), which is known to be electrically insulating, caused the sample to charge, and heat up.

The second possible explanation is that in addition to the lithium phases being transported on the outer portion of the MWCNTs, additional transfer of lithium atoms occurs within the MWCNT. This would be similar to past reports that lithium atoms

diffuse through the walls of the MWCNTs. [129] When the large coalesced lithium-rich phase is consumed by the sulfur cathode, there is a formation of a Li_2S phase, which acts as a "plug", preventing the continued diffusion of lithium through the inner diameter. As more lithium is driven into the inner cavity of the MWCNT, the additional lithium is forced to diffuse preferentially through defect sites within the carbon nanotube. This outward diffusion could result in the breaking of the nanotube walls preferentially at these defect sites, causing the un-rolling of the walls themselves. In MWCNTs with low defect densities, the breaking of these walls would be more likely to occur in comparison to those which have multiple defect sites.

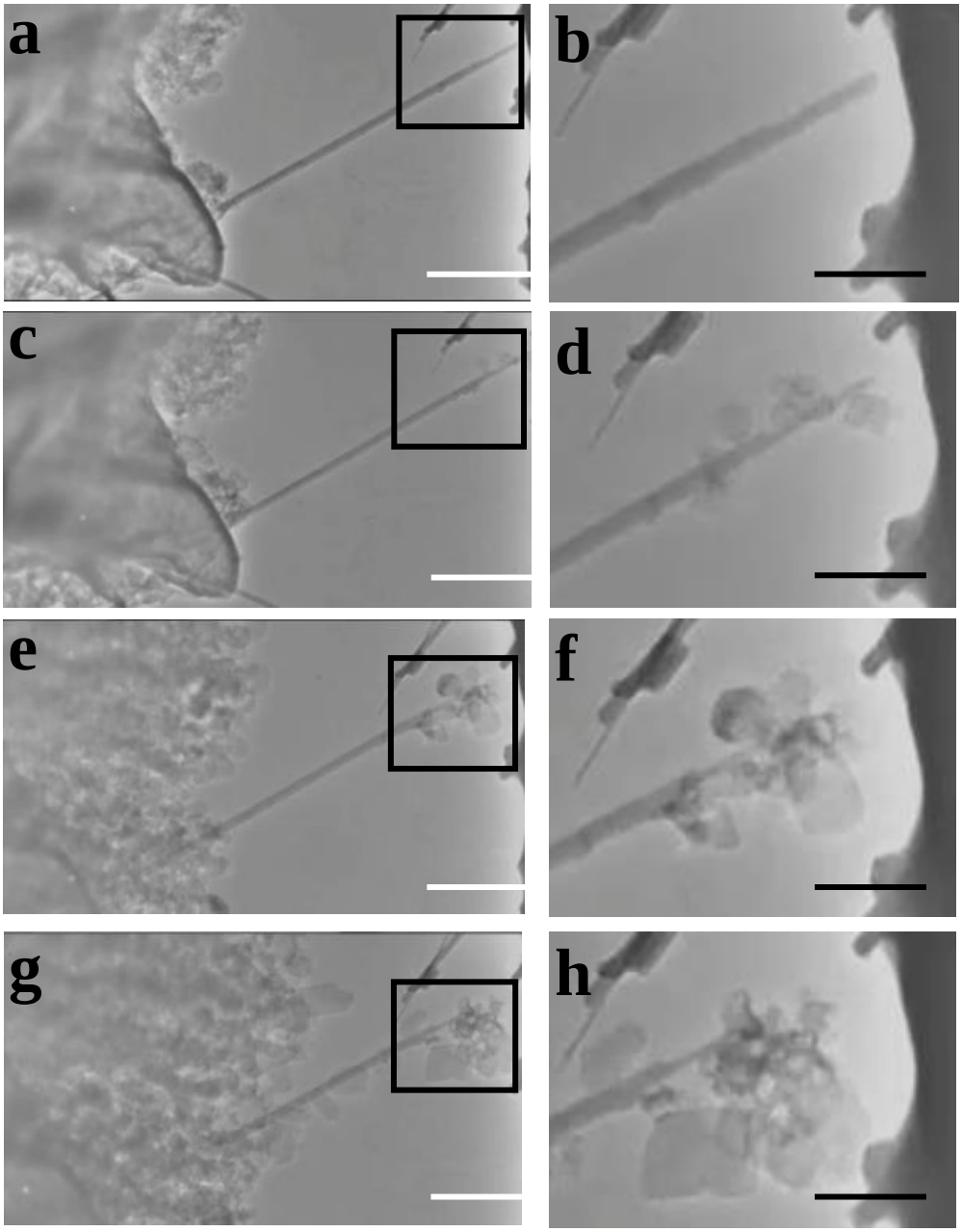

Figure 4.5: Lithium interactions with MWCNT/S composite material with applied voltage of +6 V (**a,b**) initial configuration (**c,d**) 2 minutes (**e,f**) Area after 2 minutes (**g,h**) 4 minutes (e) 8 minutes.(**b,d,f,h**) are higher magnifications of the highlighted regions in (**a,c,e,g**) respectively.

A second demonstration of lithium diffusion through the inner diameter of a MWCNT is shown in Figure 4.5. The configuration for this structure varies slightly from the previous case. During this experiment, the Li/Li_2O anode was brought into contact with the MWCNT/S cathode. The manipulation tip was then moved in the –Z direction, to create a small gap between the anode and cathode. During this step, the MWCNT broke at the site indicated by the arrow in Figure 4.5a. While slightly, disadvantageous, this geometry allows again for the study of lithium diffusion both on the surface, as well as, within the interior of a MWCNT.

During the initial stages of transport, the presence of lithium on the surface of the MWCNTs is evident. Due to the detachment of the MWCNT at one side, it is apparent that there is transport occurring due to the accumulation of lithium at the tip of the MWCNT. The accumulation of this lithium phase progresses until it is large enough to make contact with the sulfur cathode. At this point, lithium begins to appear along the length of the MWCNT at the sites indicated by arrows. These experiments confirm that lithium transport for in-situ experiments occurs both on the surface of the MWCNT and within the inner diameter. We expect that the rate of diffusion for lithium is higher within the CNT due to the possibility of beam effects in other locations. Figure 4.6a shows a MWCNT which has been exposed to lithium. After exposure to the beam for 35 minutes, these shells have been completely destroyed (Figure 4.6b). The protection offered by the MWCNT under imaging conditions, allows for the uninterrupted transport of Li.

In order to increase the amount of sulfur present in our samples, the sulfur incorporation step was modified to maximize the amount of sulfur. Following

mounting of the MWCNTs to the brass stubs, the samples (glued on brass stubs) were mounted onto an aluminum sample/brass stub holder and placed within a glass dish. Sulfur was placed on a glass slide, then loaded into the glass dish. The glass dish was then covered and loaded onto a hot plate. Thermal evaporation was carried out at 160˚C for 12 hours. Following evaporation, large sulfur crystals are visible under an optical microscope. Large orthorhombic crystals of sulfur are seen during initial imaging conditions.

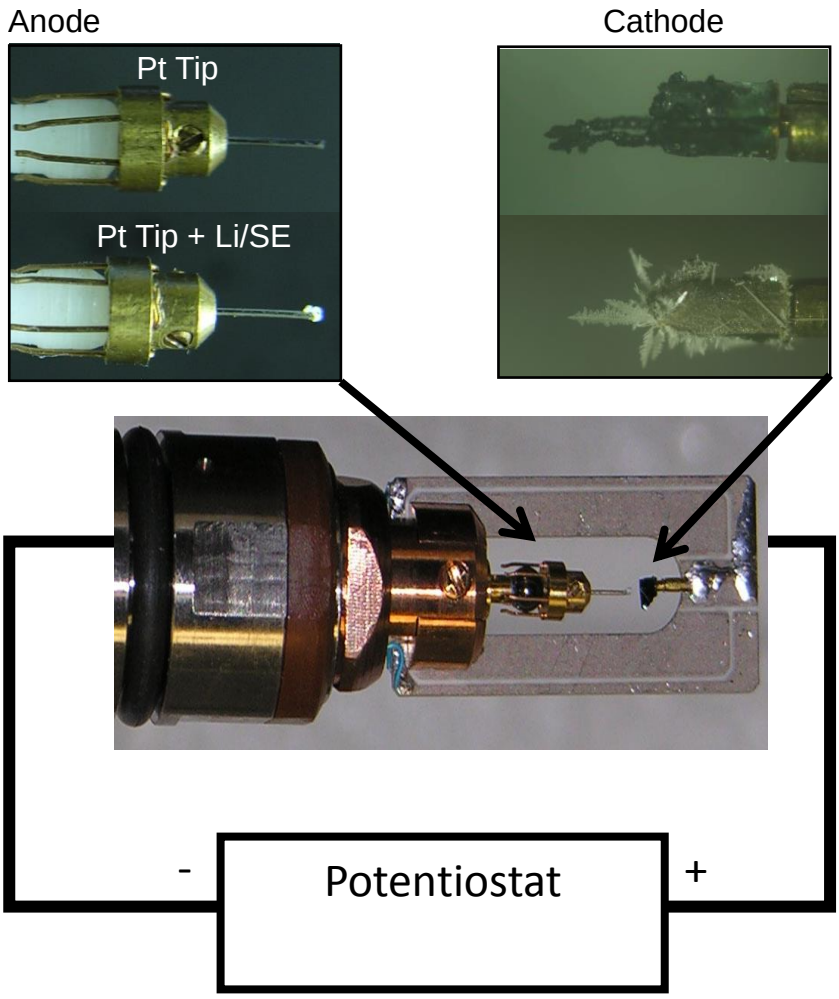

Figure 4.7: In-situ experimental set-up for Li/MWCNT-S using Nanofactory holder

While we were able to dramatically increase the amount of sulfur present in our system, the additional sulfur created certain difficulties. First, the sulfur readily sublimates within the microscope under low magnification imaging. Representative images of the evolution of sulfur species can be seen in Figure 4.8. This result is not unexpected, but efforts were taken to minimize the amount of sulfur being evaporated to reduce the amount of contamination in the microscope. Once sublimated, the sulfur could condense on lens components leading to microscope degradation. First the thermal evaporation time was reduced from 12 hours to 2 hours. Any additional time resulted in excessive deposition of sulfur on the sample, including on the brass stub. Following thermal evaporation, any excess sulfur is gently scraped away using a small wooden stick.

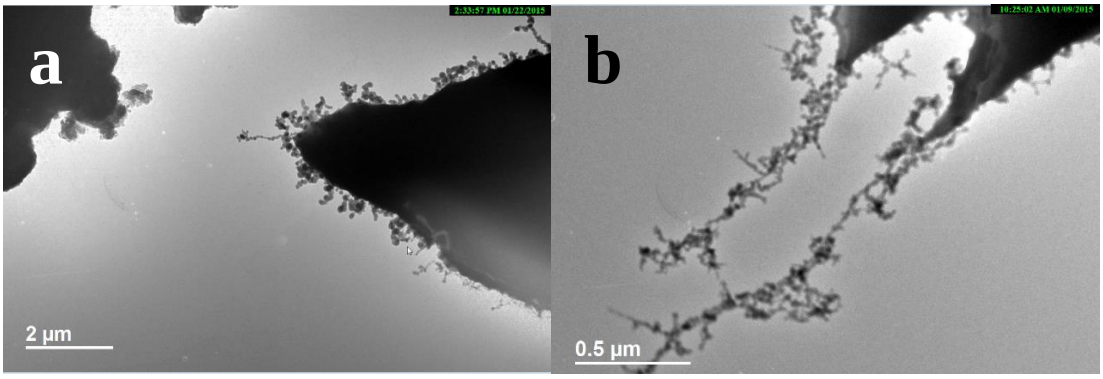

Figure 4.8: Sulfur sublimation in a TEM. (**a**) Early stages of sulfur sublimation from a large sulfur crystal. (**b**) More pronounced sulfur sublimation following longer exposures to the electron beam

In addition to potential contamination of the microscope, excess sulfur has a potentially negative impact on the reaction kinetics. While the presence of sulfur is necessary for the reaction to occur, excess sulfur can increase the resistance of the cathode material. Therefore, it is important to control the ratio of sulfur to carbon. We

commonly encounter inhomogeneity within our sample from region to region caused by uneven deposition of sulfur during thermal evaporation. In addition, during the scraping away of sulfur following evaporation, the sulfur can also be removed unregularly. All of these factors play a determining role in the resulting reactions, or lack thereof, in our experiments.

4.6.2 Li_2S-P_2S_5 Solid Electrolyte

As previously stated, we want to look at three major factors related to the implementation of a Li_2S-P_2S_5 SE. First, we want to study if the addition of a solid electrolyte resulted in faster kinetics allowing for the complete lithiation of our sulfur samples. Second, we want to monitor any changes in the electrolyte that could serve as potential failure mechanisms related to the battery's failure or degradation. In addition, we want to see if the CNTs altered the reaction of lithiation/delithiation. Third, we want to compare this to the Li/Li_2O case to see what conclusions we are able to make about lithium sulfur cells.

In our first study, we look at a configuration similar to the Li/Li_2O example, in which we made direct contact with a CNT/S composite. The initial configuration can be seen in Figure 4.9. In comparison to the Li/Li_2O S.E., the reaction behaves differently. Within one second, a small crystal of anode material can be seen on the surface of the MWCNT. This could result from electrostatic forces, but it is an occurrence which we did not see in all of the previous studies utilizing a Li/Li_2O anode.

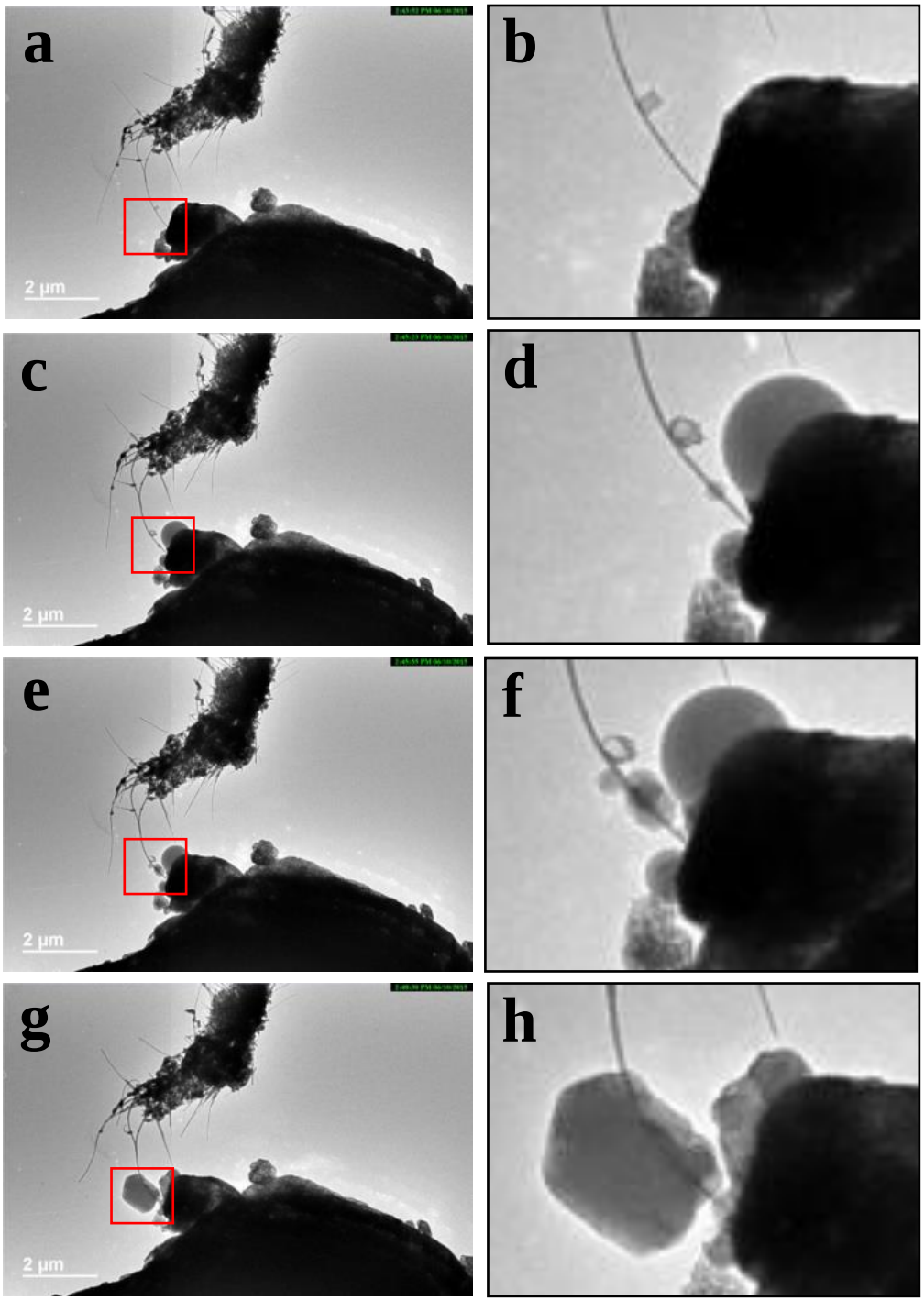

Figure 4.9: Lithium interactions with MWCNT/S composite material with applied voltage of +6 V utilizing $Li_2S+P_2S_5$ SE. (**a,b**) 1 second after contact (**c,d**) 30 seconds after contact (**e,f**) 4 minutes after contact (**g,h**) 5 minutes after contact. (**b,d,f,h**) are higher magnifications of the highlighted regions in (**a,c,e,g**) respectively.

Following the immediate appearance of the initial crystal, additional crystals begin to form at different points along the length of the MWCNT. These smaller crystals eventually coalesce into a larger crystal, which continues to grow. We were interested whether the formation of these crystals continues down the length of the MWCNT as we had seen in our previous studies, or whether these crystals served as a blocking site.

We left the cathode material with an applied voltage of +6V, relative to the sample, for the remainder of the experiment, totaling roughly 1.25 hours. The evolution of the structure can be seen in Figure 4.10. The initial image shows MWCNTs/S composite. There are a large amount of MWCNTs which extend from the mass of the composite. The majority of the sulfur in the system likely resides within the bulk of the material. However, following the demonstration of lithium transport over the MWCNT, we expect the conversion of sulfur to Li_2S_x.

After 45 minutes (Figure 4.10), there is a clear transformation to the structure of the MWCNTs. We see early signs of the coating of the MWCNT with additional material. After 70 minutes (Figure 4.10b) additional formation of a Li_2S layer can be seen resulting in a dramatic increase in the observed diameter. The Li_2S species on the surface of the MWCNTs is confirmed using EELS (Figure 4.10b). Figure 6c, shows a higher magnification of one of the MWCNTs which is encapsulated within the Li_2S layer. The Li_2S material is confirmed using EELS and can be seen in Figure 4.11.

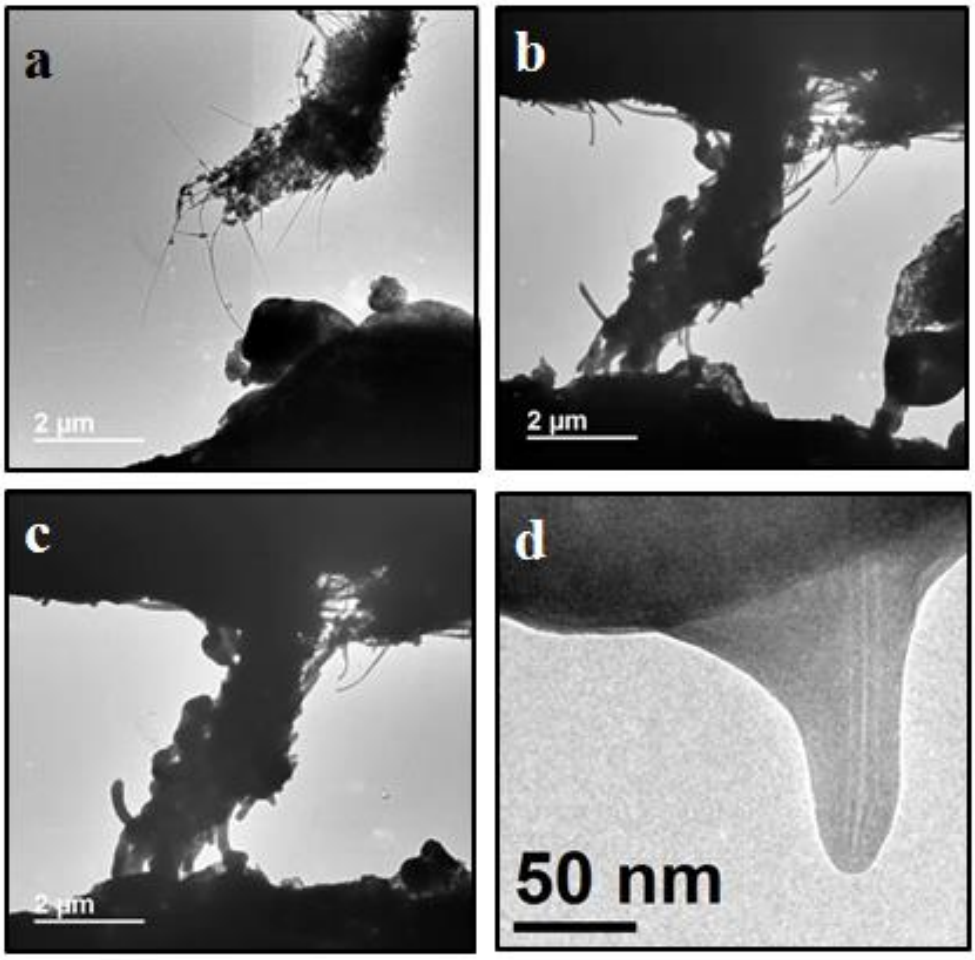

Figure 4.10: Li_2S_x formation on MWCNTs. (**a**) initial configuration after contact with +6V applied (**b**) After 45 minutes with applied +6V (**c**) After 70 minutes with applied +6V (**d**) Higher magnification image of MWCNT embedded in Li_2S_x coating.

The previously described reaction was in a MWCNT rich area. We also demonstrate the formation of a lithium sulfide phase in areas that are sulfur-rich. The reaction is summarized in Figure 4.11. Figure 4.11a. The figures show the anode (indicated with a black arrow), in contact with the cathode (indicated with a yellow arrow). The point of contact is labeled with a red arrow. Prior to Figure 4.11a, the two electrodes were placed in contact with each other without an applied bias. We observe the conversion of the sulfur to a darker contrast lithium sulfide over the course of 3

hours. Once we achieve this charged state, we are able to achieve a complete reversal by applying a reverse potential of -6V. Upon reversal of the potential to (+6V), the remaining darker phase returns, with residual lighter phases located at different parts of the sample. When we attempt to reverse the bias to "delithiate" the sample for the last time, we cannot obtain complete reversal. It is possible that the two electrodes could have separated from each other due to partial sublimation of the sulfur cathode. Another possibility is that there is an insulating layer which is blocking Li transport from continuing. This would suggest that similar to the previous MWCNT experiment, this would demonstrate electrolyte breakdown.

One interesting note is that the contrast of the lithiated and unlithiated samples, are not what would be expected from simple lithium shuttle transport. Given that the density of lithium is less than the density of sulfur, the lithium material should appear lighter than the unlithiated material. Thus, it appears that we are seeing a different phenomenon than pure lithiation of sulfur. We suspect that instead of seeing simple lithiation and delithiation, we are actually observing a degradation mechanism associated with the Li_2S-P_2S_5 SE.

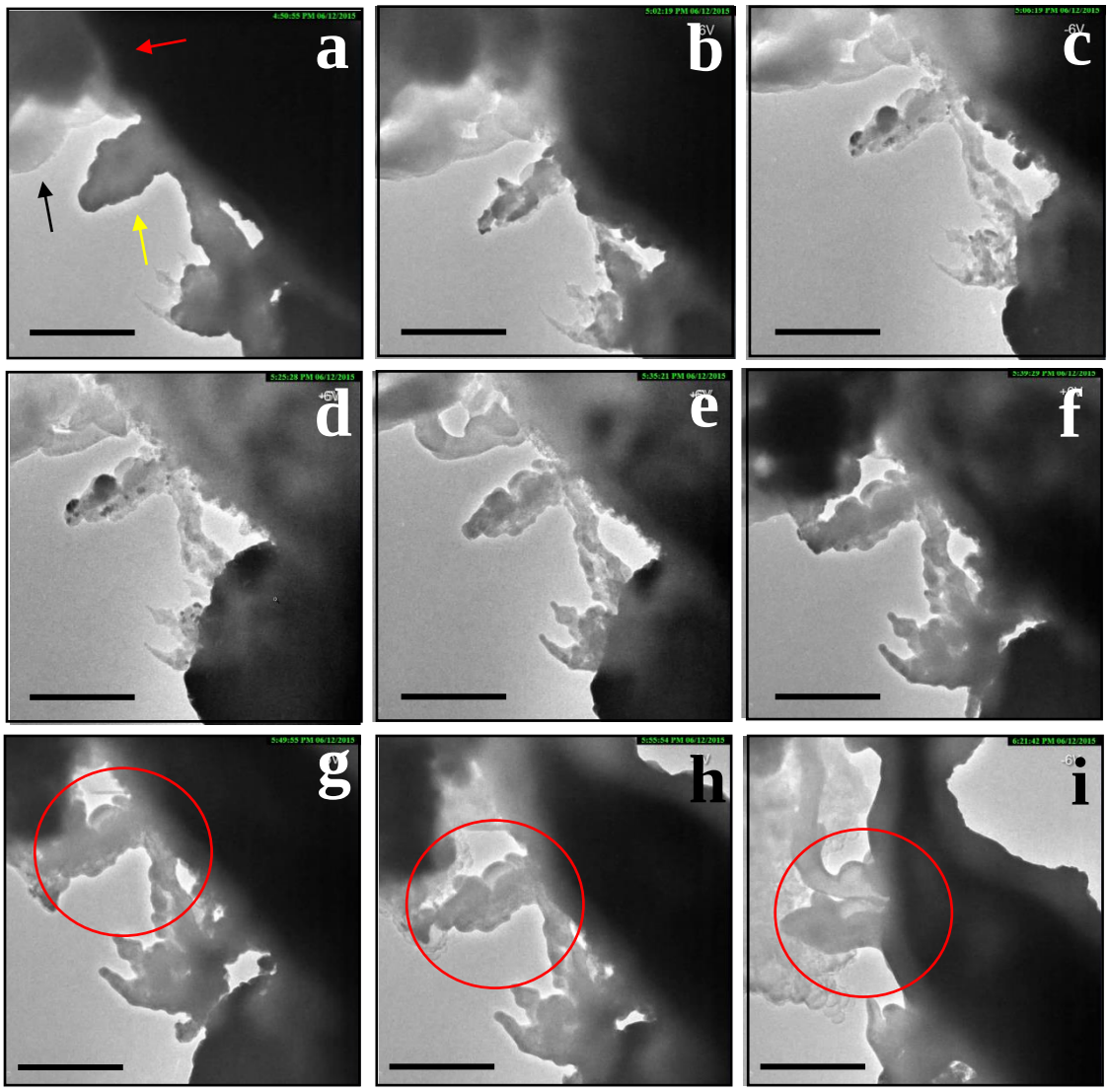

Figure 4.11: Lithium interactions with MWCNT/S composite material using a Li2S-P2S5 SE under an applied voltage of +/-6V. (**a**) First applied voltage of -6 V (**b**) 12 minutes at -6 V (**c**) 15 minutes at -6 V (**d**) First applied voltage of +6 V (**e**) 10 minutes at +6V (**f**) 15 minutes at +6 V (**g**) First applied voltage of -6V (**h**) 5 minutes at -6V (**i**) 30 minutes at -6 V. All scale bars are 0.5 µm in length.

Following cycling, EELS analysis is used to characterize the sample. The initial EELS spectrum of the cathode material can be seen in Figure 4.12, showing characteristic features of sulfur with a broad peak at 22 eV corresponding to the S $L_{2,3}$ edge. This spectrum was taken prior to making contact with the lithium anode, so we

expected no traces of lithium. A second spectrum was taken from the cathode depicted in Figure 4.11i. A clear peak at 55 eV, which is in agreement with the Li K-edge. Therefore, we concluded that the cathode is in fact a lithiated state.

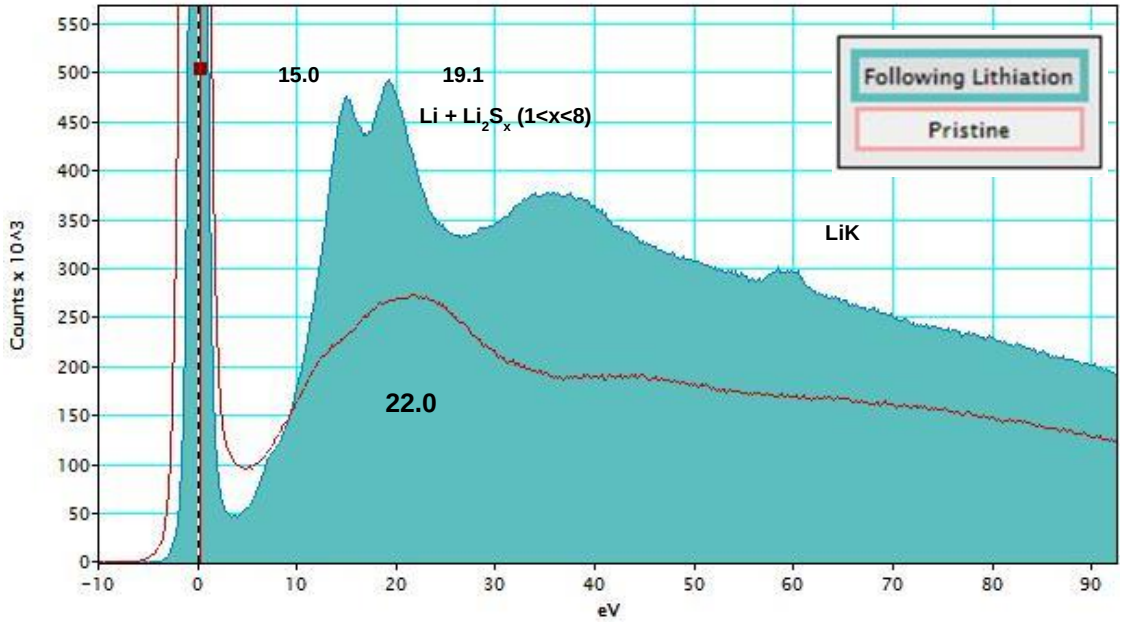

Figure 4.12: EELS Analysis of MWCNT/S Composites before and after in-situ TEM cycling

4.7 Conclusions

Through the use of in-situ TEM studies, we have provided insight into the reaction mechanisms of lithium-sulfur electrochemistry for different types of cathode structures. In looking at areas which contain majority MWCNTs, we have shown the lithium can selectively diffuse along the lengths of these CNTs to provide an electrically conductive pathway for Li transport. We have further shown the ability to select the transport regime through modifications of the beam intensity. By increasing the beam intensity through imaging at higher magnifications, we have shown that the

lithium transport on the outer surface of the MWCNT is blocked, limiting transport to inner channels.

Using a voltage which exceeds the typical operating window of currently utilized Li-S cells, we have shown accelerated electrolyte degradation. In experiments that use a Li/Li_2O electrolyte, we have demonstrated the formation of Li dendrites which are a common factor in the failure of Li-S cells. By transitioning to a Li_2S-P_2S_5 SE, we have shown the suppression of dendritic growth, which clearly demonstrates one of its main advantages. However, we also have shown that electrolyte breakdown at these higher voltages results in the diffusion of Li_2S species to coat the cathode material. This Li_2S_x species is likely electrically insulating, so we expect this would lead to battery failure and an inability to continue cycling.

Chapter 5: Conclusions & Outlook

5.1 Lithium-sulfur batteries

Very rarely, do we go more than an hour without utilizing one, or more, of our cellular phones, laptops, or tablets. For some, it is hard to imagine, or recognize, that an action as simple as checking an email, or social media page, can have such a large impact on the world. Another daily occurrence such as choosing to drive alone, in lieu of carpooling, or utilizing public transportation can also have a large effect on the environment, through increased CO_2 emissions. Each of these seemingly harmless actions consumes energy and the methods which are used to produce this energy are causing irreversible damage to our environment. The mounting evidence of global warming is making the world more aware of the harmful effects of our energy dependence. While also a potential cause, the advent of social media makes it easier to see the effects of our actions.

In a utopian society, the declaration that we are destroying our environment through our lifestyle choices would invoke radical changes to the way we live. Unfortunately, this is far from the reality that exists today. As a result, we instead aim to improve the technologies which shape our daily lives. As has been demonstrated throughout this dissertation, lithium-sulfur cells show great promise in their ability to fill the need for a low-cost, high-performance electrochemical cell. Recent progress on the creation of novel, cathode structures for Li-S cells have further revealed their potential as a revolutionary technology.

Lithium-sulfur batteries present a very appealing technology from both a research and commercial perspective. From a research perspective, there still remain many avenues which can be explored to improve and understand the cycling behavior of lithium-sulfur cells. The Li anode which provides a high capacity has primarily been improved through the implementation of protective coatings which dampen the effects of the polysulfide shuttle. Similar to the Li anode, the polymer separator has received attention through coatings to allow for the selective diffusion of Li^+ ions and detainment of polysulfide species.

The creativity in designing new experiments and equipment has further expanded the understanding which we are able to achieve. Starting with TEM experiments, the achievable imaging resolution has been improved greatly in recent years due to the development of aberration corrected TEMs. While higher magnification, does not always equate to better results, the ability to achieve these at lower accelerating voltages allows for the imaging of highly beam-sensitive materials. In addition, the development of new equipment such as TEM holders which enable seemingly impossible studies has further progressed the field of in-situ TEM.

5.2 Future work

5.2.1 Graphene/Sulfur Composites

The main difficulty in conducting TEM studies on sulfur species is the sublimation of sulfur. Sulfur easily sublimates at the base pressures for most

conventional TEMs. Therefore, we seek to create a structure which allows for the use of various analytical TEM techniques with minimal loss of sulfur. We achieve this through the fabrication of graphene/sulfur layered structures which prevent this process. By covering the sulfur with graphene, we are able to greatly expand the number of experiments that can be done using TEM. We use CVD-grown which is synthesized to enable the use of commonly used wet transfer techniques without a polymer support. This prevents any potential damage to the sulfur during the polymer removal process. Using these structures we are able to demonstrate HRTEM lattice imaging, spectral imaging, electron diffraction, and other analytical techniques which are beneficial to TEM studies.

Future work includes further optimization of the fabrication procedure. There are still rips and tears which are currently unavoidable due to the transfer procedure. Therefore, we hope to explore different techniques, such as PDMS stamping, to create better quality layered structures. This difficulty has also limited our ability to scale up to coin-cell sized samples, which would allow us to directly test the ability of graphene to act as a physical barrier to prevent the polysulfide shuttle process in a working battery.

Perhaps the most desirable aspect of this study is the further development of different TEM characterization experiments. This set-up is ideal for in-situ work and will be utilized to study the properties of sulfur under a variety of conditions. The first experiment which we hope to complete is the melting of sulfur through joule heating. Using different techniques, such as EELS, we aim to study the electrical properties of this material as it undergoes melting. Similar to the case of the SWCNTs which were

filled with sulfur, we hope to study the potential confinement induced transformations. Our recently constructed TEM electrical holder, would be utilized to study this system. (Appendix A)

In addition to the specific properties of sulfur in this arrangement, we aim to explore potential chemical alterations of the sulfur when confined between the two graphene sheets. 1,3-Diisoproponylbenzene (DIB) has been shown to improve the electrochemical performance of Li-S cells, through the chemical stabilization of sulfur through an inverse vulcanization process. [132] We hope to study the electrochemical properties of the material in both cases.

5.2.2 Sulfur Filled CNTs

Through our studies of the electrochemical performance of sulfur-filled SWCNTs, we have shown a direct correlation between the thermal oxidation and the resulting electrochemical performance. For the unoxidized SWCNTs, cells exhibit typical behavior for lithium-sulfur cells with major capacity fading over the first 10 cycles associated with the polysulfide shuttle process. For the 375 ˚C sample, we see similar capacity loss. However, we observe the first evidence of sulfur-filling in the electrochemical data in the form of a third plateau at a lower voltage. We suspect that this additional feature is related to the encapsulated sulfur. This feature appears again in both of the 475 ˚C and 575 ˚C samples. Therefore, at the oxidation temperature of 375 ˚C, certain sites are opened to allow for sulfur infiltration, but these sites also allow the polysulfide shuttle to occur, as evidenced by the capacity loss within the first few cycles. SWCNTs which were oxidized at 475 ˚C, showed stable cycle

performance and maintain a high discharge capacity. At 575 ˚C, we again see the additional plateau associated with encapsulated sulfur, but we still see the polysulfide shuttle loss.

Our future work involves modeling thermal oxidation as a function of temperature to demonstrate the preferential oxidation at certain defects for our tested temperatures. We plan to use a graphene sheet as a model system to study the effects of thermal oxidation in air. We suspect that this will build an explanatory model of our electrochemical results. By studying pristine and defect-containing graphene sheets, we expect to see a difference in the oxidation behavior at each temperature studied. Using these findings, we hope to provide insight into the mechanisms of the filling of SWCNTs with sulfur. In addition, this would shed light on the ability of sulfur-filled SWCNTs to act as a potential cathode material.

We also would like to explore other methods of sulfur filling. We are currently working with Dr. Malachi Noked of Prof. Rubloff's group to develop higher yield filling methods. In particular, we will use a liquid based filling method in which thermally oxidized SWCNTs are placed in a Li_2S_x solution and heated to allow for sulfur filling. We expect that the enhanced diffusivity of Li_2S_x versus sulfur, will allow for better filling of the SWCNT structures. In addition to characterization of this structure to determine yield rates, we hope to test these in electrochemical cells.

5.2.3 In-situ Transmission Electron Microscopy Studies of MWCNT/S composites

Through our in-situ TEM work, we explore a wide range of dynamic processes which are related to different aspects of lithium-sulfur electrochemistry. In the employment of a solid electrolyte, we show one possible degradation mechanism which could lead to battery failure within a solid-state Li-S cell which utilizes a Li_2S-P_2S_5 solid electrolyte. We have demonstrated the diffusion of electrolyte material which occurs at operating potentials of +6V. We have also demonstrated that this material can be removed through the application of a reverse bias. However, our results show that after a certain number of cycles, the loss of material within the electrolyte is irreversible. We still are in the process of understanding how this material diffusion would alter the electrochemical performance of the cell, but we suspect that it would cause rapid capacity fading.

In looking at areas which consist primarily of MWCNTS, we saw preferential diffusion of lithium along the length of the MWCNT. Using these results, it is possible to study the rate dependence of lithium transport as a function of lithium diffusion path. We believe that the transport path can be manipulated by beam intensity, due to the sensitivity of lithium to beam damage. Therefore, by altering the beam intensity we can change the transport regime for lithium diffusion. We hope to model this behavior and relate it to other recent reports which examine the induced electric field for precise control of lithium movement within a MWCNT. [134]

Appendix A: Custom-built TEM Holder

A.1 Introduction

In recent years, nanomaterials have received a tremendous amount of attention due to their exotic and highly tunable properties. As a result, many different techniques have emerged to study these materials, each providing a small contribution to the overall scope of understanding. Transmission electron microscopy (TEM) has emerged as one of the most commonly used, and most powerful, methods of characterizing these different structures. Techniques such as electron energy loss spectroscopy, energy dispersive x-ray spectroscopy, electron diffraction, and other analytical techniques allow the ability to obtain chemical, structural, and morphological information on the systems being studied. Furthermore, in-situ TEM studies allow the direct correlation between these types of information and the material's performance during operation. TEM studies rely on the development of custom TEM holders which can provide an analogous environment to the system being studied. Typically, the system's requirements lead to a highly specialized and expensive holder, which lack the versatility of other characterization methods. In addition, they often require the use of custom TEM chips which further drives up the cost of studying, and further improving these devices. Consequently, there is a high demand for custom TEM holders capable of studying a variety of different systems.

Here, we present the design of a custom *in-situ* electrical holder suitable for the study of electrical devices, heating experiments, electrochemical testing, magnetic materials, and many others. It uses commercially available TEM membranes which

can be patterned for up to eight electrical contacts. In addition, the TEM holder provides electrical isolation of the sample for efficient grounding, or application of an external bias. This enables the study of highly sensitive electrical devices and further expands the capabilities of the tool.

A.2 Design Considerations

The primary goal of this specimen holder was to provide the capability to study a large range of dynamic systems *in-situ* in the TEM. The principal limitation in designing experiments for *in*-situ TEM studies is the size restriction of the sample. This limiting factor, established by the distance between the pole pieces of the objective lens in the microscope, limits both the size of the sample, as well as the thickness of the entire holder. The specimen holder thickness further determines the extent to which the sample can be translated, or tilted, which is necessary for certain imaging modes. These mechanical limits are typically detected by applying a constant potential to the specimen holder. When the mechanical limits are reached, the voltage drop is used to halt continued movement of the specimen. For highly sensitive samples, such as carbon nanotube devices, this voltage can damage the sample. For this reason, the holder is commonly grounded during loading to avoid such events. This grounding effectively disables the touch sensor, significantly elevating the risk of an undetected collision during loading. In addition to the voltage used for collision detection, other necessary microscope functions such as the vacuum system emit magnetic fields capable of producing currents large enough to harm devices.

Therefore, it is highly favorable to electrically isolate the sample from the holder to facilitate in-operando studies.

In order to maximize the range of experiments using a new holder design, the holder should be able to operate using commercially available TEM silicon nitride membranes. In addition, the sample size and chip design should allow for multiple electrical connections which can be utilized for *in-situ* experiments. Some form of wire bonding is commonly used for TEM electrical holders to make an electrical connection between the holder and the device. Wire bonding, while creating an excellent connection, serves as a potential source of user error leading to damage of the TEM holder and/or sample. In addition, it leads to the degradation of the holder over time resulting in the necessary replacement of electrical contacts. Other methods such as set screws or are difficult to work with, and often lost. As a result, we seek to simplify the loading procedure.

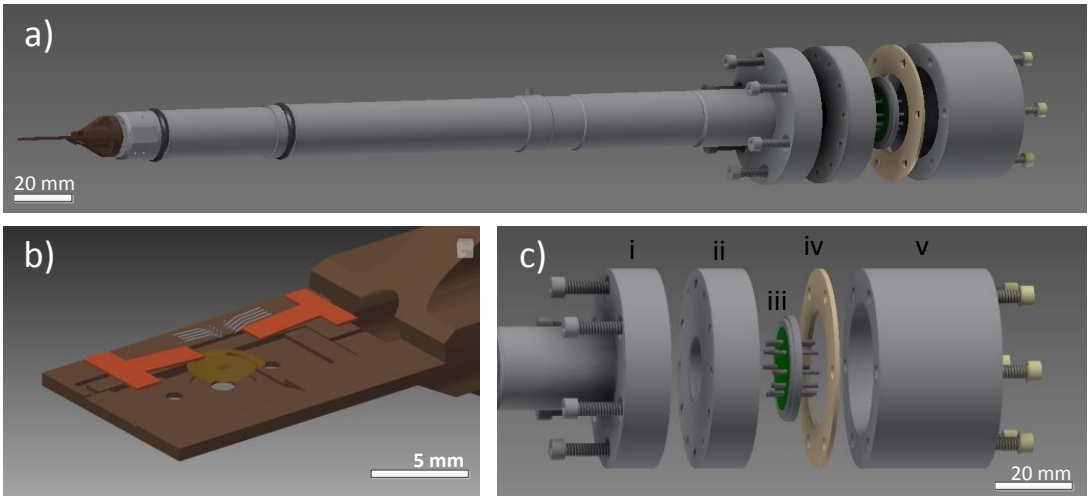

Figure A.1: Schematic render of TEM Holder Design. (**a**) Exploded view of entire holder (**b**) Exploded view of the nose piece c) Exploded view of the handle assembly

A.3 Custom TEM Holder Design

The specimen holder can be separated into three main components: the nose piece (Figure A.1b), the end handle (Figure A.1c), and the holder rod. The exploded view of the entire holder can be seen in Figure A.1a. The holder rod was constructed to fit the JEOL 2100 series of microscopes. However, the holder design itself could be modified to fit other brands of microscope. To construct the nose piece, an insert is glued into place using an electrically insulating epoxy (EPO-TEK 353ND). This allows for the electrical isolation of the sample from the rest of the holder, thereby shielding the sample from any stray voltage which could reach the sample. The insert itself features a raised alignment guide, which is used when loading the sample. Care was taken to ensure that the epoxy was effectively concealed from the beam near the imaging axis which could potentially introduce astigmatism.

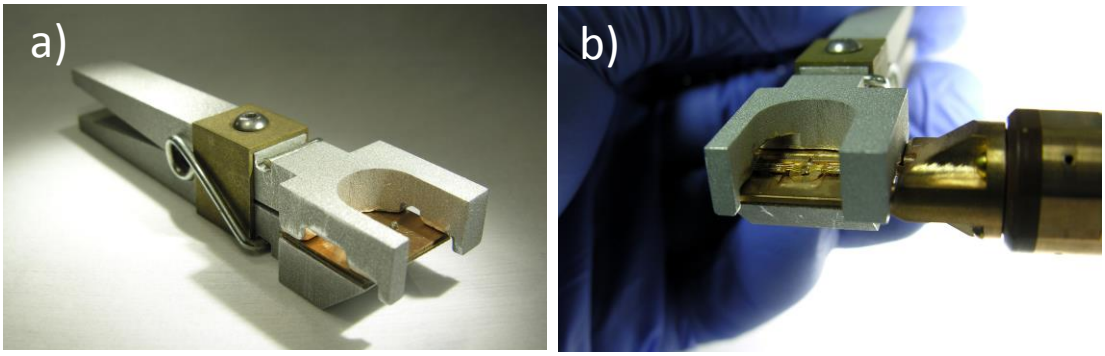

Figure A.2: Optical Image of Loading Tool. (**a**) Custom loading tool (**b**) Loading tool engaged on holder

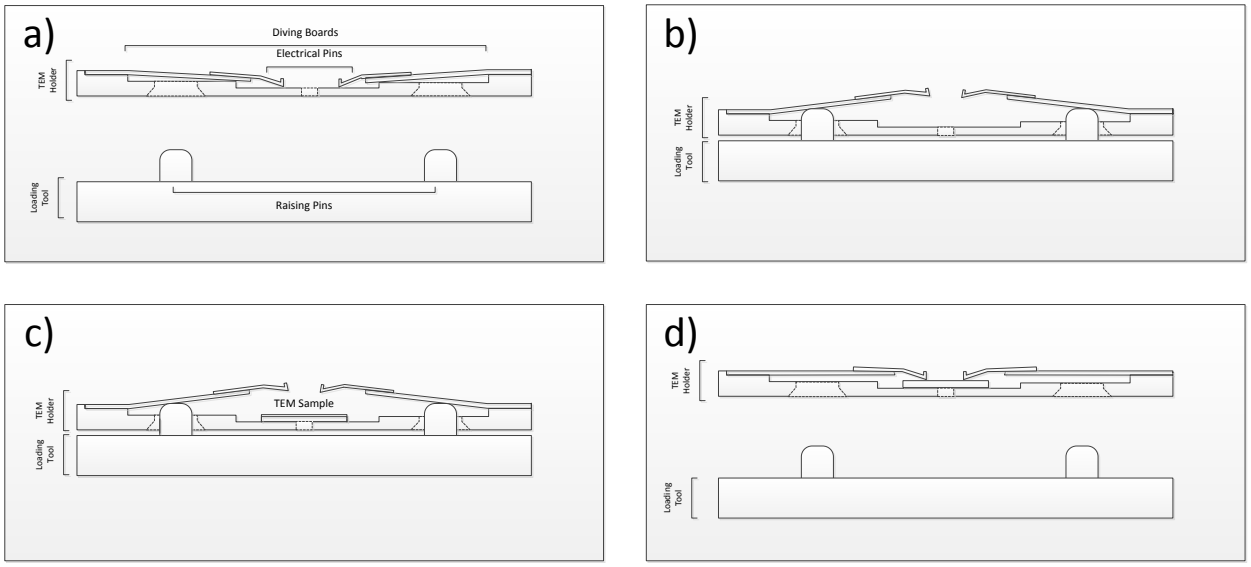

Figure A.3: Schematic of Loading Procedure. a) Electrical pins in resting position (with loading tool disengaged) b) Electrical pins raised (with the loading tool engaged) c) Electrical pins raised (with the loading tool engaged) and a conventional SiN TEM membrane in position d) Electrical pins resting on Au electrical pads (loading tool disengaged)

Two cantilevered springs (N1) made from .008mm thick Be-Cu sheets are then glued onto the nose piece using the insulating epoxy (EPO-TEK 353 ND). A dot of silver epoxy is used to establish electrical contact between the springs (N1) and nose piece to sustain touch sensor functionality. On top of each of the boards, four Au-plated Be-Cu wires (N2), of diameter .004mm, are attached using epoxy (See Figure A.1b). To ensure electrical isolation of the individual wires, a thin layer of insulating epoxy is spread on the surface prior to gluing the Be-Cu wires into place. The springs (N1) and electrical pins (N2) are positioned such that they provide both good electrical connection with the pre-patterned electrodes and exert a large enough force to hold the sample in place. The lack of set screws, wire bonding, or other clamping devices, simplifies the loading procedure and reduces the likelihood of

broken samples caused by loading. To load the sample, a custom tool is used which consists of two 1mm diameter pins (Figure A.2a). When engaged, the pins lift the springs (N1) and allow the sample to be positioned underneath the Be-Cu electrical pins (N2) (Figure A.3b). After the sample has been positioned (Figure A.3c), the tool is disengaged, which lowers the Be-Cu electrical pins (N2) onto the prefabricated electrodes on the TEM chip (Figure A.3d).

Within the holder rod, heavy polyimide (HML)-coated copper wires run from the end handle to an opening in the nose piece. Four wires extend from the center onto the closest diving board. The remaining five wires were run through an indentation in the nose piece. One wire exits to electrically connect the insert on which the sample sits. The wire enables control of the potential applied to the sample as well as detection of any unintended sample biasing. The remaining four wires continue to the outer diving board and connect to the last four Be-Cu electrical pins. To connect the HML coated wires to the Be-Cu electrical contacts, a small gold wire is glued using a small dot of conductive epoxy on both the end of the Be-Cu electrical wire and the HML coated wire, which had been previously stripped. This connection method serves dual purposes. First, should either of the wires (Be-Cu electrical wire and HML-coated Cu wire) need to be replaced, the other wire does not need to be changed. In addition, due to the electrical isolation between the diving board and Be-Cu electrical contacts, the likelihood of creating an electrical short between the two is reduced.

The end handle (Figure A.1c) is divided into a vacuum side and a non-vacuum side separated by flange **T2** in Figure A.1c. On the vacuum side, the first flange,

(labeled ***T1*** in Figure 1c), is glued directly to the holder rod itself. **T1** is at holder potential, connected electrically by a bead of conducting epoxy, and contains a face-seal O-ring that allows vacuum pumping of the holder. The middle flange (labeled ***T2*** in Figure A.1c) houses the 9-pin Detoronics multi-pin header (900F-94-HS4), labeled ***T3***, to which the coated Cu wires, were soldered. An insulating Delrin™ spacer (labeled ***T4***) is used to separate the holder ground from the experimental ground and is placed between the middle flange (flange ***T1***) and the end flange (flange ***T5***) . On the non-vacuum side of the middle flange (***T2***), 9 wires are soldered connecting the 9 pins of the Detoronics header to a Lemo receptacle. A tenth wire is used to electrically connect the holder itself, which is wedged between a piece of copper and the middle flange (**T2**).

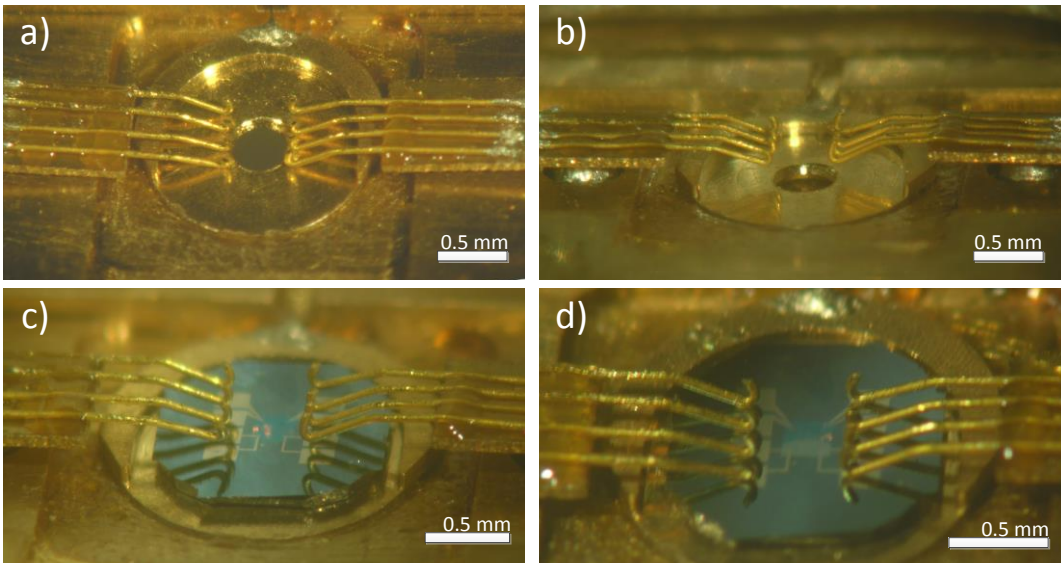

Figure A.4: Optical Image of Loading Procedure. (**a**) Electrical pins in resting position (with loading tool disengaged) (**b**) Electrical pins raised (with the loading tool engaged) (**c**) Electrical pins raised (with the loading tool engaged) and a conventional SiN TEM membrane in position (**d**) Electrical pins resting on Au electrical pads (loading tool disengaged)

A.5 Results and Discussion

As previously discussed, this holder provides the ability to study highly sensitive electrical devices, for various systems. In order to quantify the capabilities of the new design, two different measurements were conducted: leakage current measurements and voltage noise measurements. The ability to measure leakage current provides the opportunity to isolate one source of electrical device failure. The device being tested was fabricated on Silson Ltd. TEM membranes (50nm thick) with a window size of 50μm. The Cr/Au electrodes were pre-patterned using e-beam lithography followed by a thermal metal evaporation. All noise measurements were taken using a 2-6 mV peak to peak signal with a 300 MHz bandwidth oscilloscope. This yielded a measured voltage noise value of 230 nV ±115 $(Hz)^{-1/2}$. Therefore, when studying a sample with a measured resistance of 200Ω, a measured current noise of 230 nV ±115 $(Hz)^{-1/2}$ is expected.

We aim to study the performance using the measurement of electron beam induced current (EBIC). EBIC has been used to study the relationship between the electronic properties and structure of a material. [133] Electron-hole pairs at p-n junctions, or Schottky contacts, are generated by the electron beam. Our samples are 25 nm thick ZnO films deposited using RF sputtering. The substrate (SiN TEM membrane of 50μm thickness) is heated to 150 °C with a base pressure of around 2-4 E 10^{-7} Torr and a working pressure of 6 mTorr. The target-to-substrate distance is 66mm. Using a power of 100 W, ZnO films are deposited for 5 minutes at a deposition rate of roughly 5.3 nm/min. For previous samples created using these deposition conditions, samples of 4.5 10^{5} Ω·cm were produced. To pattern the

electrodes, Au is thermally evaporated onto the sample using a shadow mask to create a 25 μm gap. An approximate deposition rate of 1 Å/s was used to achieve an electrode thickness of 30nm.

EBIC experiments are conducted using the JEOL 2100FEG TEM in both TEM/STEM imaging modes. The interface between the Au electrodes and ZnO films can be seen in Figure A.5a taken in BF imaging conditions using Orius camera. Figure A.5b shows a HRTEM image of the ZnO film nanostructure. Our TEM holder offers the ability to achieve HRTEM imaging while simultaneously conducting EBIC experiments allowing for a more detailed development of the relationship between the electronic properties and the structure of the material. This was previously unachievable using the more common approach of EBIC studies using SEM.

Figure A.6 shows STEM images taken in BF imaging conditions (A.6a) and an EBIC generated image (Figure A.6b). The light fringes and dark fringes correspond to the passing of current from one electrode to the other. We found that by reversing the direction of current flow, the light fringe became dark and the dark fringe became light. We also found that by reversing the direction of the beam raster, the fringes behaved similarly. We are still working on understanding the specific causes for each of these changes.

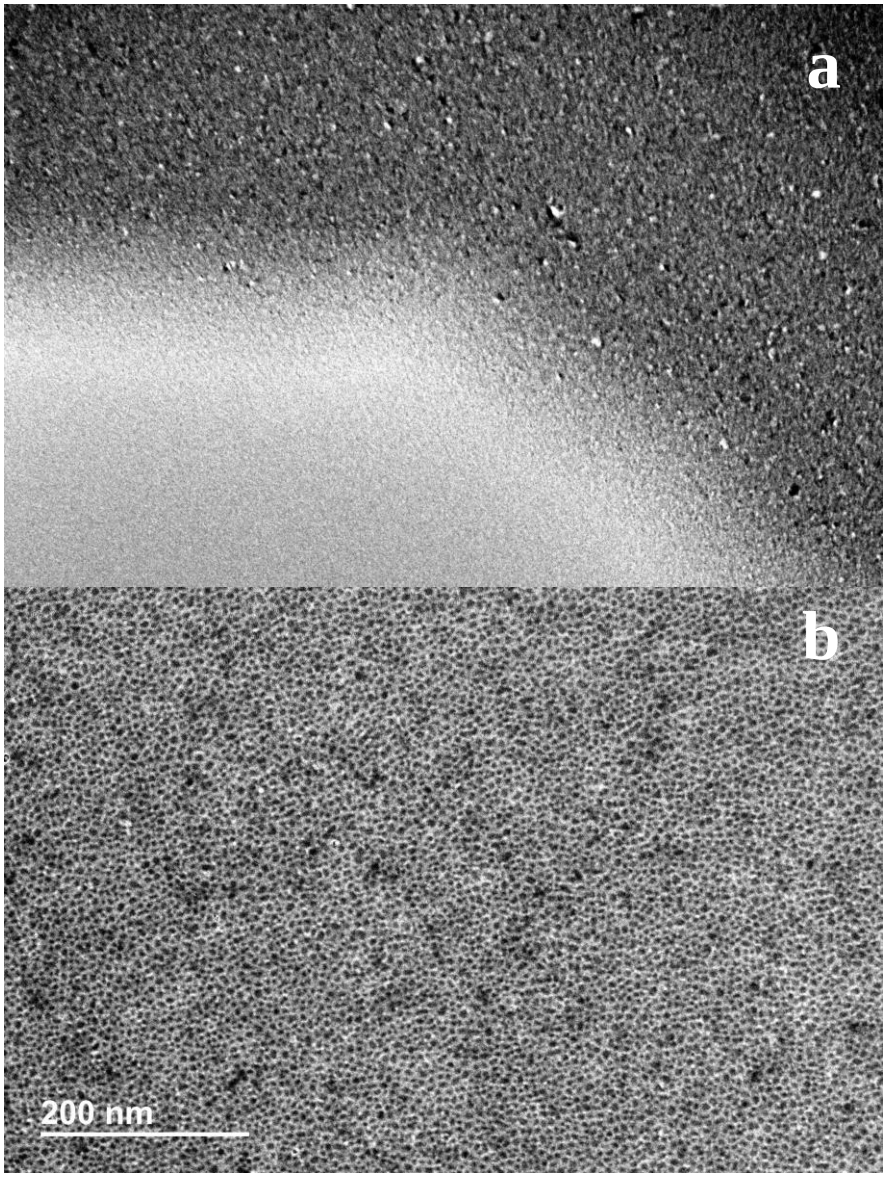

Figure A.5: TEM Images of ZnO/Au interface. (**a**) Interface of Au electrode (darker) and ZnO film (lighter) (**b**) HRTEM image showing ZnO microstructure

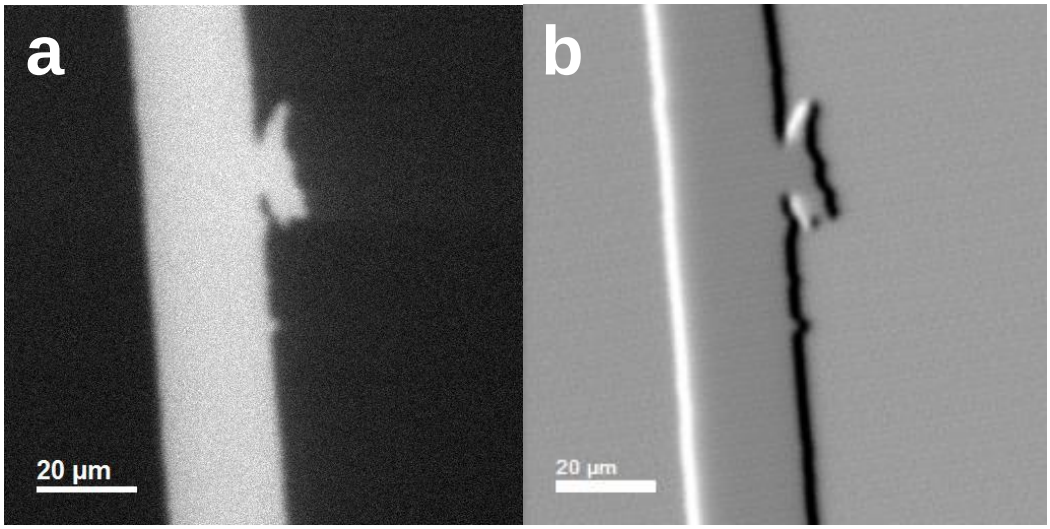

Figure A.6: EBIC experiments using custom TEM holder. (a)BF STEM image taken using JEOL camera (b) EBIC image taken using

A.6 Summary

A new *in-situ* electrical TEM holder has been designed to allow for the study of highly sensitive electrical devices. The electrical isolation of the chip allows for the study of highly sensitive electrical devices, while maintaining the functionality of the microscope's touch sensor. In addition, the sample isolation allows for the application of a gate voltage, as well as the precise measurement of both leakage current and voltage noise. The holder consists of eight Be-Cu electrical pins which serve as both electrical contacts and provide a clamping force to securely hold the sample in place. This removes the need for any sort of wire bonding, or permanent attachment between the holder and the TEM membrane. With the new holder, we carried out EBIC experiments allowing for a better correlation between the nanostructure of the material and the corresponding electrical properties.

Bibliography

[1] Lewis, N. S. (2007). Powering the Planet, 32 (October).

[2] Larcher, D. and Tarascon, J. M. (2015). "Towards greener and more sustainable batteries for electrical energy storage", *7*(January).

[3] M. Wakihara and O. Yamamoto, "Lithium-ion Batteries: Fundamentals and Performance", 1998.

[4] Goodenough, J. B., & Park, K. (2013). "The Li-Ion Rechargeable Battery : A Perspective", *Journal of the American Chemical Society*, *135*, 1167–1176.

[5] A. Yoshino, K. Sanechika, and B.T., Japanese patent 1989293," 1985.

[6] Y.X. Yin, S. Xin, Y.G. Guo, and L.J. Wan, "Lithium-sulfur batteries: Electrochemistry, materials and prospects", *Angewandte Chemie International Edition*, vol. 52, pp. 13186-13200, 2013.

[7] K. Zaghib, M. Donitgny, A. Guerfi, P. Charest, I. Rodrigues, A. Mauger, and C. Julien, "Safe and fast-charging li-ion battery with long shelf life for power applications", *Journal of Power Sources*, vol. 196, pp. 3949-3954, 2011.

[8] D. Herbert and J. Ulam, "Electric Dry Cells and Storage Batteries", 1962.

[9] Claus, C.F. (1882) British Patent 3608

[10] Apodaca, L. E. (2015). "Sulfur". *Mineral Commodity Summaries* (pp. 156–157).

[11] Komarnisky, L. A., Christopherson, R. J., & Basu, T. K. (2003). "Sulfur : Its Clinical and Toxicologic Aspects", 9007(02), 54–61.

[12] Kolosnitsyn, V. S., & Karaseva, E. V. (2008). "Lithium-sulfur batteries: Problems and solutions", *Russian Journal of Electrochemistry*, 44(5), 506–509.

[13] Li-S company Sion Power raises $50M. (2011). Retrieved from http://www.greencarcongress.com/2011/12/sion-20111227.html

[14] Wang, D.-W., Zeng, Q., Zhou, G., Yin, L., Li, F., Cheng, H.-M., Lu, G. Q. M. (2013). "Carbon-sulfur composites for Li-S batteries: status and prospects". *Journal of Materials Chemistry A*, 1(33), 9382–9394.

[15] Y. Mikhaylik and J. Akridge, "Polysulfide shuttle study in the Li/S battery system", *Journal of the Electrochemical Society*, vol. 151, pp. A1969-A1976, 2004.

[16] Xu, W., Wang, J., Ding, F., Chen, X., Nasybulin, E., Zhang, Y., & Zhang, J.-G. (2014). Lithium metal anodes for rechargeable batteries. *Energy & Environmental Science*, 7, 513.

[17] E. Peled. *J. Electrochem. Soc.*,126, 2047 (1979)

[18] Kozen, A. C., Lin, C., Pearse, A. J., Schroeder, M. A., Han, X., Hu, L., … Noked, M. (2015). Next-Generation Lithium Metal Anode Engineering via Atomic Layer Deposition, (6), 5884–5892.

[19] Chan, C. K., Peng, H., Liu, G., McIlwrath, K., Zhang, X. F., Huggins, R. a, & Cui, Y. (2008). High-performance lithium battery anodes using silicon nanowires. *Nature Nanotechnology*, *3*(1), 31–5. doi:10.1038/nnano.2007.411

[20] Weeks, M. C., Voss, E., Yoshizawa, S., Okada, S., Mathieson, R. T., Press, P., Manufacturing, C. (n.d.). "All-Solid Lithium Electrodes with Mixed-Conductor Matrix", (4), 1–5.

[21] Karki, K., Epstein, E., Cho, J., Jia, Z., Li, T., Picraux, S. T., Cumings, J. (2012). Lithium-Assisted Electrochemical Welding in Silicon Nanowire Battery Electrodes.

[22] Liu, N., Hu, L., Mcdowell, M. T., Jackson, A., & Cui, Y. (2011). Prelithiated Silicon Nanowires as an Anode for Lithium Ion Batteries, (8), 6487–6493.

[23] X.B. Cheng, J.Q. Huang, H.J. Peng, J.Q. Nie, X.Y. Liu, Q. Zhang, and F. Wei, "Polysulfide shuttle control: Towards a lithium-sulfur battery with superior capacity performance up to 1000 cycles by matching the sulfur/electrolyte loading", *Journal of Power sources*, vol. 253, pp. 263-268, 2014.

[24] S. Jeong, Y. Lim, Y. Choi, G. Cho, K. Kim, H. Ahn, and K. Cho, "Electrochemical properties of lithium sulfur cells using PEO polymer electrolytes prepared under three different mixing conditions", *Journal of Power Sources*, vol. 174, pp.745-750, 2007.

[25] Compton, R.G. and Banks, C. E. (2010). Understanding Voltammetry (1st ed.).

[26] Rauh, R. D., Abraham, K. M., Pearson, G. F., Surprenant, J. K., Brummer, S. B., & Corporation, E. I. C. (n.d.). A Lithium / Dissolved Sulfur Battery with an Organic Electrolyte.

[27] Suo, L., Hu, Y.-S., Li, H., Armand, M., & Chen, L. (2013). A new class of Solvent-in-Salt electrolyte for high-energy rechargeable metallic lithium batteries. *Nature Communications*, 4, 1481.

[28] Aurbach, D., Pollak, E., Elazari, R., Salitra, G., Kelley, C. S., & Affinito, J. (2009). On the Surface Chemical Aspects of Very High Energy Density, Rechargeable Li–Sulfur Batteries. *Journal of The Electrochemical Society*, 156(8), A694.

[29] Zhang, Z., Lai, Y., Zhang, Z., Zhang, K., & Li, J. (2014). Al2O3-coated porous separator for enhanced electrochemical performance of lithium sulfur batteries. *Electrochimica Acta*, 129, 55–61.

[30] Su, Y.-S., & Manthiram, A. (2012). Lithium–sulphur batteries with a microporous carbon paper as a bifunctional interlayer. *Nature Communications*, 3, 1166.

[31] S. Cheon, K. Ko, J. Cho, S. Kim, E. Chin, and H. Kim, "Rechargeable lithium sulfur battery – Structural change of sulfur cathode during discharge and charge", *Journal of the American Chemical Society*, vol. 150, pp. A796-A799, 2003.

[32] S. Evers and L. Nazar, \New approaches for high energy density lithium-sulfur battery cathode," *Journal of the American Chemical Society*, vol. 46, no. 5, pp. 1135{1143, 2012.

[33] B. Meyer, "Elemental sulfur," *Chemical reviews*, vol. 76, no. 3, pp. 367-388,1976.

[34] Press Release: The 1986 Nobel Prize in Physics". Nobelprize.org. Nobel Media AB 2014. Web. 20 Sep 2015

[35] Ruska, E. (1942). Beitrag zur Uebermikroskopischen Abbildung bei Hoeheren Drucken. Kolloid Zeitschrift, 100(2), 212–219.

[36] Knoll, M and Ruska, E 1932 Das Elektronenmikroskop (Electron Microscope) Z. Phys. 78 318–339

[37] Hirsch, PB, Howie, A, Nicholson, RB, Pashley, DW and Whelan, MJ 1977 Electron Microscopy of Thin Crystals 2nd Ed. Krieger Huntington NY.

[38] Tanaka, N. (2008). Present status and future prospects of spherical aberration corrected TEM/STEM for study of nanomaterials. Science and Technology of Advanced Materials, 9(1), 014111.

[39] D. B. Williams and C. B. Carter, Transmission Electron Microscopy. Springer, 2009.

[40] Neumann, K.(1934) Z. Phys. Chem., 171, pp. 416-420.

[41] Fouretier, G.(1944) Compt. Rend., 218, pp. 194-196.

[42] Taillade, M.(1944) Compt. Rend., 218, pp. 836-838.

[43] Bradley, R.S. (1951) Proc. Roy. Soc. A, 205, pp. 553-563.

[44] Briske, B. C., Hartshorne, N. H., & Stranks, D. R. (1964). The vapor pressures and latent heats of sublimation of alpha, beta, and gamma sulfur, (1200), 1200–1209.

[45] Barnaby D.A. et al., Microsc. & Microanal. 2014, 20(Supl.3), 446-447

[46] Geim, a K., & Novoselov, K. S. (2007). The rise of graphene. Nature Materials, 6(3), 183–191.

[47] Wang, M., Yan, C., & Ma, L. (2012). Graphene Nanocomposites.

[48] G. Zhou, S. Pei, L. Li, D.-W. Wang, S. Wang, K. Huang, L.-C. Yin, F. Li, and H.-M. Cheng, A graphenepure-sulfur sandwich structure for ultrafast,

long-life lithiumsulfur batteries," Advanced Materials, vol. 26, no. 4, pp. 625{631, 2014.

[49] Charlier, J. (2002). Defects in Carbon Nanotubes, 35(12), 1063–1069.

[50] Venema, L. C., Wildo, J. W. G., & Dekker, C. (1998). Electronic structure of atomically resolved carbon nanotubes ¨, 584(10), 1996–1999.

[51] Jiao, L., Zhang, L., Wang, X., Diankov, G., & Dai, H. (2009). Narrow graphene nanoribbons from carbon nanotubes. Nature, 458(7240), 877–80.

[52] Raimond, J. M., Brune, M., Computation, Q., Martini, F. De, & Monroe, C. (2004). Electric Field Effect in Atomically Thin Carbon Films, 306(October), 666–669.

[53] Novoselov, K. S., Fal'ko, V. I., Colombo, L., Gellert, P. R., Schwab, M. G., & Kim, K. (2012). A roadmap for graphene. Nature, 490(7419), 192–200.

[54] Yi, M., & Shen, Z. (2015). A review on mechanical exfoliation for scalable production of graphene. J. Mater. Chem. A, 3, 11700–11715.

[55] Jayasena, B., & Subbiah, S. (2011). A novel mechanical cleavage method for synthesizing few-layer graphenes. Nanoscale Research Letters, 6(1), 95.

[56] Charrier, A., Coati, a., Argunova, T., Thibaudau, F., Garreau, Y., Pinchaux, R., … Themlin, J.-M. (2002). Solid-state decomposition of silicon carbide for growing ultra-thin heteroepitaxial graphite films. Journal of Applied Physics, 92(5), 2479.

[57] Mayou, D., Li, T., Hass, J., Marchenkov, A. N., Conrad, E. H., First, P. N., & Heer, W. A. De. (2006). Electronic Confinement and coherence in patterned epitaxial graphene. Science, 312, 1191–1196.

[58] Ohta, T., Bostwick, A., Seyller, T., Horn, K., & Rotenberg, E. (2006). Controlling the electronic structure of bilayer graphene. Science (New York, N.Y.), 313(5789), 951–954.

[59] Bae, S., Kim, H., Lee, Y., Xu, X., Park, J.-S., Zheng, Y., … Iijima, S. (2010). Roll-to-roll production of 30-inch graphene films for transparent electrodes. Nature Nanotechnology, 5(8), 574–8.

[60] Li, X., Cai, W., Colombo, L., & Ruoff, R. S. (2009). Evolution of Graphene Growth on Ni and Cu by Carbon Isotope Labeling, 12(1).

[61] Naseem, H. (2014). CVD Graphene Growth Mechanism on Nickel Thin Films.

[62] Yu, Q., Lian, J., Siriponglert, S., Li, H., Chen, Y. P., & Pei, S.-S. (2008). Graphene segregated on Ni surfaces and transferred to insulators. Applied Physics Letters, 93(11), 113103.

[63] Reina, A., Jia, X., Ho, J., Nezich, D., Son, H., Bulovic, V., … Kong, J. (2009). Large Area , Few-Layer Graphene Films on Arbitrary Substrates by Chemical Vapor Deposition 2009, 1–6.

[64] Shelton, J. C. (1974). Equlibrium segregation of carbon to a nickel (111) surface: A surface phase transition, 43.

[65] Miyata, Y., Kamon, K., Ohashi, K., Kitaura, R., Yoshimura, M., & Shinohara, H. (2010). A simple alcohol-chemical vapor deposition synthesis of single-layer graphenes using flash cooling. Applied Physics Letters, 96(26), 2013–2016.

[66] Zhang, Y., Zhang, L., & Zhou, C. (2013). Review of chemical vapor deposition of graphene and related applications. Accounts of Chemical Research, 46(10), 2329–2339.

[67] Yazyev, O. V., & Louie, S. G. (2010). Topological defects in graphene: Dislocations and grain boundaries. Physical Review B - Condensed Matter and Materials Physics, 81(19), 1–7.

[68] Huang, P. Y., Ruiz-Vargas, C. S., van der Zande, A. M., Whitney, W. S., Levendorf, M. P., Kevek, J. W., … Muller, D. A. (2011). Grains and grain boundaries in single-layer graphene atomic patchwork quilts. Nature, 469(7330), 389–392.

[69] Yu, Q., Jauregui, L. a, Wu, W., Colby, R., Tian, J., Su, Z., … Chen, Y. P. (2011). Control and characterization of individual grains and grain boundaries in graphene grown by chemical vapour deposition. Nature Materials, 10(6), 443–9.

[70] Kang, J., Shin, D., Bae, S., & Hong, B. H. (2012). Graphene transfer: key for applications. Nanoscale, 4(18), 5527.

[71] Lee, J. N., Park, C., & Whitesides, G. M. (2003). Solvent Compatibility of Poly (dimethylsiloxane) -Based Microfluidic Devices, 75(23), 6544–6554.

[72] Kim, K. S., Zhao, Y., Jang, H., Lee, S. Y., Kim, J. M., Kim, K. S., … Hong, B. H. (2009). Large-scale pattern growth of graphene films for stretchable transparent electrodes. Nature, 457(7230), 706–10.

[73] Li, X., Zhu, Y., Cai, W., Borysiak, M., Han, B., Chen, D., … Ruoff, R. S. (2009). Transfer of Large-Area Graphene Films for High-Performance Transparent Conductive Electrodes.

[74] Caldwell, J. D., Anderson, T. J., Culbertson, J. C., Jernigan, G. G., Hobart, K. D., Kub, F. J., Gaskill, D. K. (n.d.). Technique for the Dry Transfer of Epitaxial Graphene onto Arbitrary Substrates, 4(2), 1108–1114.

[75] Berber, S., Kwon, Y., & Tománek, D. (2000). Unusually High Thermal Conductivity of Carbon Nanotubes, 84(20), 4613–4616.

[76] Getty, S. A., Cobas, E., & Fuhrer, M. S. (2004). Extraordinary Mobility in Semiconducting Carbon Nanotubes, 2–6.

[77] Robertson, D. H., & Brenner, D. W. (1992). Energetics of nanoscale graphitic tubules, 45(21), 592–595.

[78] Baughman, R. H., Zakhidov, A. A., & Heer, W. A. De. (2002). Carbon Nanotubes — the Route Toward Applications, 297(August), 787–793.

[79] Ajayan, P. M., & Lijima, S. (1993). Capillarity-induced filling of carbon nanotubes. Nature, 361(6410), 333–334. http://doi.org/10.1038/361333a0

[80] T. Fujimori, A. Morelos-Gomez, Z. Zhu, H. Muramatsu, R. Futamura, K. Urita,M. Terrones, T. Hayashi, M. Endo, S. Y. Hong, Y. C. Choi, D. Tomanek, and K. Kaneko, Conducting linear chains of sulphur inside carbon nanotubes," Nature Communications, vol. 4, no. 2162, 2013.

[81] R. Steudel and B. Eckert, \Solid sulfur allotropes," Top Current Chemistry,vol. 230, pp. 1-79,2003.

[82] Y. Akahama, M. Kobayashi, and H. Kawamurat, \Pressure-induced structural phase transition in sulfur at 83 gpa," Physical Review B, vol. 230, pp. 1{79, 1993.

[83] Dresselhaus, B. M. S., Dresselhaus, G., & Charlier, J. C. (2004). Electronic , thermal and mechanical properties of carbon nanotubes, 2065–2098.

[84] Ajayan, PM and Colliex, C. and Bernier, P. and Lambert, J. M. (1994). Shape transformations in single-layer carbon nanotubes, 4(December 1993), 501–504.

[85] Ajayan, P. M., Ravikumar, V., & Charlier, J. (1998). Surface Reconstructions and Dimensional Changes in Single-Walled Carbon Nanotubes, 1437–1440.

[86] Zaiser, M., & Banhart, F. (1997). Radiation-Induced Transformation of Graphite to Diamond, 1–4.

[87] Species, S and Wales, D. J. (1986). Theoretical studies of isosahedral C60 and some related species, 128(5), 501–503.

[88] Ajayan, P., Ebbesen, T., & Ichihashi, T. (1993). Opening carbon nanotubes with oxygen and implications for filling. Nature, 362, 522–525.

[89] Bethune, D.S. and Klang, C.H. and de Vries, M.S. and Gorman, G. and Savoy, R. and Vazquez, J. and Beyers, R. (1993). Cobalt-catalysed growth of carbon nanotubes with single-atomic-layer walls. Nature, 363, 605–607.

[90] Osswald, S., Flahaut, E., Ye, H., & Gogotsi, Y. (2005). Elimination of D-band in Raman spectra of double-wall carbon nanotubes by oxidation. Chemical Physics Letters, 402(4-6), 422–427.

[91] Ajayan, P., Ebbesen, T., & Ichihashi, T. (1993). Opening carbon nanotubes with oxygen and implications for filling. Nature, 362, 522–525.

[92] Braun, D. C., Francisco, S., Braun, D. C., Braun, D. C., & Administra-, A. (2000). Extreme Oxygen Sensitivity of Electronic Properties of Carbon, 287(March), 1801–1805.

[93] Soo, Y., Chul, Y., Soo, K., Chung, D., Jae, D., Hyeok, K., … Hee, Y. (2001). High yield purification of multiwalled carbon nanotubes by selective oxidation during thermal annealing, 39, 655–661.

[94] Soo, Y., Chul, Y., Soo, K., Chung, D., Jae, D., Hyeok, K., … Hee, Y. (2001). High yield purification of multiwalled carbon nanotubes by selective oxidation during thermal annealing, 39, 655–661.

[95] Lee, Y., Kim, S., & Tománek, D. (1997). Catalytic Growth of Single-Wall Carbon Nanotubes: An Ab Initio Study. Physical Review Letters, 78(12), 2393–2396.

[96] Zhu, X. Y., Lee, S. M., Lee, Y. H., & Frauenheim, T. (2000). Adsorption and Desorption of an O 2 Molecule on Carbon Nanotubes, 1, 2757–2760.

[97] Tabin, C. J., Speed, M. P., Smith, B. W., Monthioux, M., & Luzzi, D. E. (1998). Encapsulated C60 in carbon nanotubes, 396(November), 323–324.

[98] Datsyuk, V., Kalyva, M., Papagelis, K., Parthenios, J., Tasis, D., Siokou, a., … Galiotis, C. (2008). Chemical oxidation of multiwalled carbon nanotubes. Carbon, 46(6), 833–840.

[99] Kosynkin, D. V, Higginbotham, A. L., Sinitskii, A., Lomeda, J. R., Dimiev, A., Price, B. K., & Tour, J. M. (2009). Longitudinal unzipping of carbon nanotubes to form graphene nanoribbons. Nature, 458(7240), 872–6.

[100] H. Wang, Y. Yang, Y. Liang, J. T. Robinson, Y. Li, A. Jackson, Y. Cui, and H. Dae, Graphene-wrapped sulfur particles as a rechargeable lithiumsulfur battery cathode material with high capacity and cycling stabilityt," Nanoletters, vol. 11, pp. 2644{2647, 2011.

[101] S. Xin, L. Gu, N.-H. Zhao, Y.-X. Yin, L.-J. Zhou, Y.-G. Guo, and L.-J. Wan, Smaller sulfur molecules promise better lithium-sulfur batteries," Journal of the American Chemical Society, vol. 134, pp. 18510{18513, 2012.

[102] Dresselhaus, M. S., Dresselhaus, G., Saito, R., & Jorio, a. (2005). Raman spectroscopy of carbon nanotubes. Physics Reports, 409(2), 47–99.

[103] Pimenta, M. A., & Marucci, A. (1998). Raman modes of metallic carbon nanotubes, 58(24), 16–19.

[104] Brown, S. D. M., Jorio, a., Corio, P., Dresselhaus, M. S., Dresselhaus, G., Saito, R., & Kneipp, K. (2001). Origin of the Breit-Wigner-Fano lineshape of the tangential G -band feature of metallic carbon nanotubes. Physical Review B, 63(15), 155414.

[105] Nanotubes, M. C., Liu, Y., Zheng, H., Liu, X. H., Huang, S., Zhu, T., … Kushima, A. (2011). Lithiation-Induced Embrittlement of carbon nanotubes, (9), 7245–7253.

[106] Bagri, A., Mattevi, C., Acik, M., Chabal, Y. J., Chhowalla, M., & Shenoy, V. B. (2010). Structural evolution during the reduction of chemically derived graphene oxide. Nature Chemistry, 2(7), 581–7.

[107] Xu, R., Belharouak, I., Zhang, X., Chamoun, R., Yu, C., Ren, Y., … Amine, K. (2014). Insight into Sulfur Reactions in Li − S Batteries.

[108] Lin, Z., & Liang, C. (2015). Lithium–sulfur batteries: from liquid to solid cells. J. Mater. Chem. A, 3(3), 936–958.

[109] Verma, P., Maire, P., & Novák, P. (2010). A review of the features and analyses of the solid electrolyte interphase in Li-ion batteries. Electrochimica Acta, 55(22), 6332–6341.

[110] Goodenough, J., Abruña, H., & Buchanan, M. (2007). Basic research needs for electrical energy storage. US Department of Energy …, 186. Retrieved from http://www.sc.doe.gov/bes/reports/files/EES_rpt.pdf

[111] Sebastian, L., & Gopalakrishnan, J. (2003). Lithium ion mobility in metal oxides: a materials chemistry perspective Based on a lecture delivered at the international symposium "Materials for Energy: Batteries and Fuel Cells", November 2002, Madrid, Spain. Journal of Materials Chemistry, 13(3), 433–441.

[112] Zhu, G., Jiang, Y., Huang, W., Zhang, H., Lin, F., & Jin, C. (2013). Atomic resolution liquid-cell transmission electron microscopy investigations of the dynamics of nanoparticles in ultrathin liquids. Chemical Communications (Cambridge, England), 49(93), 10944–6.

[113] Abellan, P., Mehdi, B. L., Parent, L. R., Gu, M., Park, C., Xu, W., Browning, N. D. (2014). Probing the degradation mechanisms in electrolyte solutions for li-ion batteries by in situ transmission electron microscopy. Nano Letters, 14(3), 1293–1299.

[114] Leenheer, A. J., Sullivan, J. P., Shaw, M. J., & Harris, C. T. (2014). A Sealed Liquid Cell for In Situ Transmission Electron Microscopy of Controlled Electrochemical Processes, 1–8.

[115] Alpen, U. V., Rabenau, a., & Talat, G. H. (1977). Ionic conductivity in Li3N single crystals. Applied Physics Letters, 30(12), 621. doi:10.1063/1.89283

[116] Kamaya, N., Homma, K., Yamakawa, Y., Hirayama, M., Kanno, R., Yonemura, M., … Mitsui, A. (2011). A lithium superionic conductor. Nature Materials, 10(9), 682–6. doi:10.1038/nmat3066

[117] Zhao, Y., Zhang, Y., Gosselink, D., Doan, T. N. L., Sadhu, M., Cheang, H.-J., & Chen, P. (2012). Polymer electrolytes for lithium/sulfur batteries. Membranes, 2(3), 553–64. doi:10.3390/membranes2030553

[118] Song, J. Y., Wang, Y. Y., & Wan, C. C. (1999). Review of gel-type polymer electrolytes for lithium-ion batteries.

[119] Lee, Y.-J., Jeong, S.-K., & Jo, N.-J. (2009). PVDF-Based Nanocomposite Solid Polymer Electrolytes; the Effect of Affinity Between PVDF and Filler on Ionic Conductivity. Composite Interfaces, 16(4-6), 347–358.

[120] Croce, F., Appetecchi, G. B., Persi, L., & Scrosati, B. (1998). Nanocomposite polymer electrolytes for lithium batteries, 394(July), 456–458.

[121] Hayashi, A., Ohtomo, T., Mizuno, F., Tadanaga, K., & Tatsumisago, M. (2003). All-solid-state Li/S batteries with highly conductive glass–ceramic electrolytes. Electrochemistry Communications, 5(8), 701–705.

[122] Pradel, A., & Ribes, M. (1986). Electrical properties of lithium conductive silicon sulfide glasses prepared by twin roller, 19, 351–355.

[123] Pradel, A., & Ribes, M. (1986). Electrical properties of lithium conductive silicon sulfide glasses prepared by twin roller, 19, 351–355.

[124] Zhengming, Z. H. A. N. G., & Kennedy, J. H. (1990). Synthesis and characterization of the B2S3-Li2S, he P2S5-Li2S and the B2S3-P2S5-Li2S glass systems, 38, 217–224.

[125] Liu, Y., Zheng, H., Liu, X. H., Huang, S., Zhu, T., … Kushima, A. (2011). Lithiation-Induced Embrittlement of carbon nanotubes, (9), 7245–7253.

[126] Tatsumisago, M., & Hayashi, A. (2012). Superionic glasses and glass–ceramics in the Li2S–P2S5 system for all-solid-state lithium secondary batteries. Solid State Ionics, 225, 342–345.

[127] Yamada, T., Ito, S., Omoda, R., Watanabe, T., Aihara, Y., Agostini, M., … Scrosati, B. (2015). All Solid-State Lithium-Sulfur Battery Using a Glass-Type P2S5-Li2S Electrolyte: Benefits on Anode Kinetics. Journal of the Electrochemical Society, 162(4), A646–A651.

[128] Liu, Y., Zheng, H., Liu, X. H., Huang, S., Zhu, T., Kushima, A. (2011). Lithiation-Induced Embrittlement of carbon nanotubes, (9), 7245–7253.

[129] Maurin, G., Bousquet, C., & Henn, F. (1999). Electrochemical intercalation of lithium into multiwall carbon nanotubes, (October), 14–18.

[130] J. C. Lewis, B. Redfern, and F. C. Cowlard, Solid-State Electronics 6 (1963) 251

[131] Clark, A., & Plessey, T. (1967). Vitreous carbon - a new form of carbon, 2, 507–512.

[132] Simmonds, A. G., Griebel, J. J., Park, J., Kim, K. R., Chung, W. J., Oleshko, V. P., Char, K. (2014). Inverse Vulcanization of Elemental Sulfur to Prepare Polymeric Electrode Materials for Li − S Batteries.

[133] Han, M.-G., Zhu, Y., Sasaki, K., Kato, T., Fisher, C. a. J., & Hirayama, T. (2010). Direct measurement of electron beam induced currents in p-type silicon. Solid-State Electronics, 54(8), 777–780.

[134] Larson, J. M., Bharath, S. C., Cullen, W. G., & Reutt-Robey, J. E. (2015). Scanning MWCNT-Nanopipette and Probe Microscopy: Li Patterning and Transport Studies. Small, n/a–n/a.